



**HAL**  
open science

## **Origin of the Oligocene manganese deposit at Obrochishte (Bulgaria): Insights from C, O, Fe, Sr, Nd, and Pb isotopes**

Vesselin M. Dekov, J. Barry Maynard, George D. Kamenov, Olivier Rouxel, Stefan Lalonde, Sava Juranov

### ► **To cite this version:**

Vesselin M. Dekov, J. Barry Maynard, George D. Kamenov, Olivier Rouxel, Stefan Lalonde, et al.. Origin of the Oligocene manganese deposit at Obrochishte (Bulgaria): Insights from C, O, Fe, Sr, Nd, and Pb isotopes. *Ore Geology Reviews*, 2020, 122, <10.1016/j.oregeorev.2020.103550>. <hal-02933388>

**HAL Id: hal-02933388**

**<https://hal.science/hal-02933388v1>**

Submitted on 24 May 2024

**HAL** is a multi-disciplinary open access archive for the deposit and dissemination of scientific research documents, whether they are published or not. The documents may come from teaching and research institutions in France or abroad, or from public or private research centers.

L'archive ouverte pluridisciplinaire **HAL**, est destinée au dépôt et à la diffusion de documents scientifiques de niveau recherche, publiés ou non, émanant des établissements d'enseignement et de recherche français ou étrangers, des laboratoires publics ou privés.



HAL Authorization

## Origin of the Oligocene manganese deposit at Obrochishte (Bulgaria): Insights from C, O, Fe, Sr, Nd, and Pb isotopes

Dekov Vesselin M. <sup>1,2,\*</sup>, Barry Maynard J. <sup>3</sup>, Kamenov George D. <sup>4</sup>, Rouxel Olivier <sup>2,5</sup>, Lalonde Stefan <sup>6</sup>, Juranov Sava <sup>7</sup>

<sup>1</sup> Department of Marine Resources and Energy, Tokyo University of Marine Science and Technology, 4-5-7 Konan, Minato-ku, Tokyo, Japan

<sup>2</sup> Unité de Géosciences Marines, IFREMER, Z.I. Pointe du diable, BP 70 - 29280, Plouzané, France

<sup>3</sup> Department of Geology, University of Cincinnati, P.O. Box 210013, Cincinnati, OH 45221-0013, USA

<sup>4</sup> Department of Geological Sciences, University of Florida, 241 Williamson Hall, Gainesville, FL 32611, USA

<sup>5</sup> Department of Oceanography, School of Ocean and Earth Science and Technology, University of Hawaii at Manoa, 1000 Pope Road, MSB 510, Honolulu, HI 96822, USA

<sup>6</sup> CNRS-UMR6538 Laboratoire Géosciences Océan, European Institute for Marine Studies, Technopôle Brest-Iroise, Place Nicolas Copernic, 29280 Plouzané, France

<sup>7</sup> Department of Geology and Paleontology, University of Sofia, 15 Tzar Osvoboditel Blvd., 1000 Sofia, Bulgaria

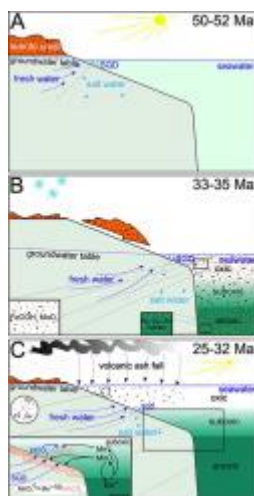
\* Corresponding author : Vesselin M. Dekov, email address : [vdekov0@kaiyodai.ac.jp](mailto:vdekov0@kaiyodai.ac.jp)

### Abstract :

The large manganese (Mn) deposit at Obrochishte (NE Bulgaria) is part of a cluster of similar Early Oligocene deposits located around present-day Black Sea. They collectively constitute the Earth's second largest endowment of Mn, after the Kalahari Manganese Field in Africa. We have employed a battery of isotopic techniques (C, O, Fe, Sr, Nd, Pb) to help understand the genesis of this deposit. Carbon isotope data indicates that some sections of the Mn-ore layer have diagenetic MnCO<sub>3</sub> mineralization, formed by reaction of Mn oxides with organic carbon (Corg), whereas other sections have MnCO<sub>3</sub> precipitated directly from the seawater column. Oxygen isotopes show that the high-grade Mn mineralization had seawater as the fluid source, whereas some lower-grade sections had a mix of ground water and seawater as fluid sources. Sr and Nd isotope values of ore leachates also indicate that the Mn deposition occurred in normal Early Oligocene seawater. Nd and Pb isotope values suggest that the clastic host sediments were sourced from continental bedrock rather than younger arc volcanic rocks to the west. Iron isotope composition of the Mn ore implies deposition in a redox-stratified basin, similar to the modern Black Sea, with much of the Fe sequestered in deep, anoxic-euxinic water as sulfides. Similar to the modern Black Sea, most of the detrital Fe was transferred from shallow oxic sediments into deep, anoxic-euxinic water by an "iron shuttle" and remobilized Mn sequestered in the upper suboxic water layer. However, during the Oligocene, the "iron shuttle" operated intermittently due to the chemocline falling mostly below the shelf break, thereby limiting the efficiency of the shuttle mechanism. We propose a model for the Lower Oligocene strata in which intense weathering during the Eocene weathering phase produced a thick lateritic crust on the southern European continent. The drastic sea-level drop at the end of the Eocene initiated downcutting of streams through this weathered material, transferring Fe- and Mn-oxides to the redox-stratified Western Black Sea. Here, these oxides were partly or entirely dissolved in the suboxic

(Mn-oxides partly, Fe-oxyhydroxides entirely dissolved) and anoxic-euxinic (Mn-oxides entirely dissolved, dissolved Fe<sup>2+</sup> re-precipitated) water layers. Eventually, Fe was re-precipitated as sulfide in the deep anoxic-euxinic water, while Mn accumulated in the suboxic water layer. Transgression in the Early Oligocene brought this Mn-rich water onto the shallow shelf where it precipitated as Mn-oxide, then converted to Mn-carbonates during early diagenesis. Some Mn was also contributed by submarine groundwater discharge. Further transgression brought lower-oxygen water onto the shelf and Mn-carbonate precipitated directly from the water column. The findings from this work provide insights about the unique Oligocene geochemical event in the region that led to the formation of the 2nd largest cluster of Mn deposits in the world.

### Graphical abstract



### Highlights

► Mn-carbonate ore at the Obrochishte has dual origin: diagenetic and authigenic. ► Mn deposition was a result of the climatic events at the Late Eocene-Early Oligocene. ► Mn ore was deposited in a redox-stratified basin, similar to the modern Black Sea.

**Keywords** : Mn metallogenesis, C-O-Fe-Sr-Nd-Pb isotopes, Early Oligocene, submarine groundwater discharge, water column anoxia, proto-Black Sea geochemistry

61

62 **1. Introduction**

63

64 The Oligocene Mn deposit in north-east Bulgaria (known as Obrochishte, or in older  
65 literature as Varna deposit) is one of a group of large deposits of Oligocene age that encircle the  
66 Black Sea. These include the deposits from the Chiatura (Georgia), Laba (Russia), Nikopol and

67 Bol'shoy Tokmak deposits (Ukraine) and Binkiliç deposit (NE Turkey) (Varentsov, 2002;  
68 Kuleshov, 2003, 2017). Collective reserves of all of these deposits are on the order of  $600 \times 10^6$   
69 metric tons of Mn making this region the world's second largest repository of Mn, after the  
70 supergiant Kalahari Manganese Field of South Africa (Maynard, 2010; Beukes et al., 2016).  
71 Recent information on reserves at Obrochishte itself is scarce. One source (GIS/GEODE 2016)  
72 gives a figure of  $16 \times 10^6$  metric tons at 28% Mn. Data in the USGS minerals yearbooks shows  
73 cumulative production in 1963-2016 was  $2.2 \times 10^6$  metric tons per year of ore with 28.6% Mn.

74 Mn-ore bed in outcrops (Vassilev et al., 1958; Stoyanov, 1961, 1963; Vangelova et al.,  
75 2005), in drill cores (Aleksiev, 1959; Stoyanov, 1961, 1963; Gnoevaya et al., 1982), and in mine  
76 sections (Obrochishte mine) in NE Bulgaria has been the subject of a number of studies aiming at  
77 shedding light on its geology (Mandev, 1954; Vassilev et al., 1958; Stoyanov, 1961, 1963;  
78 Bogdanova, 1968), sedimentology (Aleksiev, 1960b; Stoyanov, 1963; Aleksiev and Nacheva,  
79 1966; Vangelova et al., 2005), mineralogy (Vassilev et al., 1958; Aleksiev and Nacheva, 1966;  
80 Vassilev, 1967; Bogdanova, 1968; Puliev and Alexiev, 1972; Milakovska et al., 2006; Atanasova  
81 et al., 2009), and major element geochemistry (Vassilev et al., 1958; Aleksiev and Nacheva, 1966;  
82 Vassilev, 1967; Puliev and Alexiev, 1972; Vangelova et al., 2005; Milakovska et al., 2006).

83 The comprehensive mineralogy work of Vassilev et al. (1958) found that the only primary  
84 Mn-minerals (and at the same time the major ore minerals) in the deposit were Ca-rhodochrosite  
85 and Mn-calcite. Less abundant Mn-oxyhydroxides were secondary minerals formed as weathering  
86 products on the primary Mn-carbonates (Vassilev et al., 1958). Thus, two Mn-ore types can be  
87 distinguished on the basis of major Mn minerals determined in the ore bed: carbonate (primary)  
88 and oxyhydroxide (secondary). Later studies (Aleksiev, 1960a; Aleksiev and Nacheva, 1966;  
89 Puliev and Alexiev, 1972) claimed that a part of some of the Mn-ore layers was composed of Mn-

90 silicates (e.g., neotocite), but they did not provide any solid proofs for presence of these minerals  
91 in the deposit. (Neotocite was determined on the basis of: three unclear peaks at the Debye-  
92 Scherrer X-ray diffraction pattern, three peaks at the differential thermal curve, major element  
93 concentrations measured through unknown method, optical microscopy, and hand specimen  
94 description.) The results of these studies were accepted without any criticism by later workers and  
95 this led to creation and wide circulation of incorrect classifications of the major ore types in this  
96 deposit: e.g., Mn-carbonate, Mn-carbonate/Mn-silicate, Mn-silicate, and Mn-oxyhydroxide/Mn-  
97 carbonate (Gnoevaya et al., 1982). In addition to the imprecise mineralogy determinations there  
98 has been no attempt to investigate in detail the geochemistry (including radiogenic and stable  
99 isotopes) of the Mn-ore bed in order to shed light on the fluid and metal sources. Therefore, the  
100 suggested genetic models for this deposit (Vassilev et al., 1958; Aleksiev and Nacheva, 1966;  
101 Vangelova et al., 2005) based on geological, mineralogical, and geochemical (major elements)  
102 considerations were mostly speculative.

103         The size of the deposit at Obrochishte (largest in Europe), and its similarity to the group of  
104 deposits of the same age around the Black Sea, makes it an ideal site to investigate the genesis of  
105 the sedimentary Mn ores. Detailed trace element and isotope investigation can provide information  
106 about why so much Mn was deposited over such a short period of time around Black Sea? The  
107 answer must lie in the geochemistry of the basin seawater at this time and place. In this work, we  
108 provide a comprehensive set of geochemical and isotopic (C, O, Fe, Sr, Nd, and Pb) data for  
109 samples from the Obrochishte deposit and its host rocks, in order to decipher the processes that  
110 lead to the formation of the largest European Mn mineralization.

111

112

## 113 2. Geological setting

114

115 Mn mineralization in NE Bulgaria and the adjacent Black Sea shelf is located within the  
116 Ruslar Formation (Tenchov, 1993), which is a part of the Oligocene Series (Lower and Upper)  
117 (Fig. 1A, B). Thickness of this Formation varies from a few tens of meters up to ~900 m (based  
118 on drill core data). At the majority of the studied sites, it overlies both the Avren and Aladan  
119 Formations (Tenchov, 1993) (Fig. 1B, lithostratigraphic core logs). The lower boundary of the  
120 Ruslar Formation marks a hiatus stratigraphically interpreted to have varying time span: from  
121 Late Cretaceous to Late Eocene. When the hiatus in sedimentation had been long (Fig. 1B,  
122 uppermost lithostratigraphic core log) the lower boundary of the Formation is sharp. In the  
123 southern part of the region the hiatus had likely been short (Fig. 1B, middle and lowermost  
124 lithostratigraphic core logs) and the lower boundary of the Formation is gradational and unclear.  
125 The Ruslar Formation is overlain by different stratigraphic units (with hiatus) of the Neogene  
126 System (Fig. 1B, lithostratigraphic core logs).

127 Biostratigraphically, the Mn horizon was deposited in the Early Oligocene during the  
128 Pshekian stage at the transition from Nannoplankton (NP) zone 21 to zone 22 (Sachsenhofer et  
129 al., 2009, their Figure 2). At the Eocene-Oligocene boundary, which occurs in the NP zone 21,  
130 there was a brief, but extensive regression that created an erosional unconformity. Following this  
131 regressive episode, sea-level rapidly recovered and by the beginning of NP22, when Mn  
132 deposition began, had returned close to pre-regression level (Mayer et al., 2017, their Figure 2).  
133 Throughout the succeeding NP22 zone, sea-level fell, but slowly. Surface water salinity also fell  
134 until brackish conditions developed at the beginning of the NP23 zone. This has been referred to  
135 as the “Solenovian Event” (e.g., Sachsenhofer et al., 2017).

136 The Ruslar Formation is composed of clays, sandstones, siltstones, and marls (Aleksiev and  
137 Nacheva, 1966). The dominance of clays makes it easily recognizable among the other  
138 Formations. The clays are finely laminated, gray to brown, with varying silt component, and non-  
139 calcareous. Siltstones are gray-green and often grade into silty clays and silty sandstones. Marls  
140 are light-gray to green and show unclear laminations. They form a compact body at the middle of  
141 the Ruslar Formation. Thus, the Formation is clearly divided into three units north of Varna:  
142 under-marl unit (R1), marl unit (R2), and over-marl unit (R3) (Fig. 1B). South of Varna, the marls  
143 are presented as single isolated layers. The Ruslar Formation contains also spongolites,  
144 diatomites, and bentonites, which form scattered, single, isolated layers.

145 Manganese mineralization forms 1 to 4 beds within the lower part of the Ruslar Formation  
146 (Gnoevaya et al., 1982). The thickest Mn-ore beds are within the siltstones and sandstones of the  
147 under-marl unit (R1) north-east of Varna and within the clays of the lower part of the Formation  
148 south of the Kamchia River. The ore bed thickness varies from 2 to 24 m, with 11.3 m within the  
149 Obrochishte mine area.

150

151

### 152 **3. Samples and methods of investigation**

153

#### 154 *3.1. Samples*

155

156 We investigated 27 samples from the Mn-ore bed and 5 samples from the host-rock (both  
157 below and above the Mn-ore bed) all located at the basal part of the Ruslar Formation recovered  
158 at 11 sampling sites (Fig. 1): 12 samples from 5 drill cores, 12 samples from 5 outcrops, and 8

159 samples from the Obrochishte mine (Table 1). The eight mine samples were collected across the  
160 Mn-ore bed crossed and mined at shaft #1 (~320 m below the surface) of the Obrochishte mine  
161 located near the Tzarkva village (Dobrich district, northeast Bulgaria). Drill core and outcrop  
162 samples were collected by us. Samples from the Obrochishte mine were provided by the mine  
163 geologist Mr. Plamen Neychev following our requirements based on the mine report description  
164 of the Mn-ore bed. Pisoliths from 6 mine samples and the matrix among them from one sample  
165 were selected by hand picking for further analyses.

166

### 167 *3.2. Methods of investigation*

168

169 Initial characterization of the samples was with a binocular microscope, followed by  
170 examination of polished thin sections with an optical polarizing microscope (Eclipse LV100N  
171 POL, Nikon; Department of Marine Resources and Energy, Tokyo University of Marine Science  
172 and Technology). Subsequent qualitative X-ray fluorescence mapping of the thin sections was  
173 performed on a Bruker Tornado  $\mu$ XRF using a Rh source operating at 50 kV and 600  $\mu$ A under 20  
174 mbar vacuum (Laboratory for Ocean Geosciences, European Institute for Marine Studies). Spot  
175 size was 20  $\mu$ m and dwell times were 6 ms/pixel. Images of the areal distribution of elements along  
176 the thin sections were produced using M4 Tornado software package with spectra deconvolution  
177 and averaging every 3 pixels. All elements were represented by their  $K_{\alpha}$  emission lines except for  
178 Fe, for which  $K_{\beta}$  emission was chosen for imaging due to significant overlap of the  $K_{\alpha}$  Fe emission  
179 signal with the stronger  $K_{\alpha}$  emission of Mn in the samples. Scanning electron microscope (SEM)  
180 imaging and energy dispersive X-ray analysis (EDX) using a FEI XL30 ESEM and an associated  
181 EDX system were performed in order to investigate mineral morphology and chemistry on a

182 smaller scale.

183 Bulk samples, separated pisoliths and matrix among the pisoliths were ground to fine powder  
184 in an agate mortar and sieved to less than 200 mesh in acid-washed stainless-steel sieves prior to  
185 the bulk mineralogy and geochemistry investigations.

186 Bulk mineralogy was determined by X-ray diffractometry (XRD) on the powdered samples  
187 mounted on glass slides by dispersing grains in alcohol. This standard specimen preparation is  
188 necessary when working with small amounts of samples. It provides an even coating of powder  
189 that adheres to the sample holder and helps alleviate problems with preferred crystal orientation.  
190 Instrumentation was a Siemens D500 X-ray diffractometer with Cu  $K_{\alpha}$  radiation (Department of  
191 Geology, University of Cincinnati). Scans were conducted from  $5^{\circ}$  to  $55^{\circ}$   $2\theta$  with a step size of  
192  $0.2^{\circ}$   $2\theta$  and a count time of 10 s/step. Quantification of the X-ray diffraction patterns was done by  
193 Rietveld refinement using the software Panalytical HighScore Plus and the reference patterns  
194 stored in the ICSD 2013 database distributed by FIZ Karlsruhe.

195 Bulk chemistry of the samples was determined by X-ray fluorescence (XRF) using a Rigaku  
196 3070 spectrometer (Department of Geology, University of Cincinnati). Sample powders were  
197 pressed into thin pellets using a Spex 3624B X-Press 20-ton press. Samples were analyzed for  
198 major and selected trace elements. Concentrations of major elements were calculated by multiple  
199 regression using data from a set of USGS and NIST standards selected to bracket the range of  
200 compositions in the samples. Trace elements were calibrated by simple regression after correcting  
201 for peak overlaps (e.g., Sr  $K_{\beta}$  on Zr  $K_{\alpha}$ ).

202 A set of powdered sub-samples (~50 mg each; bulk and pisoliths) were dissolved with HF-  
203 HCl-HNO<sub>3</sub> in clean Teflon vials for whole-rock elemental concentration and radiogenic isotopes  
204 measurements (Department of Geological Sciences, University of Florida). According to the

205 previous studies (Vassilev et al., 1958), the Mn-ore bed is composed of both ore (Mn- carbonates  
206 and oxyhydroxides) and detrital components. Therefore, we decided to investigate the chemical  
207 composition of both components. For this reason, we prepared another set of powdered sub-  
208 samples (bulk and pisoliths) for two-step dissolution. About 80 mg of sample powder was  
209 dissolved with 2M HCl for 2 hours on a hot (100°C) plate aiming at leaching of the ore component  
210 (Mn-carbonates and -oxyhydroxides) only. The resultant leachates were separated from the  
211 residues in clean Teflon vials and evaporated to dryness. The remaining residues (supposed to be  
212 detrital component) were further dissolved with HF-HNO<sub>3</sub>. Chemical compositions of produced  
213 solutions (bulk samples, leachates, and residues) were analyzed with Inductively Coupled Plasma  
214 Mass Spectrometry (ICP-MS) using Thermo-Finnigan Element 2 instrument, and Re and Rh as  
215 internal standards. Quantification of the results was done by external calibration using a  
216 combination of USGS rock standards (AGV-1, BCR-2, and BIR-1) and following methods  
217 described in Kamenov et al. (2008). The error for the trace elements was less than 5%.

218 Strontium, Nd and Pb isotopes were separated from bulk and pisolith samples (bulk,  
219 leachate, and residue) using standard ion-exchange procedures and measured on a Nu Plasma  
220 Multiple Collector Inductively Coupled Plasma Mass Spectrometer (MC-ICP-MS) following  
221 methods described in Kamenov et al. (2008). The reported <sup>87</sup>Sr/<sup>86</sup>Sr ratios are relative to NBS 987  
222 <sup>87</sup>Sr/<sup>86</sup>Sr=0.71025 (+/-0.00003, 2σ). The Nd isotopic compositions are relative to JNdi-1  
223 <sup>143</sup>Nd/<sup>144</sup>Nd=0.512115 (+/-0.000018, 2σ). The Pb isotope data are relative to the following values  
224 of NBS 981: <sup>206</sup>Pb/<sup>204</sup>Pb=16.937 (+/-0.004, 2σ), <sup>207</sup>Pb/<sup>204</sup>Pb=15.490 (+/-0.003, 2σ), and  
225 <sup>208</sup>Pb/<sup>204</sup>Pb=36.695 (+/-0.009, 2σ).

226 For C and O isotope analyses, bulk (carbonate) samples, separated pisoliths and standards  
227 were reacted in He purged exetainer vials (10 min at 110 mL/min He flow) with 100% phosphoric

228 acid in a water bath at 25°C. The C and O isotopic composition of the CO<sub>2</sub> headspace gas was  
229 analyzed on a Thermo Delta V Advantage isotope ratio mass spectrometer with a Thermo  
230 Gasbench II connected via a Conflo IV interface (Department of Geology, University of  
231 Cincinnati). The  $\delta^{13}\text{C}$  values of carbonates were normalized to the VPDB scale using LSVEC (-  
232 46.6‰) and NBS-19 (1.95‰). The  $\delta^{18}\text{O}$  values were normalized to the VPDB scale with NBS-18  
233 (-23.01‰) and NBS-19 (-2.2‰) following the recommendation of Kim et al. (2015). The O  
234 isotope acid fractionation factors that were used for calcite and rhodochrosite were 1.01030 (Kim  
235 et al., 2007) and 1.01012 (Friedman and O'Neil, 1977; amended from Sharma and Clayton, 1965),  
236 respectively. Precision and accuracy were determined by analyzing an independent calcite  
237 standard over the course of analyses (n=43). For  $\delta^{13}\text{C}$ , precision and accuracy were 0.11‰ (1 $\sigma$ )  
238 and 0.00‰, respectively. For  $\delta^{18}\text{O}$ , precision and accuracy were 0.09‰ (1 $\sigma$ ) and 0.01‰.

239 Stable Fe isotopes were studied in 20 samples according to the analytical protocol reported  
240 in Rouxel et al. (2008) at Pôle de Spectrométrie Océan, IUEM/Ifremer. About 50 mg of each  
241 powdered sample and georeference materials [BHVO-2 (Hawaiian basalt), Nod-A-1 (Atlantic Mn-  
242 nodule), and Nod-P-1 (Pacific Mn-nodule)] were put in 15 mL PFA beakers. Powders were  
243 dissolved in 2 mL concentrated (14.4M) ultrapure HNO<sub>3</sub> (obtained using TFE sub-boiling  
244 distillation system, hereafter referred as SB grade) and between 1 to 2 mL of concentrated Trace  
245 Metal™ (Fisher Scientific) grade HF. Solutions were evaporated to dryness on a hot plate at 80°C.  
246 Then, we added 2 mL concentrated SB grade HNO<sub>3</sub> and 2 mL 6M SB grade HCl (thus forming  
247 *aqua regia*). Solutions were evaporated to dryness on a hot plate at 90°C. After that, we added 1  
248 mL 5M HCl with 10  $\mu\text{L}$  of 30% (v/v) H<sub>2</sub>O<sub>2</sub> in each beaker, closed the beakers and put them on a  
249 warm (60°C) plate for 1 h. The beakers were cooled down (20°C) and the solutions were ready for  
250 column load.

251 For Fe isotope separation we used 2.0 mL (wet volume) of anion-exchange resin AG MP-1  
252 placed in polypropylene columns. All diluted acids were prepared from SB-grade concentrated  
253 acids. Before the sample load, the resin was washed with 10 mL 3M HNO<sub>3</sub>, 10 mL 18 MΩ cm<sup>-1</sup>  
254 H<sub>2</sub>O, 5 mL 1.2M HCl, and conditioned with 2 mL 5M HCl. 1 mL of each sample solution was  
255 loaded in the columns. The matrix fraction was eluted with 14.5 mL 5M HCl. Fe was eluted with  
256 14 mL 1.2M HCl in PFA beakers. After evaporation of the Fe eluate at 90°C, we added 2 mL  
257 0.28M HNO<sub>3</sub> in the beakers and transferred the solutions into 2 mL PFA vials.

258 Fe isotope compositions were determined with a Neptune (Thermo-Scientific) MC-ICP-MS  
259 using medium or high-resolution mode. It involves both “sample-standard bracketing” and  
260 “internal normalization” using Ni of known isotope composition (Weyer and Schwieters, 2003;  
261 Poitrasson and Freydier, 2005; Rouxel et al., 2005). All analyses are reported in delta notation  
262 relative to the IRMM-014 standard, expressed as δ<sup>56</sup>Fe. Based on >50 replicate dissolutions,  
263 purifications, and analyses of internal standard BHVO-2, we have obtained: δ<sup>56</sup>Fe = 0.09 ± 0.07‰  
264 (2 SD). Results for Mn-nodules Nod-A-1 and Nod-P-1 yielded δ<sup>56</sup>Fe = -0.39 ± 0.06‰ (2 SD) and  
265 -0.51 ± 0.06‰ (2 SD), respectively, which is indistinguishable, within analytical error, from  
266 previously published values (Asael et al., 2013; Marcus et al., 2015; Rolison et al., 2018).

267

268

## 269 4. Results

270

### 271 4.1. Petrography

272

273 Most samples collected from the Mn-ore layer at the mine were highly pisolitic (Fig. 2)

274 comprising tan to brownish-red, concentrically-laminated pisoliths (Fig. 3A, B) set in a greenish-  
275 tan matrix. Pisoliths are 1 to 2 cm in diameter and show some tendency to increase up-layer in  
276 both size and abundance. Thin section microscope observations revealed that the grain size for  
277 both the carbonate and the aluminosilicate components was exceeding small and the ore matrix  
278 looked greyish-brown to light-brown (images not shown). Optical microscopy observations along  
279 with X-ray fluorescence mapping showed that the pisolith concentric layers were of two types:  
280 carbonate-rich and aluminosilicate-rich (Figs 3C, D; 4). Carbonate-rich layers were composed of  
281 Mn- and Mn-Ca-carbonates (Fig. 4A, B, C). They alternated with layers enriched in elements  
282 typical for detrital aluminosilicate component: Al, Si, Fe, Rb, and Zr (Fig. 4D, E, F, G, H). The  
283 SEM imaging showed that the carbonate-rich layers contained large crystals of Mn-carbonate (Fig.  
284 5A), whereas the aluminosilicate-rich layers were composed of sub-micron spheres of silica and  
285 Mn-carbonate (Fig. 5B), and, possibly, clays.

286 An EDX survey of the composition of pisoliths and matrix showed (Table 2) the same  
287 distribution as in the X-ray mapping: the matrix was primarily Al- and Si-rich, whereas the  
288 pisoliths were composed predominantly of Mn and Ca.

289

#### 290 *4.2. Mineralogy*

291

292 The strata below and above the Mn-ore layer are composed mainly of quartz, plagioclase,  
293 and clay minerals (illite/smectite and kaolinite). Where carbonates are present, they are calcite or  
294 dolomite rather than one of the Mn-carbonates (Table 1).

295 The Mn-ore layer and its low-grade equivalents also include the same detrital components.  
296 They differ from the host strata in having Mn-carbonates as well. The amount and type of Mn-

297 carbonates varies laterally. In the area of the Obrochishte mine, the Mn-ore layer is mainly  
298 composed of rhodochrosite ( $\text{MnCO}_3$ ) with some kutnahorite [ $\text{Ca}(\text{Mn}^{2+}, \text{Mg}^{2+}, \text{Fe}^{2+})(\text{CO}_3)_2$ ] at the  
299 base and lesser amounts of detrital components (Table 1). This assemblage is consistent with the  
300 results of Vassilev et al. (1958). However, northeast of the Obrochishte mine where the ore-  
301 equivalent horizon is crossed by drill holes, kutnahorite dominates over rhodochrosite and non-ore  
302 components roughly equal ore minerals. To the south and southwest of the Obrochishte mine  
303 where the ore interval crops out (Fig. 1), it is mostly composed of quartz, plagioclase, and clays  
304 with subordinate amounts of Mn-calcite [ $(\text{Ca}, \text{Mn})\text{CO}_3$ ] and kutnahorite (Table 1). Our samples  
305 are mostly free of Mn-oxides. Trace amounts of pyrolusite ( $\text{MnO}_2$ ) and todorokite [ $(\text{Na}, \text{Ca},$   
306  $\text{K})_2(\text{Mn}^{4+}, \text{Mn}^{3+})_6\text{O}_{12} \cdot 3-4.5(\text{H}_2\text{O})$ ] were found in some samples (OBR-7-3178, OBR-7-4130,  
307 OBR-8-A, OBR-9-3884) at amounts too low to be quantified by the Rietveld refinement (therefore,  
308 not in Table 1). Rare thin (0.1-0.5 mm) pyrite veins cross the ore matrix (Figs 3E, F, G; 6). They  
309 have thin rhodochrosite bands (Fig. 3E) and are altered along thin cracks at some places (Fig. 3H).

310

### 311 4.3. Geochemistry

312

313 Similar to the distribution of minerals, the host strata below and above the Mn-ore layer lack  
314 significant Mn content ( $\text{MnO}=0.04-0.46$  wt.%; Table 3). Content of the most other elements in  
315 bulk rock samples are similar in the ore layer and in the host strata except for Ca, Fe, Pb, and Zn,  
316 which are higher in the host rocks, and Mn, Co, Mo, Ni, V, P and total rare earth elements (REE),  
317 which are substantially higher in the ore interval. The ore interval shows considerable lateral  
318 variation in geochemistry. In the Obrochishte mine area, the Mn-ore layer contains less  $\text{SiO}_2$ ,  
319  $\text{Al}_2\text{O}_3$ ,  $\text{Fe}_2\text{O}_3$ ,  $\text{K}_2\text{O}$ , and  $\text{S}_{\text{tot}}$ , and more MnO, MgO, and  $\text{C}_{\text{tot}}$  than both the host rocks and the Mn-

320 ore interval sampled at the outcrops and drill holes outside the mine area (Table 3). Across the  
321 Mn-ore layer CaO and Fe<sub>2</sub>O<sub>3</sub> concentrations decrease upward (Table 3). Overall, the picture from  
322 mineralogy and bulk geochemistry is that the sedimentary rocks are a mixture of a detrital  
323 component of fixed composition and a (presumably) authigenic component that varies from Ca-  
324 rich to Mn-rich.

325 Within the authigenic component, there are important variations that likely relate to  
326 depositional conditions. The relationship between organic carbon (C<sub>org</sub>) and total sulfur (S<sub>tot</sub>)  
327 content is often used to characterize low-oxygen environments (e.g., Potter et al., 2005). Organic  
328 carbon concentrations in the studied samples are low, ranging from 0.1 to 1.3 wt.% with an average  
329 of 0.4 wt.% (Table 3). Total sulfur content ranges to higher values, with some exceeding 2 wt.%  
330 (Table 3). Many of the studied samples show the typical correlation between C<sub>org</sub> and S<sub>tot</sub> that is  
331 found in normal marine sediments (Fig. 7) (Berner, 1982; Raiswell and Berner, 1986; Morse and  
332 Berner, 1995). There is another group of samples, however, that has excess S, which is usually  
333 interpreted to indicate free H<sub>2</sub>S in the water column (euxinic conditions). There is a tendency for  
334 the S<sub>tot</sub> concentration in these rich in S samples to increase upwards across the Mn-ore layer, but  
335 there are exceptions.

336 Because the ore consists of a mixture of detrital components and authigenic material in two  
337 contrasting textural forms (matrix and pisoliths), it is useful to view the geochemistry of major and  
338 trace elements in terms of separate fractions. The concentrations of trace elements and some major  
339 elements in the bulk, pisolith, leachate and residue fractions of the samples are reported in Table  
340 4.

341 The chemistry of the studied sample fractions (leachates and residues) shows some  
342 interesting features (Table 4). The major part (>50%) of the investigated elements (Mg, Fe, Mn,

343 Na, K, Li, Sc, Ti, V, Cr, Co, Zn, Ga, Rb, Zr, Nb, Cs, Ba, Hf, Ta, and Th) in the host rock (sample  
344 OBR-8-A) are in the residual fraction (Table 4). Only P, Ni, Cu, Y, Pb, and U reside mostly (>50%)  
345 in the leachate fraction of the host rock. REE and Sr are equally distributed in both fractions.

346 The residues of the Mn-ore layer (sampled in the mine and in a drill hole) and pisoliths (Table  
347 4) contain the major part of K, Sc, Ti, Cr, Ga, Rb, Zr, Nb, Cs, Hf, and Ta. The leachate fraction of  
348 this layer and of the pisoliths contains most (>50%) of Ca, Mg, Mn, Na, P, Li, V, Co, Ni, Zn, Sr,  
349 Y, Ba, REE, Pb, Th, and U. Cu is almost in equal proportions in both fractions.

350 The vertical distribution of some elements across the Mn-ore layer sampled at the mine show  
351 some correlation with the ore mineralogy. Major ore mineral in the lowermost two samples is  
352 kutnahorite whereas rhodochrosite is the only ore mineral in the rest of the samples upward (see  
353 sub-section 4.2 and Table 1). Li and V are mostly in the residue in the lowermost two kutnahorite-  
354 containing samples and in the leachate in the upper rhodochrosite samples. Fe and Pb are mostly  
355 in the leachate fraction of the pisoliths in the lower kutnahorite-containing samples and  
356 progressively decrease upward through the rhodochrosite samples. Na is mostly in the leachate of  
357 the pisoliths, but lower in the lowermost two kutnahorite-containing samples. Cu is mostly in the  
358 leachate of pisoliths in the lower two kutnahorite samples and mostly in the residue in the upper  
359 rhodochrosite samples.

360 In order to estimate the magnitude of elemental enrichment of the Mn-ore layer with respect  
361 to the host rocks we compared the averages of the leachate compositions of the bulk samples from  
362 the Obrochishte mine (samples OBR-11: Mn-ore layer), one drill hole (samples OBR-5: Mn-ore  
363 layer), and a host rock sample (OBR-8-A), and of the pisoliths from the Mn-ore layer at the  
364 Obrochishte mine (samples OBR-11-1.2P, -1.8P, -3.8P, -4.4P, -5.1P, -6.1P). This sample selection  
365 is based on the assumption that the residues of all studied samples represent detrital component

366 delivered to the sedimentary basin from the same provenance and with similar composition.

367 Ca concentration in the leachates of the host rocks (~20%) is 3-5 times higher than that of  
368 the leachates of the Mn-ore layer and its pisoliths (Table 4). In contrast, Mn, Mg, and Fe  
369 concentrations in the leachates of both the Mn-ore layer and its pisoliths are higher than those of  
370 the host rocks. Mn and Mg contents are even 2-3 and 1-2 (respectively) orders of magnitude higher  
371 than those of the host rock. Only K, Ti, Cu, Nb, Hf, Ta, and Pb have similar concentrations in the  
372 leachates of both types of samples: Mn-ore layer (and its pisoliths) and host rock. Contents of all  
373 the other studied elements (V, Co, Ba, Na, Li, Ni, REE, Th, Zn, Ga, Cr, Rb, Sr, Y, Zr, Cs, and U)  
374 are higher in the leachates of the Mn-ore layer (and pisoliths) than in those of the host rock. The  
375 concentrations of Na, Li, Ni, REE, and Th are 1 and those of V, Co, and Ba are 1-2 orders of  
376 magnitude higher than those of the host rock. Pisoliths are richer in P, Y, heavy REE (Ho-Lu), and  
377 U than the Mn-ore layer (bulk) and host rock, but poorer in Th than the Mn-ore layer (Table 4).  
378 They are richer in Mn, Ca, and (particularly) P than the matrix among them (Table 3).

379 The total content of REE ( $\Sigma$ REE) in the studied Mn-ore samples (Table 4) is slightly lower  
380 than that of the average upper continental crust (UCC) (McLennan, 1989).  $\Sigma$ REE in the  
381 background samples (below and above the Mn-ore bed) are even less than the  $\Sigma$ REE of the Mn  
382 ores (Table 4, sample OBR-8-A). Over 60% of the content of each rare earth element in the studied  
383 Mn ore samples is within the leachable by 2M HCl fraction and only <40% of the REE content is  
384 in the residue supposed to be composed of detrital aluminosilicates (Table 4; Fig. 8A, B). Selected  
385 pisoliths show similar REE composition with over 70% of the REE content being within the  
386 leachable fraction (Table 4; Fig. 8C). The REE distribution patterns of the Mn ores and their  
387 components (Fig. 8A-D; Table 4) are broadly similar to those of the upper continental crust (Fig.  
388 8F; McLennan, 1989) with light REE (LREE) enrichment, flat heavy REE (HREE) distributions

389 and negative Eu anomaly ( $\text{Eu}/\text{Eu}^* < 1$ ). The only difference between them and those of the upper  
390 continental crust is the negative Ce anomaly ( $\text{Ce}/\text{Ce}^* < 1$ ) (Fig. 8A-D; Table 4). The negative Ce  
391 anomaly is well pronounced at the REE distribution patterns of both the bulk samples  
392 ( $\text{Ce}/\text{Ce}^*_{\text{average}} = 0.69$ ) and the 2M HCl leachates ( $\text{Ce}/\text{Ce}^*_{\text{average}} = 0.79$ ), whereas it is negligible at the  
393 REE distribution patterns of the residues ( $\text{Ce}/\text{Ce}^*_{\text{average}} = 0.90$ ) (Fig. 8A-D; Table 4). REE  
394 distribution patterns of the leachates of both the Mn ores and background rocks are similar with  
395 the only difference that the REE contents in the Mn ores are about five times more than those in  
396 the background rocks (Fig. 8A, B, F).

397

#### 398 *4.4. Isotope geochemistry*

399

##### 400 *4.4.1. C and O isotopes*

401 C and O stable isotope values of studied samples (Table 5), when plotted against one another,  
402 fall into two groups (Fig. 9A). One has  $\delta^{18}\text{O}_{\text{PDB}}$  of 0‰ to -4‰, and  $\delta^{18}\text{O}_{\text{PDB}}$  is independent of  
403  $\delta^{13}\text{C}_{\text{PDB}}$  (Fig. 9A). The other group has a strong correlation of  $\delta^{18}\text{O}_{\text{PDB}}$  to  $\delta^{13}\text{C}_{\text{PDB}}$ , with lighter O  
404 isotope values, ranging from -12‰ to -3‰. This second group comes from sample sites (##6, 7,  
405 8, and 9) located in the southern part of the Ruslar Formation with larger content of detrital  
406 component (clays and sandstones) (Fig. 1B). They plot along an array between typical fresh water  
407 and seawater. Although mineralized, this sample group has lower MnO content:  $\leq 10\%$ . These  
408 samples are strongly enriched in Cu, Pb, and Zn (3 to 8 times in bulk composition) compared to  
409 the fully marine group, which in turn is strongly enriched in Cl, S, and V with lesser enrichment  
410 in Co and Ni. The number of leachate samples for the first sample set was too small to make valid  
411 comparisons.

412 Another aspect of C-O isotope geochemistry is seen in a plot of  $\delta^{13}\text{C}_{\text{PDB}}$  against Mn content  
413 of the studied samples (Fig. 9B). This pair of variables also shows two distinct trends, but involving  
414 a somewhat different grouping of samples from the  $\delta^{18}\text{O}_{\text{PDB}} - \delta^{13}\text{C}_{\text{PDB}}$  plot (Fig. 9A). One set of  
415 samples (Group I) clusters around the value for seawater bicarbonate ( $\delta^{13}\text{C}_{\text{PDB}} = 0\text{‰}$ ) and is  
416 independent of Mn concentration. This set of samples is substantially larger than the other set and  
417 comes from stratigraphically lower positions in the Mn-ore layer in the mine area. The other  
418 sample set (Group II) has lighter C isotope values,  $-5\text{‰}$  to  $-25\text{‰}$ , and they correlate inversely to  
419 the MnO concentration (Fig. 9B). The first array has  $\delta^{13}\text{C}_{\text{PDB}}$  values consistent with derivation  
420 from seawater  $\text{HCO}_3^-$ , whereas the second array has some to all of its C derived from decay of  
421 organic matter, perhaps including some oxidized methane for samples with  $\delta^{13}\text{C}$  in the  $-25$  to  $-$   
422  $32\text{‰}$  range. The lightest  $\delta^{13}\text{C}_{\text{PDB}}$  value,  $-25\text{‰}$ , corresponds to modern C isotope values for organic  
423 matter in sediments on the shelf off the mouth of the Danube River,  $-26\text{‰}$  to  $-23\text{‰}$  (Galimov et  
424 al., 2002), so the second array spans the complete range from 100% organic-sourced C to 100%  
425 seawater-sourced carbon. The bulk chemistry of the two populations identified on Figure 9B shows  
426 enrichments in Group I in Pb and Zn when compared to Group II, which in turn shows strong  
427 enrichments in Co, Ni, and S and smaller enrichments in V, Cr, and Cu. For the leachates, a smaller  
428 sample set, the Co and Ni enrichments seen in the bulk chemistry do not appear, but V and Cu  
429 remain higher in Group II samples compared to Group I. Pb continues to be enriched in Group I,  
430 but Zn does not show enrichment.

431

#### 432 4.4.2. Sr, Nd and Pb isotopes

433  $^{87}\text{Sr}/^{86}\text{Sr}$  in the bulk samples shows a range from 0.70826 to 0.70937 (Table 5). The leachates  
434 show lower values compared to the bulk samples and cluster around the expected seawater Sr

435 isotopic composition at 31 My (Fig. 10). A t-test shows that the means of the two sets of data are  
436 statistically different ( $P = 0.001$ ). The residues show much more radiogenic  $^{87}\text{Sr}/^{86}\text{Sr}$  when  
437 compared to leachates and bulk, with values ranging from 0.70967 to 0.72038 (Table 5). Sample  
438 size for the residues is too small for effective statistical evaluation.

439 Bulk samples show a relatively narrow range for  $\epsilon\text{Nd}$ , between -6.7 and -8.1 (Table 5).  
440 Leachates also show a narrow range for  $\epsilon\text{Nd}$ , between -6.0 and -7.4. Again, the means are  
441 significantly different ( $P = 0.009$ ). A portion of the leachates overlap with the expected Nd isotopic  
442 composition for Atlantic and Tethys seawater at 31My, although some leachates and most of bulk  
443 samples extend to more negative  $\epsilon\text{Nd}$ , towards the residues (Fig. 11). As can be seen from Figure  
444 11, the residues show the most negative  $\epsilon\text{Nd}$  as low as -12.1, from all of the analyzed samples  
445 (Table 5).

446 In contrast to Sr and Nd isotopes, Pb isotopes have very similar median values for bulk and  
447 leachate compositions and show the same modes on histograms. Statistically, the means for bulk  
448 and leachate sample sets are the same for  $^{206}\text{Pb}/^{204}\text{Pb}$  ( $P = 0.33$ ) and for  $^{207}\text{Pb}/^{204}\text{Pb}$  ( $P = 0.83$ ),  
449 whereas the means for  $^{208}\text{Pb}/^{204}\text{Pb}$  are somewhat different ( $P = 0.02$ ). The residence time of Pb in  
450 seawater (unlike that of Sr and Nd) is very short (30-400 years) and Pb reflects local weathering  
451 inputs (e.g., Basak and Martin, 2013). Thus, the dissolved and particulate Pb fractions should have  
452 similar isotope composition. Means for the three isotope ratios are:  $^{206}\text{Pb}/^{204}\text{Pb}$  of bulk samples,  
453 18.95 and leachate samples, 18.89;  $^{207}\text{Pb}/^{204}\text{Pb}$  – 15.661 and 15.663, respectively;  $^{208}\text{Pb}/^{204}\text{Pb}$  –  
454 38.80 and 38.70, respectively. Sample OBR-8-A departs significantly from others in Pb isotope  
455 values, but it is mostly composed of  $\text{CaCO}_3$  rather than of  $\text{MnCO}_3$ . Therefore, we have excluded  
456 it from the statistical analysis. We only have Pb isotopic data from 4 residues, so statistical  
457 comparisons are difficult. However, the similarity of the whole-rock and leachate values implies

458 that the residues should also be similar. Also, the means for the residue isotopes are within 1% of  
459 the means for the leachates and whole rock.

460

#### 461 *4.4.3. Fe isotopes*

462 Iron isotope composition ( $\delta^{56/54}\text{Fe}$ ) of the whole-rock samples from the Mn-ore layer at the  
463 Obrochishte mine ranges from -0.16‰ to +0.16‰ (samples OBR-11-...; Table 5) and does not  
464 clearly correlate to other geochemical parameters such as concentrations of  $\text{Al}_2\text{O}_3$  and MnO  
465 (Tables 3, 4). In the areas lateral to the mine, the whole-rock  $\delta^{56/54}\text{Fe}$  range is greater: -0.33‰ to  
466 +0.24‰. The pisolith  $\delta^{56/54}\text{Fe}$  (analyzed at the Obrochishte mine only) has a distinct trend to lighter  
467 values relative to the host whole-rock data and decreases upward within the Mn-ore layer (Table  
468 5). The lower Mn-ore beds (samples OBR-11-1.2 to OBR-11-3.8) have average  $\delta^{56/54}\text{Fe}_{\text{pisolith}} = -$   
469 0.08‰ (Table 5), whereas the upper Mn-ore beds (samples OBR-11-4.4 to OBR-11-6.1) have  
470 average  $\delta^{56/54}\text{Fe}_{\text{pisolith}} = -0.36\text{‰}$ .

471

472

## 473 **5. Discussion**

474

### 475 *5.1. Mineralogy of Mn-ore layer*

476

477 The absence of Mn-minerals in the host strata below and above the Mn-ore layer (Table 1)  
478 suggests that precipitation was caused by an abrupt change in geochemical conditions. Maynard  
479 et al. (1990) observed a similar abrupt appearance of Mn in the Molango deposit of Mexico and  
480 related it to a rise in sea-level that allowed penetration of new water into the depositional basin.

481 For Obrochishte deposit, the occurrence of Mn-oxides mostly in the outcrop samples is in  
482 accordance with the previous suggestion (Vassilev et al., 1958) that these are secondary minerals  
483 formed as a weathering product of the primary Mn-carbonates. The Mn-ore layer crossed at the  
484 Obrochishte mine is richer in Mn-minerals (rhodochrosite and kutnahorite) than at the other  
485 studied sites (Table 1). We interpret this lateral variability in the mineralogical composition of the  
486 Mn-ore layer as a result of different degree of dilution of the Mn-minerals with detrital component  
487 (quartz, plagioclase, and clays). The area of the Mn deposit is relatively small (Fig. 1) and it does  
488 not seem plausible to assume that the lateral variability in the mineralogy of the Mn-ore layer is  
489 due to spatial variations in the conditions of Mn-mineral precipitation.

490

#### 491 *5.2. REE constraints on redox conditions of Mn-carbonate precipitation*

492

493 The close resemblance of the REE distribution patterns of the Mn-ore residues (after 2M  
494 HCl leaching) (Fig. 8A-D; Table 4) to those of the average UCC (Fig. 8F) suggests that the residues  
495 are detrital (terrigenous) component. The negative Ce anomaly in the REE distribution patterns of  
496 the 2M HCl leachable component of the Mn-ores is visible at the REE distribution patterns of the  
497 bulk Mn-ore (Fig. 8A, B) as the latter is the sum of both leachable and residual (without Ce  
498 anomaly) components. The 2M HCl leachable component is mostly composed of authigenic Mn-  
499 carbonates and therefore, it is essential to understand the source of this anomaly and its  
500 implications for the source of Mn in the ore layer.

501 The location of the Mn-ore layer within a sedimentary rock sequence (Oligocene Ruslar  
502 Formation) suggests that it is a sedimentary formation (e.g., Johnson et al., 2016). Therefore, any  
503 aspect of its deposition needs to consider the conditions in the depositional basin. The Ruslar

504 Formation in general, had formed at the western margin of the Western Black Sea basin, which  
505 was progressively opening during the Oligocene (Nikishin et al., 2015). According to the  
506 paleotectonic reconstructions (Nikishin et al., 2015) during this epoch, the uplift of the Pontides  
507 orogenic area limited the open oceanic connection of the basin with the Tethys. This reduced the  
508 ventilation of the Western Black Sea, which in turn led to suboxic to anoxic conditions in the water  
509 column (Sachsenhofer et al., 2009; Mayer et al., 2017). Therefore, when discussing the  
510 geochemistry of the Mn deposit formed at the western margin of the Oligocene Black Sea, it seems  
511 reasonable to use as a proxy the recent anoxic Black Sea (see also Schulz et al., 2005).

512 The modern Black Sea water body is vertically stratified in three layers (from surface to  
513 bottom): oxic, suboxic and anoxic (Lewis and Landing, 1991; German et al., 1991; Schijf et al.,  
514 1991). The suboxic layer is the zone where sharp gradients of dissolved as well as particulate  
515 elements (Mn, Fe, and REE) are found (German et al., 1991; Schijf et al., 1991). Its thickness  
516 varies from a few meters up to as much as 80 m with an average of ~26 m (Glazer et al., 2006a,  
517 b). Particulate Mn concentration is high throughout the suboxic layer, but its maximum occurs at  
518 the top of this layer coincident with a minimum in dissolved total REE and a minimum in  $Ce/Ce^*$   
519 (German et al., 1991). The maximum of particulate Fe content is shifted down, at the transition  
520 from the suboxic to the anoxic layer. Average  $Ce/Ce^*$  (chondrite-normalized) of dissolved REE is  
521 0.39 in the oxic layer, 0.08 at the oxic-suboxic transition, 0.34 in the suboxic layer proper and 0.86  
522 in the anoxic layer (calculated from the data reported by German et al., 1991). We have not found  
523 any data for the REE composition of the corresponding particulate material. A rough estimate can  
524 be calculated by assuming the observed dissolved values are the residual after extraction of  
525 dissolved REE by adsorption to newly-formed Mn-oxide particles. The very low  $Ce/Ce^*$  value at  
526 the oxic-suboxic boundary requires a positive particulate Ce anomaly of about 1.80, based on the

527 difference between the dissolved values of La, Ce, and Nd in the oxic and transition layers. Using  
528 the same approach, the suboxic layer itself would produce particles with Ce/Ce\* of about 0.84 (see  
529 online data supplement for details). These numbers are sensitive to the exact choice of samples to  
530 be included in each category, but they do give an indication of what is to be expected for different  
531 levels in the water column.

532 The Ce/Ce\* of the Mn-ore leachates (Fig. 8A-D) ranges from 0.61 to 1.03 with an average  
533 of 0.77 with no apparent trend across the Mn-ore layer. For comparison, two other circum-Black  
534 Sea deposits have reported REE data: Binkiliç, which averages 0.80 for Ce/Ce\* and Nikopol,  
535 which has 1.05 in oxide ore and 0.91 in carbonate ore [calculated from data of Gültekin and Balci  
536 (2018) and Varentsov et al. (1997), respectively]. Thus, the REE in the Mn-ores around the  
537 Oligocene paleo-Black Sea could reasonably have been acquired by scavenging of the dissolved  
538 REE ions by particulate Mn-oxides, which then sank to the seafloor and were converted to MnCO<sub>3</sub>  
539 during diagenesis. The values seen suggest formation in the lower part of the suboxic zone. The  
540 Ce/Ce\* values are also consistent with a portion of the REE being directly incorporated in MnCO<sub>3</sub>  
541 in the seawater column (see model of Konovalov et al., 2006). The carbonate phase would not  
542 have a preference for Ce<sup>4+</sup> so its REE distribution pattern would be the same as that of the seawater  
543 parcel where precipitation occurred. The amount of this authigenic MnCO<sub>3</sub> is hard to estimate  
544 because of the uncertainty in the value for the Mn-oxides, but 20 to 30% could easily be  
545 accommodated (see calculations in online data supplement). In summary, Ce/Ce\* for the  
546 Obrochishte Mn-ore layer is consistent with precipitation of Mn as Mn<sup>4+</sup>-oxide in the suboxic layer  
547 of the seawater column in a euxinic basin similar to the modern Black Sea, with some Mn going  
548 directly into MnCO<sub>3</sub> as Mn<sup>2+</sup> at the top of the anoxic zone.

549

550 *5.3. Controls on the trace element content of the Mn-ore layer*

551

552 *5.3.1. Crystallography and mineralogy controls on the Sr and Ba concentrations in Mn-ore layer*

553 The lowermost part of the Mn-ore layer crossed at the Obrochishte mine (OBR-11-1.2 and  
554 OBR-11-1.8) is richer in Sr and Ba than the middle-upper part of this layer sampled in the  
555 Obrochishte mine (Table 4). The mineralogy studies did not reveal any single mineral phases of  
556 Sr and Ba in any sample. Hence, Sr and Ba are either hosted in the crystal lattice of some minerals,  
557 or they are adsorbed on the mineral surfaces. Chemistry of the acid-leached fraction (presumably  
558 composed mainly of Mn-carbonates) and residual fraction (presumably composed mainly of  
559 aluminosilicates) showed that Sr and Ba were mostly (>70%) hold in the Mn-carbonates  
560 (excluding Ba in the lower part of the Mn-ore layer drilled at site #5) (Table 4). We have not  
561 performed detailed partitioning chemistry analysis that would allow us to precisely determine the  
562 carbonate-bound and adsorbed fractions of these two elements. Therefore, we may consider (at  
563 first approximation) that a major part of the elements leached according to our protocol (see 3.2)  
564 are carbonate-bound. Thus, the vertical distribution of Sr and Ba across the Mn-ore layer in the  
565 mine (site #11) seems to be crystallographically controlled.

566 The lowermost Mn-ore layer contains kutnahorite as a major ore mineral along with  
567 rhodochrosite, whereas the middle-upper Mn-ore layer contains only rhodochrosite (Table 1). The  
568 only possible structural site for Sr<sup>2+</sup> and Ba<sup>2+</sup> substitution in rhodochrosite (MnCO<sub>3</sub>) is that of Mn<sup>2+</sup>  
569 in octahedral coordination, whereas the structural sites for Sr<sup>2+</sup> and Ba<sup>2+</sup> substitution in kutnahorite  
570 [Ca(Mn, Mg, Fe)(CO<sub>3</sub>)<sub>2</sub>] are those of Ca<sup>2+</sup>, Mg<sup>2+</sup> and Fe<sup>2+</sup> in addition to that of Mn<sup>2+</sup>. According  
571 to the Goldschmidt's rules of substitution of ions in crystals (Goldschmidt, 1954) from charge  
572 considerations Sr<sup>2+</sup> and Ba<sup>2+</sup> might substitute for Mn<sup>2+</sup>, Ca<sup>2+</sup>, Mg<sup>2+</sup> and Fe<sup>2+</sup> in the crystal lattices

573 of both carbonates. Then, the governing control for such a substitution is the ionic radius of the  
574 replacing and replaced ions. For an extensive substitution, the radius of the replacing ion must not  
575 differ from the radius of the replaced ion by more than 15% (Goldschmidt, 1954). The ionic radius  
576 of  $\text{Mn}^{2+}$  in six-fold coordination (like that in rhodochrosite) is 0.75-0.91 Å (depending on the low  
577 or high spin, respectively), whereas the radii of  $\text{Sr}^{2+}$  and  $\text{Ba}^{2+}$  in the same coordination are 1.21  
578 and 1.44 Å, respectively (Whittaker and Muntus, 1970). Hence,  $\text{Sr}^{2+}$  and  $\text{Ba}^{2+}$  substitution for  $\text{Mn}^{2+}$   
579 in rhodochrosite crystal lattice is difficult:  $r_{\text{Sr}}$  and  $r_{\text{Ba}}$  must be  $\leq 1.05$  Å (i.e., 115% of the  $\text{Mn}^{2+}$ -site  
580 radius) for an extensive substitution. However, the theoretical possibilities of  $\text{Sr}^{2+}$  and  $\text{Ba}^{2+}$   
581 incorporation in the kutnahorite crystal lattice are different. In addition to the structural site of  
582  $\text{Mn}^{2+}$ , which obviously cannot easily accommodate these elements, there are also those of  $\text{Ca}^{2+}$ ,  
583  $\text{Mg}^{2+}$  and  $\text{Fe}^{2+}$ . The ionic radii of  $\text{Mg}^{2+}$  and  $\text{Fe}^{2+}$  in six-fold coordination are even smaller than that  
584 of  $\text{Mn}^{2+}$  (0.80 and 0.86 Å, respectively), which means that their structural sites cannot easily  
585 accommodate  $\text{Sr}^{2+}$  or  $\text{Ba}^{2+}$ . However, the structural site of  $\text{Ca}^{2+}$  ( $r_{\text{Ca}} = 1.08$  Å; Whittaker and  
586 Muntus, 1970) can easily accept substitution of ions up to 1.24 Å (within the 15% substitution  
587 tolerance), which is perfect for  $\text{Sr}^{2+}$  accommodation ( $r_{\text{Sr}} = 1.21$  Å), but more difficult for  $\text{Ba}^{2+}$   
588 accommodation ( $r_{\text{Ba}} = 1.44$  Å). This explains the higher concentrations of Sr in the lowermost Mn-  
589 ore layer containing kutnahorite than in the middle-upper Mn-ore layer having only rhodochrosite.  
590 Barium may instead reside in small amounts (<4%, the detection limits of XRD) of single Ba-  
591 mineral like barite that has not been detected during our XRD investigations. The lowermost Mn-  
592 ore layer contains on average 190 ppm Ba, whereas the middle-upper Mn-ore layer (samples OBR-  
593 11-4.4 to -6.1) has on average 160 ppm Ba (Table 4). Its enrichment in the lower Mn-ore layer  
594 may reflect a more oxidizing depositional environment, which is supported by the presence of  
595 excess S (i.e., S in excess of that predicted from the  $C_{\text{org}}$  content) in the middle-upper Mn-ore

596 layer:  $S_{\text{excess lower}} = 100 \text{ ppm}$ ,  $S_{\text{excess upper}} = 1300 \text{ ppm}$  (Table 3).

597

### 598 *5.3.2. Euxinia control on Fe, Zn, Cu, Cr, Ni, Co, and Mo contents of Mn-ore layer*

599 Principal minerals in the Mn-ore layer are rhodochrosite and kutnahorite (Table 1).  
600 Reasonably, major part of Mn, Ca, and Mg in this layer (and in the extracted pisoliths) is in the  
601 leachate fraction (Table 4), i.e., mostly in the Mn-carbonates. In addition to these major elements,  
602 a number of trace elements (Na, P, Li, V, Co, Ni, Zn, Sr, Y, Ba, REE, Pb, Th, and U) is also mostly  
603 contained in the leachate fraction of the Mn-ore layer (Table 4). The enrichment of the Mn-ore  
604 layer in these trace elements relative to the host rocks is likely a result of the processes that led to  
605 the deposition of this layer in the Western Black Sea during the Early Oligocene.

606 Major accumulations of sedimentary Mn are thought to require the presence of a large body  
607 of anoxic seawater to provide a sufficient reservoir of dissolved Mn (e.g., Maynard, 2014). The  
608 required anoxia can develop in two ways: a restricted marine basin, or an intense oxygen-minimum  
609 zone in the open ocean (Maynard, 2010). In the former case, the basin becomes euxinic: i.e., there  
610 is free  $\text{H}_2\text{S}$  dissolved in the bottom water. In both cases, the Mn deposit forms above the anoxic  
611 water where suboxic conditions impinge on the seafloor.

612 Consistent with this model, REE evidence from studied deposit suggests that the Mn-ore  
613 layer formed in suboxic seawater conditions (see 5.2). Euxinic conditions offshore from the area  
614 of deposition are indicated by several studies of the petroleum potential of the Ruslar Formation  
615 (e.g., Sachsenhofer et al., 2009; Mayer et al., 2017). We also see some evidence for euxinic  
616 conditions at the area of Mn deposition, based on the excess S found in some of the samples (Fig.  
617 7). It would appear that seawater in the deeper Early Oligocene Western Black Sea basin was  
618 anoxic, while on the shallow shelf it was generally suboxic (see Mayer et al., 2017, their Figures

619 11 and 12), but with occasional intervals when the chemocline rose to cover the shallow shelf.  
620 Deposition of several Mn-carbonate layers (up to 4; Gnoevaya et al., 1982) during Early Oligocene  
621 suggests for intermittent euxinic conditions, like those in the modern Baltic Sea deeps (Lenz et al.,  
622 2015).

623 This model is also supported by the Mo content of the Mn-ore layer (Table 3). Molybdenum  
624 concentrations of this layer are generally below 10 ppm (except for sample OBR-5-1262; Table  
625 3). Studies on modern euxinic basins (Scott and Lyons, 2012) showed that Mo concentrations  
626 exceeding 100 ppm in sediments are a strong indicator for the presence of H<sub>2</sub>S in the water column  
627 overlying the sediment. It has also been demonstrated that Mo/Al ratio of the sediments increases  
628 in euxinic conditions (Algeo and Lyons, 2006). Low Mo content of the Mn-ore layer yields Mo/Al  
629 ratios (not shown) below those typical for the euxinic Black Sea sediments (Eckert et al., 2013).  
630 All this is in line with the hypothesis that the Mn-ore layer formed above the deep euxinic waters.

631 To understand the distribution of trace elements in the Ruslar Formation, it is necessary to  
632 consider processes in the suboxic seawater layer and in the underlying anoxic (euxinic) layer.  
633 Again, using the modern Black Sea as an analog of the Early Oligocene Western Black Sea,  
634 particulates in the euxinic (sulfidic) deep seawater should be enriched in elements that form highly  
635 insoluble sulfide minerals, whereas the overlying suboxic seawater should be enriched in those  
636 elements that bind strongly to Mn-oxides. From the data reported by Lewis and Landing (1991;  
637 1992), particulate Fe, Pb, and Zn are strongly enriched in deep Black Sea anoxic seawater.  
638 Particulate Mn, Cu, and Ni have highest concentrations in the suboxic layer. Yigitheran et al.  
639 (2011) also reported a correlation of Fe and Pb in the particulate fraction of the deep Black Sea  
640 anoxic seawater. Zn did not correlate well to Fe, possibly owing to anthropogenic contributions,  
641 but the authors attributed Zn removal to the formation of sulfides. Particulate Co was strongly

642 associated with Mn, as were U and V. Particulate Cr, Mo, and Ni were strongly correlated to each  
643 other, but not to Mn or Fe, and they tended to have irregular vertical distributions. Cu had no  
644 associations (Yigitheran et al., 2011). In summary, the euxinic deep seawater has particulates rich  
645 in Fe, Pb, and Zn, whereas the suboxic shallow waters have high particulate Mn, Co, U, and V  
646 concentrations. The elements Cr, Cu, Mo, and Ni can be with either seawater layer.

647 For the Ruslar Formation, using leachate compositions as representative of the non-detrital  
648 component (Table 4), Mn-rich samples show a strong enrichment in Mg and V and moderate  
649 enrichments in Ba, Co, Ni, and P compared to low-Mn samples, but are depleted in Ca, Fe, Pb,  
650 and Zn. This pattern is consistent with deposition in the suboxic zone of an euxinic basin like the  
651 modern Black Sea.

652 Strata deposited under anoxic to euxinic conditions are reported from Lower Oligocene  
653 sections in various parts of Parathethys, for example the eastern Carpathians (Sachsenhofer et al.,  
654 2015), Georgia (Pupp et al., 2018), Azerbaijan (Bechtel et al., 2014). We can hypothesize that the  
655 euxinia in the deeper basin sequestered a substantial amount of the dissolved metals that bind to  
656 S, most importantly Fe. Manganese does not make easily an insoluble sulfide, which allowed the  
657 separation of  $Mn^{2+}$  dissolved in the water column from  $Fe^{2+}$ , which was incorporated in bottom  
658 sediments as Fe-sulfides. The Early Oligocene transgression over the Western Black Sea shelf  
659 promoted the deposition of Mn-oxides, which in turn absorbed Ba, Ce, Co, Cu, Ni, and V. During  
660 early diagenesis, these Mn-oxides were converted to the Mn-carbonate layers and would have  
661 retained most of this array of trace elements (e.g., Johnson et al., 2016). However, as shown by the  
662 C isotope patterns described in sub-section 4.4.1, this scenario of diagenetic formation of  
663 carbonates only applies to a portion of the Mn-ore beds. Other portions formed authigenically by  
664 direct precipitation from the seawater of the basin as carbonates, and thus would have been less

665 prone to incorporation of those elements that bind to Mn-oxides. In modern Mn-nodules, the most  
666 strongly enriched trace elements are  $\text{Co} > \text{Ni} > \text{Mn} > \text{Cu}$  (Li 2000). These elements, plus Cr and V,  
667 are enriched in the diagenetically formed Mn-carbonate layers compared to the authigenic ones,  
668 which provides support for our model of Mn-carbonate formation by dual pathways.

669

#### 670 *5.4. Sr, Nd, and Pb isotope constraints*

671

672 McArthur and Howarth (2004) report the following Oligocene seawater  $^{87}\text{Sr}/^{86}\text{Sr}$  values  
673 (error  $\pm 0.00002$ ): 0.707915 at 32 Ma, 0.70795 at 31 Ma, and 0.70798 at 30 Ma. The average  
674  $^{87}\text{Sr}/^{86}\text{Sr}$  observed in our samples leachates is 0.707966 ( $\pm 0.00012$ ), and excluding one outlier  
675 (leachate OBR-5-1264 with  $^{87}\text{Sr}/^{86}\text{Sr}=0.70837$ ), the average  $^{87}\text{Sr}/^{86}\text{Sr}$  is 0.707941 ( $\pm 0.00006$ ).  
676 Both average leachate values (with and without the outlier) are indistinguishable from the  
677 Oligocene seawater at 31 Ma, suggesting that all of Sr in the 2M HCl leachable fraction was most  
678 likely derived from seawater. The slightly elevated values observed in the OBR-5-1264 sample  
679 are likely due to minor incorporation of Sr from the residual, detrital fraction during the 2M HCl  
680 leaching. In contrast to the leachates, the highly radiogenic Sr observed in the residues (presumably  
681 representative of the terrigenous input) indicates input from continental source.

682 Peucker-Ehrenbrink et al. (2010) reported  $\epsilon\text{Nd}$  of about -7.9 for modern Aegean Sea, which  
683 is the source for the underflow entering through the Bosphorus in Black Sea. Lericolais et al. (2012)  
684 reported slightly more negative  $\epsilon\text{Nd}$ , from -8.0 to -9.0, for Danube River-derived sediments in the  
685 western Black Sea. Nd isotopes in the leachates and bulk samples overall show less negative values  
686 when compared to modern day input from Danube and/or Bosphorus. However, the less negative  
687 values observed in our leachates and bulk samples overlap with the expected values for

688 Atlantic/Tethys seawater at 31 Ma. The leachates showing lower  $\epsilon\text{Nd}$  compared to Atlantic/Tethys  
689 (Fig. 11) can be explained either with contribution of Nd from paleo-Danube River or Nd  
690 contribution from the residues. Either way, the more negative  $\epsilon\text{Nd}$  values indicate contribution  
691 from continental source. As can be seen on Figure 11 the leachates and bulk samples extend  
692 towards the more negative values represented by the residues. This suggests that Nd (and  
693 presumably the REE) is controlled by boundary exchange processes (mixing between seawater  
694 and regionally derived detrital input), given the proximity of the sediment deposition area to nearby  
695 landmasses.

696 Based on the regional geological setting, the most likely regional sources for the detrital  
697 materials to the Oligocene Western Black Sea was the eastern part of the Moesian Platform (to the  
698 west and north-west), the Eastern Balkanides (including eastern Stara Planina and eastern  
699 Srednogorie to the west), Strandzha Mountains and Eastern Rhodope Mountains to the south-west.  
700 Erosion of Cretaceous-age volcanic cover rocks from the Srednogorie Arc would have supplied  
701 detrital material with low  $^{87}\text{Sr}/^{86}\text{Sr}$  ( $\sim 0.7045$ ; Georgiev et al., 2009). The pre-Mesozoic basement  
702 of the Srednogorie Arc, however, would have yielded more radiogenic values,  $\sim 0.7076$ - $0.7081$   
703 (Georgiev et al., 2009). Detrital material from the Eastern Rhodope Mountains would likely have  
704 been blocked from reaching the studied part of the Oligocene Western Black Sea by the  
705 Srednogorie Arc, but explosive volcanism could have supplied the tephra component. There are  
706 several contemporaneous volcanic centers, but most show either less-radiogenic Sr ( $0.7073$ -  
707  $0.7078$ ), or much higher  $\epsilon\text{Nd}$  ( $-2.8$  to  $-3.8$ ) (Ivanova et al., 2002; Kirchenbau et al., 2012) to explain  
708 the trend observed in Sr-Nd isotopes of our samples. Only Mesta volcanics, which contain acidic  
709 extrusives with a large component of assimilated crust, can be a possible source as Marchev et al.  
710 (2014) reported initial  $^{87}\text{Sr}/^{86}\text{Sr}$  in the range of  $0.71080$ - $0.71521$  and initial  $\epsilon\text{Nd}$  of  $-6.1$  to  $-8.1$ .

711 However, even the Sr-Nd isotopic composition of the Mesta volcanics does not extend to the  
712 observed high  $^{87}\text{Sr}/^{86}\text{Sr}$  ratio (as high as 0.72038) and low  $\epsilon\text{Nd}$  (as low as -12.1) in the residues,  
713 representing the detrital input to the studied area. Therefore, based on the observed data for the  
714 sample residues we can rule out volcanoclastic input from the Srednogorie and/or Eastern Rhodope  
715 Mountains as a major contributor of the detrital component in the studied area. The high  $^{87}\text{Sr}/^{86}\text{Sr}$   
716 and low  $\epsilon\text{Nd}$  observed in the sample residues point to an older, non-arc related source for detrital  
717 component, possibly lithologic units in Stara Planina and/or Moesian Platform.

718 Pb isotopes of the studied samples show a wide range of compositions with no particular  
719 relationships observed between leachates and residues (Fig. 12). Overall, the Pb isotope data plot  
720 above the mantle evolution line, indicating that Pb was sourced from rocks with continental crust  
721 affinity. The overall linear spread in the Pb isotope data can be interpreted as Pb derivation from  
722 two sources. The most plausible sediment sources in the region are the Mesozoic Srednogorie Arc  
723 and the orogenic belt of Stara Planina, located between the arc terranes and the Moesian Platform.  
724 As can be seen on Figure 12, the available data from Srednogorie Arc can explain some of the less  
725 radiogenic Pb isotope values in the Obrochishte samples. In particular, 3 out of the 4 residues plot  
726 in Srednogorie field close to Vitosha Mountain, a volcano-magmatic complex related to the  
727 Mesozoic subduction. In contrast, Stara Planina detritus shows more radiogenic Pb isotopes, close  
728 to the bulk and a number of leachates (Fig. 12). It is highly unlikely that the 3 samples available  
729 in the literature from Stara Planina represent the full spread of Pb isotope values in the orogenic  
730 belt. In addition, it is possible that some of the radiogenic Pb isotopes observed in Obrochishte  
731 were derived from suspended sediments carried by proto-Danube River. Overall, the Pb isotopes  
732 in the Obrochishte samples indicate continental source for the sediments, consistent with the  
733 observed Sr-Nd isotopes in the residues.

734

735 *5.5. Source of Fe to the Mn-ore layer: Fe isotope constraints*

736

737 Our data argue for Mn-ore deposition at suboxic conditions in a redox-stratified marine basin  
738 representative of the Oligocene Western Black Sea. Studies on the Fe cycle in a modern redox-  
739 stratified marine basin (e.g., Black Sea) showed that  $Fe_{solid}$  from the oxic shelf is eventually  
740 exported to the deep anoxic basin via a benthic shuttle mechanism (Severmann et al., 2008, 2010).  
741 It was demonstrated that reduction of the sedimentary Fe deposited at the oxic shelf fractionates  
742 Fe isotopes and produces an isotopically light Fe flux to the deep basin (Severmann et al., 2010;  
743 Chever et al., 2015). Whereas  $\delta^{56/54}Fe$  of the oxic shelf sediments (0.07‰) is close to that of the  
744 weathering input (0‰; Dauphas et al., 2017),  $\delta^{56/54}Fe$  of the anoxic-euxinic sediments is typically  
745 negative, reflecting the value of the Fe shuttle ( $\delta^{56/54}Fe = -1.2$  to  $-0.7$  ‰; Severmann et al., 2008;  
746 Rolison et al., 2018) and Fe isotope fractionation during diagenetic pyrite formation (Guilbaud et  
747 al., 2011).

748 Iron isotope composition of the investigated Mn-ore layer is slightly negative:  $\delta^{56/54}Fe_{bulk} =$   
749  $-0.05$ ‰ (average of 14 measurements; Table 5). Pisoliths from the Mn-ore layer have more  
750 negative Fe isotope composition, which is comparable to that of the modern Black Sea anoxic-  
751 euxinic sediments:  $\delta^{56/54}Fe_{pisolith} = -0.22$ ‰ (average of 6 measurements; Table 5),  $\delta^{56/54}Fe_{Black\ Sea}$   
752  $euxinic\ sediments} = -0.22$ ‰ (Severmann et al., 2008). These Fe isotope values imply: (i) significant Fe  
753 isotope fractionation during diagenesis, such as dissimilatory Fe reduction leading to isotopically  
754 lighter Fe in the sediment porewaters, which is then recorded in the pisoliths; (ii) a significant  
755 portion of total Fe in the Mn-ore layer has been supplied through a benthic shuttle mechanism  
756 (Severmann et al., 2008, 2010) from the shallow oxic shelf sediments.

757 Compared to the oxic shelf sediments of the modern Black Sea (taken as a prototype of the  
758 background oxic sediments of the Oligocene Western Black Sea) that have Fe/Al ratio ranging  
759 from 0.5 to 0.6 (Severmann et al., 2008), the studied Mn-ore layers display a large range of Fe/Al:  
760 from 0.14 (OBR-11-6.1P) to 2.49 (OBR-11-1.2). This suggests that Fe is depleted in some Mn-ore  
761 layers while being enriched in others. The large variation in the excess of Fe content is consistent  
762 with a variable efficiency of the Fe shuttle. The lack of relationships between  $\delta^{56/54}\text{Fe}_{\text{bulk}}$  and Fe/Al  
763 further suggests that Fe enrichment/depletion processes produced only a limited Fe isotope  
764 fractionation.

765 Because Mn oxidizes more slowly than Fe in seawater, and does not easily form insoluble  
766 sulfides in euxinic conditions, a geographic separation of Mn and Fe deposits is often observed in  
767 sedimentary Mn deposits. The lack of relationship between Fe/Mn ratio and  $\delta^{56/54}\text{Fe}$  is consistent  
768 with a strong decoupling between Fe and Mn enrichment processes, leading to important  
769 constraints on the depositional setting of Mn-ore layers. We propose that the limited enrichment  
770 of Fe in the Mn deposits result from the combined effect of (i) the efficient trapping of Fe in the  
771 deeper part of the basin under euxinic conditions, which is also consistent with limited enrichment  
772 in Mo in the deposits (see section 5.3.2.) and (ii) a deepening of the chemocline (suboxic/euxinic  
773 interface) below the shelf edge, leading to a decreased efficiency of the Fe shuttle (e.g., Eckert et  
774 al., 2013). Considering that Fe requires lower redox potential than Mn to be solubilized, the  
775 expansion of suboxic conditions on the shelf would further promote the input of Mn in the water  
776 column, which can then be incorporated in Mn deposits either through direct precipitation in the  
777 water column, or through co-precipitation of Mn oxides and organic matter and further diagenetic  
778 reactions [see below and Maynard (2014)].

779

780 *5.6. Mechanisms of Mn-carbonate deposition: C and O stable isotope constraints*

781

782 The studied bulk samples from the Mn-ore bed are mostly composed of Mn-carbonates  
783 (Table 1). Hence, the C and O isotope composition of these samples (Table 5) reflects the C and  
784 O isotope composition of the Mn-carbonates, the major ore component.

785 C-O-isotope data distribution along two distinct trends (Fig. 9A), suggests two different  
786 mechanisms of Mn-carbonate precipitation at the studied region. All samples from the southern  
787 part (south of Obrochishte mine, sites ##6, 7, 8, 9, 10; Fig. 1B) as well as some samples from the  
788 north-eastern part of the Ruslar Formation (sites ##1, 2, 3; pisoliths from the lower part of the Mn-  
789 ore bed at site #11; Fig. 1B) lie along the mixing line between the modern Danube River water and  
790 Oligocene seawater (Fig. 9A). This suggests that C and O in the Mn-carbonates of the ore bed  
791 derived from two distinct sources: fresh water and seawater. Oligocene seawater is a reasonable  
792 source of C and O in carbonates deposited in the Oligocene marine basin. Questionable remains  
793 the fresh water source of C and O in Mn-carbonate deposits, which are interpreted to be submarine  
794 based on lithostratigraphic evidence (Aleksiev, 1960a; Stoyanov, 1963). The only possible  
795 submarine source of fresh water at continental margins is the submarine groundwater discharge  
796 (SGD) (Moore, 2010; Santos et al., 2012). SGD comprises terrestrial fresh groundwater mixed  
797 with seawater that has infiltrated coastal aquifers, and flows from the seafloor to the coastal ocean  
798 (Moore, 2010). It has recently been recognized as a global phenomenon (and also widespread in  
799 the Black Sea; Schubert et al., 2017), which is an important source of fresh water and dissolved  
800 elements to the ocean, comparable to the riverine input (Moore, 2010). This water flux contains  
801 high concentrations of dissolved inorganic carbon (DIC), Fe, and Mn (Windom et al., 2006;  
802 Szymczycha and Pempkowiak, 2016). Thus, the precipitation of Mn-carbonates, which plot along

803 the mixing line between the fresh water and Oligocene seawater C-O-isotope composition (Fig.  
804 9A), is explained by SGD at the Oligocene Western Black Sea shelf. According to the  
805 paleogeographical reconstructions (e.g., Nikishin et al., 2015), the area of deposition of the Ruslar  
806 Formation was a wide shelf (Western Black Sea basin) bounded by the Balkan High to the south  
807 and Moesian High to the north-west during the Oligocene. The elevated landmasses could have  
808 provided a sufficient hydraulic head difference to overcome the pressure from seawater and allow  
809 groundwater to discharge onto the seafloor.

810 The proportions of two end-members of the SGD, fresh water and seawater, vary spatially  
811 and temporally due to a number of factors (Moore, 2010; Santos et al., 2012). Thus, the spread of  
812 the data points between both end-members (Fig. 9A) reflects the different contribution of fresh  
813 water and seawater to the C and O isotope composition of the Mn-carbonates. Mn-carbonates in  
814 the southern part of the Ruslar Formation (associated with ~400 m thick clays and sandstones; Fig.  
815 1B) formed at higher proportion of fresh SGD than the Mn-carbonates from the north-eastern part  
816 of the Ruslar Formation (associated with ~100-250 m thick clays, sandstones, and marls; Fig. 1B)  
817 (Fig. 9A).

818 Mn-carbonates that show precipitation at submarine groundwater discharge with varying  
819 contribution of its two components (fresh water and seawater, Fig. 9A) cluster along a trend at the  
820  $\delta^{13}\text{C} - \text{MnO}$  space (Fig. 9B) suggesting precipitation by direct reaction with  $\text{HCO}_3^-$ . The second  
821 group of Mn-carbonate samples comprising those from the upper part of Mn-ore bed at site #11  
822 and lower part of Mn-ore bed at site #5 form distinct arrays at both C-O-isotope diagrams (Fig.  
823 9A, B), suggests they formed by oxidation of organic matter within the sediment. Thus, the Mn-  
824 carbonates from the studied Mn-ore bed likely formed via two different mechanisms: (1)  
825 precipitation through reaction of dissolved inorganic species (e.g.,  $\text{Mn}^{2+}$  and  $\text{HCO}_3^-$ ), and (2)

826 diagenetic precipitation mediated by oxidation of organic matter. Whereas the second mechanism  
827 operated within the sediment, the first may have worked either in the water column or in the near-  
828 seafloor sediment pore space.

829 The average range for C isotopic compositions in sediment-hosted Mn-carbonate ores is -1  
830 to -16‰ (based on a survey of 17 deposits with isotopic data compiled at  
831 [http://www.sedimentaryores.net/Index\\_Mn.html](http://www.sedimentaryores.net/Index_Mn.html)). Some samples from the Obrochishte deposit  
832 have  $\delta^{13}\text{C}$  values outside this range, both positive and negative (Table 5).  $\delta^{13}\text{C}$  values in the range  
833 0 to +5‰ are reported for 6 of the 17 deposits listed in the database cited above, so this is a common  
834 situation. Almost all are associated with high Ca/Mn ratio, as are most of the positive values for  
835 Obrochishte samples. Such values could result from slight evaporation of seawater, or be from  
836 residual  $\text{CO}_2$  left from  $\text{CH}_4$  fermentation during early diagenesis, with the  $\text{CH}_4$  escaping. Two  
837 samples from the Obrochishte deposit have very light  $\delta^{13}\text{C}$  values (Table 5). Similar values have  
838 been reported for 3 of the 17 deposits in the database, so this situation is not common, but also not  
839 unusual. These values could result from  $\text{CO}_2$  totally sourced from oxidation of marine organic  
840 matter or, more likely, from oxidation of  $\text{CH}_4$ .

841 The long-standing debate on the source of Mn to the Oligocene Western Black Sea and,  
842 eventually, to the deposited Mn-carbonates was recently summarized by Vangelova et al. (2005).  
843 We will just underline the earlier observations of Aleksiev (1959) on the lithology and stratigraphy  
844 of the Oligocene Series in NE Bulgaria and his interpretations about the Mn source to the  
845 Oligocene Black Sea basin. He described three (in some sections four) sets of rhyolite tuff layers  
846 across the Oligocene Series in NE Bulgaria and noticed that the Mn ore layers either immediately  
847 overlie the tuff layers, or are intercalated in them (Aleksiev, 1959; Huff et al., 2014). Based on  
848 lithology, mineralogy, and geochemistry studies, Aleksiev (1959) assumed that the tuff layers were

849 a result of submarine volcanic activity within the Oligocene Western Black Sea. He suggested that  
850 post-volcanic submarine hydrothermal activity was the source of Mn to the Mn-ore deposits  
851 around the modern Black Sea. Later work has not added anything meaningful to this problem  
852 except for far-going “exotic” hypotheses about the Mn source and origin of the Mn-ore bed  
853 [summarized in Vangelova et al. (2005)].

854 Based on the interpretation of our C and O isotope data we suggest that in addition to or  
855 instead of the inferred submarine hydrothermal source of Mn (Aleksiev, 1959), the submarine  
856 groundwater discharge may be another possible Mn source in the Oligocene Western Black Sea.  
857 Studies on the redox conditions in the SGD show that they vary from oxic to anoxic depending on  
858 the proportions of fresh water and recirculated seawater, and local conditions at the seafloor  
859 (Moore, 2010; Santos et al., 2012). Transportation of Mn in dissolved state within the SGD and its  
860 input into the marine basin generally requires suboxic to anoxic conditions. Further, the  
861 precipitation of Mn in solid phase and deposition at the seafloor requires either high Eh ( $E_h > 530$   
862 mV at pH=7 and  $T=25^\circ\text{C}$ , and preliminary precipitation as Mn-oxyhydroxides), or high alkalinity,  
863 or very high dissolved Mn concentrations (direct precipitation as Mn-carbonates).

864 We may speculate about the mechanisms of Mn-carbonate precipitation at the Oligocene  
865 Western Black Sea floor. The REE evidence shows that the eventual Mn-carbonates had formed  
866 at suboxic seawater conditions (see 5.2). Suboxic conditions can exist throughout large volumes  
867 of seawater column: suboxic and anoxic marine basins, and oxygen-minimum zone at continental  
868 margins. Although we are not aware of existence of highly alkaline conditions in large seawater  
869 masses in the modern ocean, we cannot completely rule out the temporary establishment of  
870 alkaline conditions in isolated and semi-isolated marine basins. Hence, direct precipitation of Mn-  
871 carbonates in the seawater column seems likely when a high flux of dissolved Mn into a suboxic

872 seawater layer is combined with increased alkalinity. In modern times this process has been  
873 reported only in lakes (Havig et al., 2018; Herndon et al., 2018).

874        Could this high Mn flux have been caused by purely sedimentary processes? It is tempting  
875 to view the diagenetic Mn as forming from Mn-oxide particles settled in the suboxic water layer,  
876 where the highest particulate Mn occurs (e.g., Lewis and Landing, 1991), whereas the authigenic  
877 Mn is formed in the underlying anoxic euxinic layer, where the highest dissolved Mn is found  
878 (Lewis and Landing, 1991). If this was the case, we would expect to see higher S in the authigenic  
879 Mn (deeper water, below the H<sub>2</sub>S interface). Furthermore, there should be a weak Ce anomaly in  
880 the authigenic Mn precipitates, but a large one in the diagenetic Mn phases. Our results show that  
881 the reverse is true for both parameters: S<sub>tot</sub> averages 0.21% in the authigenic beds compared with  
882 0.54% in the diagenetic beds. Ce/Ce\* of the leachate is 0.75 in the authigenic beds, 0.81 in the  
883 diagenetic. (We excluded the fresh water-influenced samples from these calculations). Thus, the  
884 authigenic beds that dominate the ore body have geochemical properties inconsistent with a  
885 deposition in anoxic euxinic deep waters. The only reasonable possibility that remains is  
886 precipitation of authigenic Mn-carbonates in the suboxic water column. To have this process  
887 working and producing ore-grade Mn deposit there should be high dissolved Mn flux and alkalinity  
888 in the suboxic zone.

889        The group of samples that were strongly affected by SGD (with the highest fresh water  
890 contribution), based on C-O-isotopes, have sub-economic concentrations of Mn in all cases (Fig.  
891 9). Hence, it would appear that, at least for the Obrochishte case, an inferred Mn flux from SGD  
892 alone was not sufficient to produce a major Mn deposit. Considering the high-Mn samples, all  
893 have O-isotopes consistent with precipitation from seawater with a minor fresh water component  
894 (presumably SGD) (Fig. 9A). Those, whose C-isotopes indicate diagenetic conversion of Mn-

895 oxide to Mn-carbonate, have trace element signatures suggestive of primary deposition as Mn-  
896 oxide. By contrast, the samples whose C-isotopes indicate direct precipitation in seawater column  
897 are enriched in Ba, Pb, and Zn, elements that are mobilized and released from the sediment during  
898 organic matter-driven diagenesis (Gobeil and Silverberg, 1989; Kerner and Wallmann, 1992;  
899 McManus et al., 1994; Hendy, 2010).

900

### 901 *5.7. Model of formation of the Obrochishte Mn deposit*

902

903 There is virtually no direct evidence for hydrothermal Mn input in the Oligocene Western  
904 Black Sea other than the tuff layers associated with the deposit. Bulk chemistry of the Obrochishte  
905 Mn-ores is the same as background sediment, except for Mn and C. Oxygen isotopes do not suggest  
906 a hydrothermal component. Nd, Pb, and Sr isotopes reflect seawater, or local clastics. Textures  
907 and sequence stratigraphy seem more or less like any other Phanerozoic deposit. But the mass of  
908 Mn contained in this narrow time interval is at least  $600 \times 10^6$  tons (Maynard, 2010), more than all  
909 of the rest of the Phanerozoic deposits combined, and precipitated in only about 500,000 years.  
910 This truly remarkable geochemical event suggests some special circumstances at this time interval.  
911 The Earth climate was coming off an exceptionally high temperature and high  $P_{CO_2}$  at the Early  
912 Eocene Climatic Optimum (EECO) (50-52 Ma, Zachos et al., 2001). This event was followed by  
913 the initiation of glaciation in Antarctica at the end of Eocene and beginning of Oligocene,  
914 accompanied by one of the sharpest drops in temperature and sea level in the Phanerozoic. It is  
915 likely that the intense chemical weathering during the Eocene produced a thick residuum enriched  
916 in kaolinite and Fe- and Mn-oxyhydroxides on the continents and these processes peaked  $\sim 35$  Ma,  
917 during the Late Eocene (see for example Retallack, 2010) (Fig. 13 A). The Early Oligocene sea

918 level fall caused rapid erosion of these lateritic deposits, while at the same time producing  
919 restricted basins and anoxic euxinic conditions (Fig. 13 B). The hypothesis of erosion of the  
920 Eocene laterites is supported by a recent study (Dekoninck et al., 2019) of the weathering of  
921 primary Mn-rich sedimentary rocks (Ordovician) and formation of supergene Mn-deposits (Late  
922 Oligocene – Late Neogene) in the Central and Western Europe. It concluded that the old  
923 weathering series/systems (e.g., Eocene) must have been removed (at least partly) from the  
924 geological record. The erosion products that found their way to the open ocean remained as stable  
925 detrital sediments. Fe- and Mn-oxyhydroxides deposited into anoxic euxinic basins (like the  
926 Western Black Sea) were dissolved and released Fe and Mn in the seawater. The Fe was  
927 reprecipitated as Fe-sulfides while the Mn accumulated as dissolved  $Mn^{2+}$  in the anoxic euxinic  
928 water column (Fig. 13 B). Suboxic water layer formed as a transition zone between the deep anoxic  
929 and surface oxic waters. Steep concentration gradient of dissolved Mn across the suboxic-anoxic  
930 interface caused Mn diffusion towards the suboxic layer where it oxidized and sank back into the  
931 anoxic waters (Fig. 13 C). The amount of oxidized  $Mn^{2+}$  in the suboxic layer was controlled by  
932 the available dissolved  $O_2$ . Due to the general depletion of  $O_2$  in this layer part of the dissolved  
933 Mn supplied from below remained as  $Mn^{2+}$ . The weathering-related Mn flux to the Western Black  
934 Sea was supplemented by SGD Mn flux. Volcaniclastic layers below and among the Mn-ore layers  
935 (Aleksiev, 1959) imply that ash fall dissolution in seawater (e.g., Frogner et al., 2001; Randazzo  
936 et al., 2009; Censi et al., 2010) may have additionally supplied Mn in the basin before and during  
937 Mn-ore deposition (Fig. 13 C). Alteration of this ash would also have increased alkalinity and  
938 raised the dissolved silica level in sediment pore waters (e.g., Lyons et al., 2000).

939 Was the dissolved Mn stored in the Oligocene Black Sea enough to produce the Mn ores  
940 deposited there? The dissolved Mn inventory of the modern Black Sea is about  $220 \times 10^6$  metric

941 tons ( $5.03 \times 10^5$  km<sup>3</sup> seawater below chemocline with 8  $\mu$ M dissolved Mn). This amount compares  
942 to  $550 \times 10^6$  tons of Mn in high-grade ores in all Oligocene deposits combined (Maynard, 2014).  
943 Assuming an equal mass for low-grade ore, the total resource is about  $1000 \times 10^6$  tons of Mn. Even  
944 if all of the dissolved Mn in the modern Black Sea could be precipitated at once, it would still fall  
945 short by a factor of five. How often is this mass of Mn renewed? In the fluxes of Mn to the Black  
946 Sea, particulate-borne Mn in river suspended solids dominates substantially over dissolved  
947 transport, and the Danube dominates all other river sources. Annual suspended load for the Danube  
948 before dam construction was about  $47 \times 10^6$  tons/year (Oaie et al., 2005) with 1380 mg/kg Mn  
949 (Yigiterhan and Murray, 2008). Deep-water sediments contain approximately 620 mg/kg of Mn  
950 (Brumsack, 1989) so the net contribution of Mn from the Danube flux is 760 mg/kg or  $3.6 \times 10^4$   
951 tons/year of Mn. Using the same concentration values for other rivers entering the Black Sea would  
952 add another  $0.6 \times 10^4$  tons, based on suspended loads from Mikhailova (2009). Total river sources  
953 would then be  $4.2 \times 10^4$  tons/year. Some of this river flux is lost to the Mediterranean Sea via the  
954 net outflow through the Bosphorus Strait, but the amount is very small compared to the river flux.  
955 At  $4.2 \times 10^4$  tons/year it would take only 24000 years to supply all of the Mn in the Oligocene  
956 economic deposits. Even if the efficiency were only 10%, there would be adequate supply to  
957 account for the existing deposits. But there are no large accumulations of Mn forming in the Black  
958 Sea today, suggesting that there must be additional factors beyond the existence of a large euxinic  
959 basin responsible for the formation of the ore bodies.

960 Eocene-Oligocene glaciation had led to an increased ocean alkalinity on a global scale  
961 (Coxall et al., 2005). Ephemeral glacial ice (Greenland) and sea ice (Arctic) formed in the Northern  
962 Hemisphere (Tripathi and Darby, 2018). We can assume that there may have been at least  
963 permafrost in northern Europe (the drainage area of the big rivers emptying in Oligocene Black

964 Sea). This would mean that the groundwater table had lowered in the northern Europe during the  
965 cooling event at Eocene-Oligocene boundary.

966 Early Oligocene warming and sea level rise must have led to a marine transgression over the  
967 Western Black Sea shelf. The suboxic layer of vertically stratified seawater would have impinged  
968 on the shelf. From what we know from the modern Black Sea, this layer contained both suspended  
969  $\text{MnO}_2$  and dissolved  $\text{Mn}^{2+}$ . Settled  $\text{MnO}_2$  particles had diagenetically transformed into  $\text{MnCO}_3$ :  
970  $\text{MnO}_2$  dissolution,  $\text{Mn}^{4+}$  reduction to  $\text{Mn}^{2+}$ , and  $\text{Mn}^{2+}$  re-precipitation as  $\text{MnCO}_3$  (Fig. 13 C).

971 Early Oligocene warming had caused permafrost/glacier melting in northern Europe, which  
972 would have increased the groundwater volume and led to groundwater table rise (e.g., Liljedahl et  
973 al., 2017). As a result, the SGD flux should have increased and this would bring  $\text{HCO}_3^-$  and  
974 alkalinity directly in the Western Black Sea shelf. Eocene rocks (potential groundwater aquifer  
975 during Early Oligocene) that underlie Obrochishte Mn-layer are mostly carbonates. Hence, high  
976  $\text{HCO}_3^-$  and alkalinity supply (through SGD and as a result of previous glaciation) to the shelf seems  
977 possible.

978 Thus, dissolved  $\text{Mn}^{2+}$  precipitation as Mn-carbonates in suboxic water layer overlaps with  
979 diagenetic Mn-carbonate precipitation from  $\text{MnO}_2$  precursor in the sediment (Fig. 13 C). Dissolved  
980 Mn precipitation will draw down its content in the suboxic layer and this will cause pumping of  
981 dissolved Mn from the deeper anoxic Mn store due to sharp concentration gradient and molecular  
982 diffusion, eddy diffusion and turbulent mixing (e.g., Podymov et al., 2017). This pumping  
983 mechanism will supply high dissolved Mn flux to the shelf where it will meet high alkalinity flux  
984 and this will result in authigenic precipitation of Mn-carbonates in the seawater column.

985

986 *5.8. Comparison of Obrochishte Mn-deposit to other Oligocene Mn-deposits around the Black Sea*

987

988         Although the Oligocene Mn-deposits around the Black Sea have been studied for many  
989 years, data is still spotty and incomplete, except for major elements (Table 6). Isotopic data for  
990 radiogenic isotopes are not available that we know of, but some information on stable isotopes of  
991 C and O has been published [see Kuleshov (2017) for a summary]. However, there is a lack of  
992 systematic data where major, trace element, and isotopic data were acquired on the same samples.  
993 There is only enough systematic data for us to make comparisons for C and O isotopes for three  
994 deposits: Binkiliç (Turkey), Chiatura (Georgia), and Mangyshlak (Kazakhstan). The detailed  
995 datasets for each of these deposits are available at  
996 <http://www.sedimentaryores.net/Manganese/Black%20Sea%20index.html>.

997         Binkiliç Mn-deposit shows a pattern of stable isotopes with a cluster tightly grouped around  
998  $-6.6\text{‰ } \delta^{13}\text{C}_{\text{VPDB}}$  and  $-7\text{‰ } \delta^{18}\text{O}_{\text{VPDB}}$  (Fig. 14 A). The C isotopes do not show a correlation with  
999 the amount of Mn (Fig. 14 B), which is not consistent with the formation of  $\text{MnCO}_3$  by reaction  
1000 of MnO or  $\text{MnO}_2$  with organic matter during early diagenesis. Instead, direct precipitation in the  
1001 water column is more likely. Ozturk and Frakes (1995) interpreted the uniformly light oxygen  
1002 isotope values as indicating an important role of meteoric water in ore genesis. We speculate that  
1003 Binkiliç Mn-deposit could have formed in a large freshwater lake.

1004         The Mn-deposits at Chiatura have isotopic values that are strongly overprinted by a late  
1005 diagenetic event, one that added considerable Ca and some Mn from a fluid with  $\delta^{13}\text{C}$  and  $\delta^{18}\text{O}$   
1006 close to  $0\text{‰}$  (Fig. 14 C,D) [see Kuleshov (2017) for a discussion].

1007         Of the three deposits for which we have sufficient data, Mangyshlak is closest in isotope  
1008 behavior to Obrochishte. A plot of MnO content vs  $\delta^{13}\text{C}$  (Fig. 14 E) shows the same two  
1009 populations as at Obrochishte: (1) has constant  $\delta^{13}\text{C}$  at all MnO contents, indicating direct

1010 precipitation of  $\text{MnCO}_3$  in the water column (This data population has low  $R^2$  (0.30) and high  $p$   
1011 (0.17), which suggests there has to be some significant additional factor at work for these samples:  
1012 likely an irregular component of diagenetic addition of lighter  $\delta^{13}\text{C}$ .), and (2) has a negative  
1013 covariance of MnO content and  $\delta^{13}\text{C}$ , indicating production of  $\text{MnCO}_3$  via reaction of  $\text{MnO}_2$  with  
1014 organic matter during early diagenesis (This data population has  $R^2$  of 0.82 and a  $p$  value of 0.01  
1015 for the regression, which suggests that this group of samples is well-explained by our model.). A  
1016 plot of  $\delta^{18}\text{O}$  vs  $\delta^{13}\text{C}$  (Fig. 14 F) shows a linear trend to sharply lighter  $\delta^{18}\text{O}$  at nearly constant  $\delta^{13}\text{C}$ ,  
1017 suggestive of groundwater-seawater mixing, as at Obrochishte, but this time, only calcite is  
1018 involved.

1019

1020

## 1021 6. Conclusions

1022

1023 Isotope geochemistry of the Obrochishte Mn-deposit revealed surprising complexity in the  
1024 details of Mn precipitation. The data indicate involvement of normal seawater and meteoric water  
1025 (presumably from submarine groundwater discharges onto the seafloor). There was authigenic as  
1026 well as diagenetic precipitation of the main ore minerals, Mn-carbonates. We present a general  
1027 model of the formation of the Obrochishte Mn-deposit (Fig. 13) that we believe is applicable to  
1028 the series of deposits of this age that encircle the present-day Black Sea and explains the peculiar  
1029 concentration of Mn ores at this time and place. Intense weathering during the Eocene weathering  
1030 phase produced thick lateritic soils enriched in Fe and Mn. The dramatic sea level fall at the  
1031 Eocene-Oligocene boundary caused flushing of the lateritic residue into marginal basins while at  
1032 the same time led to isolation of these basins from the global ocean which fostered anoxic

1033 conditions. The sea level fall also produced a much greater head difference between groundwater  
1034 recharge areas and the continental shelf, which intensified submarine discharge of Mn-bearing  
1035 groundwater. Continent-derived Fe and Mn were transferred to a redox-stratified Western Black  
1036 Sea basin, similar to the modern Black Sea. Most of the Fe was sequestered in deep anoxic-euxinic  
1037 water as sulfides, while Mn accumulated in the suboxic water layer. Transgression of this Mn-rich  
1038 seawater onto the shallow shelf, and some Mn contribution from submarine ground water  
1039 discharge, led to the formation of the Oligocene Mn deposits. This unique sequence of events and  
1040 the configuration of the continental masses around the depositional basin produced the exceptional  
1041 accumulations of Mn around the Black Sea.

1042

1043

#### 1044 **Acknowledgements**

1045

1046 V.M. Dekov appreciates the support from the LabexMER (IUEM, UBO, Brest, France) Axis 3  
1047 initiative “Geobiological interactions in extreme environments” through grant NODESIS. Many  
1048 thanks go to Mr. Plamen Neychev (former geologist at Obrochishte mine) who provided the  
1049 samples from the Obrochishte mine. The numerous suggestions and constructive comments by  
1050 Andrey Bekker and an anonymous reviewer improved the paper significantly and are highly  
1051 appreciated.

1052

1053

#### 1054 **References**

1055

- 1056 Aleksiev, B., 1959. Oligocene pyroclastic sedimentary rocks from Varna district. Reports of Geological Institute,  
1057 Bulgarian Academy of Sciences 7, 101-117 (in Bulgarian).
- 1058 Aleksiev, B., 1960a. Neotocite from the Oligocene Mn-ore bed in Varna district. Mineralogy Collection of the Lvov  
1059 Geological Society 14, 208-214.
- 1060 Aleksiev, B., 1960b. Sedimentare Manganerse des Oligozans bei Varna-Bulgarien. Freiburger Forschungshefte C 79.
- 1061 Aleksiev, B., Nacheva, L., 1966. Characteristic of manganese ore from Obrochishte deposit, Tolbuhin area. Annual  
1062 of Sofia University, Geology 61, 237-260 (in Bulgarian).
- 1063 Aleksiev, B., Nacheva, L., 1969. Substantial composition of manganese ore from Obrochishte deposit. Ore Product.  
1064 Metallurgy 7, 18-20 (in Bulgarian).
- 1065 Algeo, T.J., Lyons, T.W., 2006. Mo-total organic carbon covariation in modern anoxic marine environments:  
1066 Implications for analysis of paleoredox and paleohydrographic conditions. *Paleoceanography* 21, PA1016.
- 1067 Armstrong-McKay, D.I., Tyrrell, T., Wilson, P.A., 2016. Global carbon cycle perturbation across the Eocene-  
1068 Oligocene climate transition. *Paleoceanography* 31, 311-329.
- 1069 Asael, D., Tissot, F.L.H., Reinhard, C.T., Rouxel, O., Dauphas, N., Lyons, T.W., Ponzevera, E., Liorzou, C., Cheron,  
1070 S., 2013. Coupled molybdenum, iron and uranium stable isotopes as oceanic paleoredox proxies during the  
1071 Paleoproterozoic Shunga Event. *Chem. Geol.* 362, 193-210.
- 1072 Atanasova, S., Petrov, P., Yanakieva, D., Stanchev, H., 2009. Greigite from the manganese ore bed of Obrochishte  
1073 deposit, Dobrich district, NE Bulgaria – first data. V International Symposium “Mineral Diversity, Research  
1074 and Preservation”, 12-15 October 2009, Sofia, pp. 255-265.
- 1075 Basak, C., Martin, E.E., 2013. Antarctic weathering and carbonate compensation at the Eocene-Oligocene transition.  
1076 *Nature Geoscience* 6, 121-124.
- 1077 Bechtel, A., Muvsumova, U., Pross, J., Gratzer, R., Coric, S., Sachsenhofer, R., 2014. The Oligocene Maikop series  
1078 of Lahich (eastern Azerbaijan): Paleoenvironment and oil-source rock correlation. *Org. Geochem.* 71, 43-59.
- 1079 Berger, A., 1968. Geochimie und Lagerstättenkunde des Mangans. Clausthaler Hefte zur Lagerstatt und Geochemie  
1080 des Mineral Rohstoffe 7, 216 p.
- 1081 Berner, R.A., 1982. Burial of organic carbon and pyrite sulfur in the modern ocean: its geochemical and environmental  
1082 significance. *Am. J. Sci.* 282, 451-473.
- 1083 Beukes, N.J., Swindell, E.P.W., Wabo, H., 2016. Manganese deposits of Africa. *Episodes* 39, 285-317.

- 1084 Bogdanova, K., 1968. Structure of manganese ore bed in Obrochishte deposit. *Rev. Bulg. Geol. Soc.* 29, 13-26 (in  
1085 Bulgarian).
- 1086 Bonev, N., Dilek, Y., Hanchar, J.M., Bogdanov, K., Klain, L., 2012. Nd–Sr–Pb isotopic composition and mantle  
1087 sources of Triassic rift units in the Serbo-Macedonian and the western Rhodope massifs (Bulgaria–Greece).  
1088 *Geol. Mag.* 149, 146-152.
- 1089 Brumsack, H.J., 1989. Geochemistry of recent TOC-rich sediments from the Gulf of California and the Black Sea.  
1090 *Geol. Rundsch.* 78, 851-882.
- 1091 Censi, P., Randazzo, L.A., Zuddas, P., Saiano, F., Aricò, P., Andò, S., 2010. Trace element behaviour in seawater  
1092 during Etna's pyroclastic activity in 2001: Concurrent effects of nutrients and formation of alteration minerals.  
1093 *J. Volcanol. Geoth. Res.* 193, 106-116.
- 1094 Chever, F., Rouxel, O., Croot, P.L., Ponzevera, E., Wuttig, K., Auro, M., 2015. Total dissolvable and dissolved iron  
1095 isotopes in the water column of the Peru upwelling regime. *Geochim. Cosmochim. Acta* 162, 66-82.
- 1096 Coxall, H.K., Wilson, P.A., Pälike, H., Lear, C.H., Backman, J., 2005. Rapid stepwise onset of Antarctic glaciation  
1097 and deeper calcite compensation in the Pacific Ocean. *Nature* 433, 53-57.
- 1098 Dauphas, N., John, S., Rouxel, O., 2017. Iron isotope systematics. *Rev. Mineral. Geochem.* 82, 415-510.
- 1099 Dekoninck, A., Monié, P., Blockmans, S., Hatert, F., Rochez, G., Yans, J., 2019. Genesis and  $^{40}\text{Ar}/^{39}\text{Ar}$  dating of K-  
1100 Mn oxides from the Stavelot Massif (Ardenne, Belgium): Insights into Oligocene to Pliocene weathering  
1101 periods in Western Europe. *Ore Geol. Rev.* 115, 103191.
- 1102 Eckert, S., Brumsack, H.J., Severmann, S., Schnetger, B., Marz, C., Frollje, H., 2013. Establishment of euxinic  
1103 conditions in the Holocene Black Sea. *Geology* 41, 431-434.
- 1104 Friedman, I., O'Neil, J.R., 1977. Compilation of stable isotope fractionation factors of geochemical interest. In:  
1105 Fleischer, M. (Ed.), *Data of Geochemistry, Sixth Edition*. U.S. Geological Survey Professional Paper 440-KK.  
1106 U.S. Government Printing Office, Washington, p. 12.
- 1107 Frogner, P., Gíslason, S.R., Óskarsson, N., 2001. Fertilizing potential of volcanic ash in ocean surface water. *Geology*  
1108 29, 487-490.
- 1109 Galimov, E.M., Kodina, L.A., Zhiltsova, L.I., Tokarev, V.G., Vlasova, L.N., Bogacheva, M.P., Korobeinik, G.S.,  
1110 Vaisman, T.I., 2002. Organic carbon geochemistry in the north-western Black Sea–Danube River System.  
1111 *Estuar. Coast. Shelf. Sci.* 54, 631-641.

- 1112 Georgiev, N., Pleuger, J., Froitzheim, N., Sarov, S., Jahn-Awe, S., Nagel, T.J., 2010. Separate Eocene–Early  
1113 Oligocene and Miocene stages of extension and core complex formation in the Western Rhodopes, Mesta  
1114 Basin, and Pirin Mountains (Bulgaria). *Tectonophysics* 487, 59-84.
- 1115 Georgiev, S., Marchev, P., Heinrich, C.A., von Quadt, A., Peytcheva, I., Manetti, P., 2009. Origin of nepheline-  
1116 normative high-K ankaramites and the evolution of Eastern Srednogorie arc in SE Europe. *J. Petrol.* 50, 1899-  
1117 1933.
- 1118 Georgiev, S., von Quadt, A., Heinrich, C.A., Peytcheva, I., Marchev, P., 2012. Time evolution of a rifted continental  
1119 arc: Integrated ID-TIMS and LA-ICPMS study of magmatic zircons from the Eastern Srednogorie, Bulgaria.  
1120 *Lithos* 154, 53-67.
- 1121 German, C.R., Holliday, B.P., Elderfield, H., 1991. Redox cycling of rare earth elements in the suboxic zone of the  
1122 Black Sea. *Geochim. Cosmochim. Acta* 55, 3553-3558.
- 1123 Glazer, B.T., Luther III, G.W., Konovalov, S.K., Friederich, G.E., Trouwborst, R.E., Romanov, A.S., 2006a. Spatial  
1124 and temporal variability of the Black Sea suboxic zone. *Deep-Sea Res. Pt II* 53, 1756-1768.
- 1125 Glazer, B.T., Luther III, G.W., Konovalov, S.K., Friederich, G.E., Nuzzio, D.B., Trouwborst, R.E., Tebo, B.M.,  
1126 Clement, B., Murray, K., Romanov, A.S., 2006b. Documenting the suboxic zone of the Black Sea via high-  
1127 resolution real-time redox profiling. *Deep-Sea Res. Pt II* 53, 1740-1755.
- 1128 Gnoevaya, N., Gribneva, D., Bogdanova, K., 1982. Mineralogical and petrographic description of the Oligocene in  
1129 Tyulenovo deposit, Tolbuhin district. *Rev. Bulg. Geol. Soc.* 43, 1, 41-49 (in Bulgarian).
- 1130 Gobeil, C., Silverberg, N., 1989. Early diagenesis of lead in Laurentian Trough sediments. *Geochim. Cosmochim.*  
1131 *Acta* 53, 1889-1895.
- 1132 Goldschmidt, V.M., 1954. *Geochemistry*. University Press, Oxford, 730 p.
- 1133 Guilbaud, R., Butler, I.B., Ellam, R.M., 2011. Abiotic pyrite formation produces a large Fe isotope fractionation.  
1134 *Science* 332, 1548-1551.
- 1135 Gültekin, A.H., 1998. Geochemistry and origin of the Oligocene Binkiliç manganese deposit; Thrace Basin, Turkey.  
1136 *Turk. J. Earth Sci.* 7, 11-23.
- 1137 Gültekin, A.H., Balçı, N., 2018. Geochemical characteristics of sedimentary manganese deposit of Binkılıç, Thrace  
1138 Basin, Turkey. *J. Geol. Geophys.* 7, 1000336.

- 1139 Havig, J.R., Hamilton, T.L., McCormick, M., McClure, B., Sowers, T., Wegter, B., Kump, L.R., 2018. Water column  
1140 and sediment stable carbon isotope biogeochemistry of permanently redox-stratified Fayetteville Green Lake,  
1141 New York, USA. *Limnol. Oceanogr.* 63, 570-587.
- 1142 Heiser, U., Neumann, T., Scholten, J., Stüben, D., 2001. Recycling of manganese from anoxic sediments in stagnant  
1143 basins by seawater inflow: a study of surface sediments from the Gotland Basin, Baltic Sea. *Mar. Geol.* 177,  
1144 151-166.
- 1145 Hendy, I.L., 2010. Diagenetic behavior of barite in a coastal upwelling setting. *Paleoceanography* 25, PA4103.
- 1146 Herndon, E.M., Havig, J.R., Singer, D.M., McCormick, M.L., Kump, L.R., 2018. Manganese and iron geochemistry  
1147 in sediments underlying the redox-stratified Fayetteville Green Lake. *Geochim. Cosmochim. Acta.* 231, 50-63.
- 1148 Huff, W.D., Cesta, J., Aucoin, C.D., Harrell, M., Malgieri, T.J., Maynard, J.B., Schwalbaach, C.E., Ugurlu, I., Winrod,  
1149 A., 2014. Evidence for a Volcanogenic Component to the Obrochishte Mn Ore Deposit, Bulgaria: 2014 Annual  
1150 Meeting Geological Society of America, Vancouver, British Columbia.
- 1151 Ivanov, Z., 1988. Aperçu général sur l'évolution géologique et structural du massif des Rhodopes dans le cadre des  
1152 Balkanides. *Bulletin de la Société Géologique de France* 8, IV, 2, 227-240.
- 1153 Ivanova, R., Kamenov, G.D., Yanev, Y., 2002. Sr, Nd, and Pb isotopic geochemistry of rhyolites from the Eastern  
1154 Rhodopes, Bulgaria. *Eos Trans. AGU* 83 (47), Fall Meet. Suppl., V62B-1413.
- 1155 Johnson, J.E., Webb, S.M., Ma, C., Fischer, W.W., 2016. Manganese mineralogy and diagenesis in the sedimentary  
1156 rock record. *Geochim. Cosmochim. Acta.* 173, 210-231.
- 1157 Kalinenko, V.V., Shumikhina, I.V., Gusareva, A.I., 1965. Manganiferous sediments and the distribution of V, Cr, Ni,  
1158 Co and Cu in the Laba Deposit. In: Sapozhnikov, D.G., (Ed.), *Manganese Deposits of the Soviet Union.*  
1159 Moscow, Academy of Sciences of the USSR. English translation, 1970, Jerusalem, Israel Program for  
1160 Scientific Translations, pp. 301-322.
- 1161 Kamenov, G.D., 2008. High-precision Pb isotopic measurements of teeth and environmental samples from Sofia  
1162 (Bulgaria): insights for regional lead sources and possible pathways to the human body. *Environ. Geol.* 55,  
1163 669-680.
- 1164 Kamenov, G.D., Perfit, M.R., Mueller, P.A., Jonasson, I.R., 2008. Controls on magmatism in an island arc  
1165 environment: study of lavas and sub-arc xenoliths from the Tabar-Lihir-Tanga-Feni island chain, Papua New  
1166 Guinea. *Contrib. Mineral. Petrol.* 155, 635-656.

- 1167 Kerner, M., Wallmann, K., 1992. Remobilization events involving Cd and Zn from intertidal flat sediments in the  
1168 Elbe estuary during the tidal cycle. *Estuar. Coast. Shelf Sci.* 35, 371-393.
- 1169 Kim, S.-T., Mucci, A., Taylor, B.E., 2007. Phosphoric acid fractionation factors for calcite and aragonite between 25  
1170 and 75 C: Revisited. *Chem. Geol.* 246, 135-146.
- 1171 Kim, S.-T., Coplen, T.B., Horita, J., 2015. Normalization of stable isotope data for carbonate minerals:  
1172 Implementation of IUPAC guidelines. *Geochim. Cosmochim. Acta* 158, 276-289.
- 1173 Kirchenbaur, M., Münker, C., Schuth, S., Garbe-Schönberg, D., Marchev, P., 2012. Tectonomagmatic constraints on  
1174 the sources of Eastern Mediterranean K-rich lavas. *J. Petrol.* 53, 27-65.
- 1175 Konovalov, S.K., Murray, J.W., Luther, G.W., Tebo, B.M., 2006. Processes controlling the redox budget for the  
1176 oxic/anoxic water column of the Black Sea. *Deep-Sea Res Pt II* 53, 1817-1841.
- 1177 Kuleshov, V.N., 2003. Isotopic composition ( $\delta^{13}\text{C}$ ,  $\delta^{18}\text{O}$ ) and origin of manganese carbonate ores from the Early  
1178 Oligocene deposits, the Eastern Paratethys. *Chem. Erde-Geochem.* 63, 329-363.
- 1179 Kuleshov, V., 2017. *Isotope Geochemistry: The Origin and Formation of Manganese Rocks and Ores*. Elsevier,  
1180 Amsterdam, 440 p.
- 1181 Kuleshov, V.N., Dombrovskaya, Zh.V., 1997. Manganese deposits of Georgia: Communication 1. Geological features  
1182 and isotopic composition of carbonate manganese ore from the Chiatura and Kvirila deposits. *Lithology and  
1183 Mineral Resources* 32, 249-267.
- 1184 Lenz, C., Jilbert, T., Conley, D.J., Wolthers, M., Slomp, C.P., 2015. Are recent changes in sediment manganese  
1185 sequestration in the euxinic basins of the Baltic Sea linked to the expansion of hypoxia? *Biogeosciences* 12,  
1186 4875-4894.
- 1187 Lericolais, G., Bourget, J., Popescu, I., Jorry, S., Popescu, I., Abreu, V., Jouannic, G., Bayon, G., 2012. The “Sink”  
1188 of the Danube River Basin: The Distal Danube Deep-Sea Fan. In: 32nd Annual Gulf Coast SSEPM Foundation  
1189 Bob F. Perkins Research Conference: New Understanding of the Petroleum Systems of Continental Margins  
1190 of the World.
- 1191 Lericolais, G., Bourget, J., Popescu, I., Jermannaud, P., Mulder, T., Jorry, S., Panin, N., 2013. Late Quaternary deep-  
1192 sea sedimentation in the western Black Sea: New insights from recent coring and seismic data in the deep basin.  
1193 *Global Planet. Change* 103, 232-247.
- 1194 Lewis, B.L., Landing, W., 1991. The biogeochemistry of manganese and iron in the Black Sea. *Deep-Sea Res.* 38,

- 1195 S773-S803.
- 1196 Lewis, B.L., Landing, W.M., 1992. The investigation of dissolved and suspended-particulate trace metal fractionation  
1197 in the Black Sea. *Mar. Chem.* 40, 105-141.
- 1198 Li, Y.-H., 2000. *A Compendium of Geochemistry: from Solar Nebula to the Human Brain*. Princeton University Press,  
1199 Princeton, 475 p.
- 1200 Liljedahl, A.K., Gädeke, A., O'Neel, S., Gatesman, T.A., Douglas, T.A., 2017. Glacierized headwater streams as  
1201 aquifer recharge corridors, subarctic Alaska. *Geophys. Res. Lett.* 44, 6876-6885.
- 1202 Luther, G.W. III, Rozan, T.F., Witter, A., Lewis, B., 2001. Metal-organic complexation in the marine environment.  
1203 *Geochem. Trans.* 2, 65.
- 1204 Lyons, T.W., Murray, R.W., Pearson, D.G., 1995. A comparative study of diagenetic pathways in sediments of the  
1205 Caribbean Sea: Highlights from pore-water results. *Proceedings of the Ocean Drilling Program: Scientific*  
1206 *results* 165, 287-298.
- 1207 Mandev, P., 1954. On the Paleogene in the Stalin district. *Annual of Sofia University, Geology* 49, 73-154 (in  
1208 Bulgarian).
- 1209 Marchev, P., Raicheva, R., Downes, H., Vaselli, O., Chiaradia, M., Moritz, R., 2004. Compositional diversity of  
1210 Eocene-Oligocene basaltic magmatism in the Eastern Rhodopes, SE Bulgaria: implications for genesis and  
1211 tectonic setting. *Tectonophysics* 393, 301-328.
- 1212 Marchev, P., Filipov, P., Peytcheva, I., Münker, C., Kirchenbaur, M., 2014. Coeval felsic igneous magmatism of  
1213 Mesta Volcanic Complex and Central Pirin Batholith, SW Bulgaria: evidence for extreme crustal assimilation.  
1214 Abstracts, International Symposium on Eastern Mediterranean Geology. Mugla, Turkey, 13-17 October.2014.
- 1215 Marcus, M.A., Edwards, K.J., Gueguen, B., Fakra, S.C., Horn, G., Jelinski, N.A., Rouxel, O., Sorensen, J., Toner,  
1216 B.M., 2015. Iron mineral structure, reactivity, and isotopic composition in a South Pacific Gyre ferromanganese  
1217 nodule over 4 Ma. *Geochim. Cosmochim. Acta* 171, 61-79.
- 1218 Mayer, J., Rupprecht, B.J., Sachsenhofer, R.F., Tari, G., Bechtel, A., Coric, S., Siedl, W., Kosi, W., Floodpage, J.,  
1219 2017. Source potential and depositional environment of Oligocene and Miocene rocks offshore Bulgaria.  
1220 Geological Society, London, Special Publications 464, 307-328.
- 1221 Maynard, J.B., 2010. The chemistry of manganese ores through time: a signal of increasing diversity of earth-surface  
1222 environments. *Econ. Geol.* 105, 535-552.

- 1223 Maynard, J.B., 2014. Manganiferous sediments, rocks, and ores. In: MacKenzie, F.T. (Ed.), *Treatise of Geochemistry*  
1224 *2<sup>nd</sup> edition. Volume 9, Sediments, Diagenesis, and Sedimentary Rocks*, Elsevier, Amsterdam, pp. 327-349.
- 1225 Maynard, J.B., Okita, P.M., May, E.D., Martinez-Vera, A., 1990. Paleogeographic setting of manganese  
1226 mineralization in the Molango district, Mexico. In: Parnell, J. (Ed.), *Mechanisms of Metal Concentration in*  
1227 *Sedimentary Basins*, London, International Association of Sedimentologists Special Publication 11, pp. 17-30.
- 1228 McArthur, J.M., Howarth, R.J., 2004. Strontium isotope stratigraphy. In: Gradstein, F.M., Ogg, J.G., Smith, A.G.  
1229 (Eds), *A Geologic Time Scale 2004*, Cambridge University Press, Cambridge, pp. 96-105.
- 1230 McLennan, S.M., 1989. Rare earth elements in sedimentary rocks: Influence of provenance and sedimentary  
1231 processes. In: Lipin, B.R., McKay, G.A. (Eds), *Geochemistry and Mineralogy of Rare Earth Elements. Rev.*  
1232 *Mineral.* 21, 169-200.
- 1233 McManus, J., Berelson, W.M., Klinkhammer, G.P., Kilgore, T.E., Hammond, D.E., 1994. Remobilization of barium  
1234 in continental margin sediments. *Geochim. Cosmochim. Acta* 58, 4899-4907.
- 1235 Mikhailova, D., 2009. Water and sediment runoff at the mouths of rivers flowing into the Black Sea. *Environ. Res.*  
1236 *Eng. Manag.* 48, 5-10.
- 1237 Milakovska, Z., Djourova, E., Landjeva, E., 2006. Septarian concretions in lower Oligocene sediments of the  
1238 manganese ore deposit Obrochishte (NE Bulgaria). *CR Acad. Bulg. Sci.* 59, 1031-1038.
- 1239 Moore, W.S., 2010. The effect of submarine groundwater discharge on the ocean. *Annu. Rev. Mar. Sci.* 2, 59-88.
- 1240 Morel, F.M.M., Price, I.G., 2003. The biogeochemical cycles of trace metals in the oceans. *Science* 300, 944-947.
- 1241 Morse, J.W., Berner, R.A., 1995. What determines sedimentary CS ratios? *Geochim. Cosmochim. Acta* 59, 1073-  
1242 1077.
- 1243 Nachev, I.K., 1995. On the Geochemistry of manganese ores in Obrochishte Deposit. *CR Acad. Bulg. Sci.* 48, 55-58.
- 1244 Nikishin, A.M., Okay, A., Tüysüz, O., Demirer, A., Wannier, M., Amelin, N., Petrov, E., 2015. The Black Sea basins  
1245 structure and history: New model based on new deep penetration regional seismic data. Part 2: Tectonic history  
1246 and paleogeography. *Mar. Petrol. Geol.* 59, 656-670.
- 1247 Oaie, G., Secrieru, D., Bondar, C., Ka, S.S., Dutu, L.R., Stanescu, I., Opreanu, G., Dutu, I., Manta, T.V., 2015. Lower  
1248 Danube River: Characterization of sediments and pollutants. *Geo-Eco-Marina* 21, 19-34.

- 1249 Okita, P.M., Maynard, J.B., Spiker, E.C., Force, E.R., 1988. Isotopic evidence for organic matter oxidation by  
1250 manganese reduction in the formation of stratiform manganese carbonate ore. *Geochim. Cosmochim. Acta* 52,  
1251 2679-2685.
- 1252 Öztürk, H., Frakes, L.A., 1995. Sedimentation and diagenesis of an Oligocene manganese deposit in a shallow  
1253 subbasin of the Paratethys: Thrace Basin, Turkey. *Ore Geol. Rev.* 10, 117-132.
- 1254 Peucker-Ehrenbrink, B., Miller, M.W., Arsouze, T., Jeandel, C., 2010. Continental bedrock and riverine fluxes of  
1255 strontium and neodymium isotopes to the oceans. *Geochem. Geophys. Geosyst.* 11, Q03016.
- 1256 Podymov, O.I., Zatsepin, A.G., Ostrovsky, A.G., 2017. Vertical turbulent exchange in the Black Sea pycnocline and  
1257 its relation to water dynamics. *Oceanology* 57, 492-504.
- 1258 Poitrasson, F., Freyrier, R., 2005. Heavy iron isotope composition of granites determined by high resolution MC-ICP-  
1259 MS. *Chem. Geol.* 222, 132-147.
- 1260 Potter, P.E., Maynard, J.B., DePetris, P., 2005. *Mud and Mudstones*. Springer-Verlag, Heidelberg, 297 p.
- 1261 Povinec, P., Ženišová, Z., Šivo, A., Ogrinc, N., Richtáriková, M., Breier, R., 2013. Radiocarbon and stable isotopes  
1262 as groundwater tracers in the Danube River Basin of SW Slovakia. *Radiocarbon* 55, 1017-1028.
- 1263 Puliev, C., Alexiev, B., 1972. On manganese hydrosilicates of Oligocene ore from Northeastern Bulgaria. *Annual of*  
1264 *Sofia University, Geology* 65, 85-96 (in Bulgarian).
- 1265 Pupp, M., Bechtel, A., Ćorić, S., Gratzer, R., Rustamov, J., Sachsenhofer, R.F., 2018. Eocene and Oligo-Miocene  
1266 source rocks in the Rioni and Kura basins of Georgia: depositional environment and petroleum potential. *J.*  
1267 *Petrol. Geol.* 41, 367-392.
- 1268 Raiswell, R., Berner, R.A., 1986. Pyrite and organic matter in Phanerozoic normal marine shales. *Geochim.*  
1269 *Cosmochim. Acta* 50, 1967-1976.
- 1270 Randazzo, L.A., Censi, P., Saiano, F., Zuddas, P., Aricò, P., Mazzola, S., 2009. Trace elements release from volcanic  
1271 ash to seawater. Natural concentrations in Central Mediterranean sea. *Geophys. Res. Abstr.* 11, 2131.
- 1272 Rank, D., Wyhlidal, S., Schott, K., Jung, M., Heiss, G., Tudor, M., 2014. A 50 years' isotope record of the Danube  
1273 River water and its relevance for hydrological, climatological and environmental research. *Acta Zool. Bulgar.*  
1274 (Supplementum 7), 109-115.
- 1275 Retallack, G.J., 2010. Lateritization and bauxitization events. *Econ. Geol.* 105, 655-667.
- 1276 Rolison, J.M., Stirling, C.H., Middag, R., Gault-Ringold, M., George, E., Rijkenberg, M.J.A., 2018. Iron isotope

- 1277 fractionation during pyrite formation in a sulfidic Precambrian ocean analogue. *Earth Planet. Sci. Lett.* 488, 1-  
1278 13.
- 1279 Rouxel, O.J., Bekker, A., Edwards, K.J., 2005. Iron isotope constraints on the Archean and Paleoproterozoic ocean  
1280 redox state. *Science* 307, 1088-1091.
- 1281 Rouxel, O., Sholkovitz, E., Charrette, M., Edwards, K.J., 2008. Iron isotope fractionation in subterranean estuaries.  
1282 *Geochim. Cosmochim. Acta* 72, 3413-3430.
- 1283 Sachsenhofer, R.F., Stummer, B., Georgiev, G., Dellmour, R., Bechtel, A., Gratzner, R., Ćorić, S., 2009. Depositional  
1284 environment and hydrocarbon source potential of the Oligocene Ruslar Formation (Kamchia Depression;  
1285 western Black Sea). *Mar. Petrol. Geol.* 26, 57-84.
- 1286 Sachsenhofer, R.F., Hentschke, J., Bechtel, A., Coric, S., Gratzner, R., Gross, D., Horsfield, B., Rachetti, A., Soliman,  
1287 A., 2015. Hydrocarbon potential and depositional environments of Oligo-Miocene rocks in the Eastern  
1288 Carpathians (Vrancea Nappe, Romania). *Mar. Petrol. Geol.* 68, 269-290.
- 1289 Sachsenhofer, R.F., Popov, S.V., Akhmetiev, M.A., Bechtel, A., Gratzner, R., Groß, D., Horsfield, B., Rachetti, A.,  
1290 Rupprecht, B., Schaffar, W.B., Zaporozhets, N.I., 2017. The type section of the Maikop Group (Oligocene–  
1291 lower Miocene) at the Belaya River (North Caucasus): Depositional environment and hydrocarbon potential.  
1292 *AAPG Bull.* 101, 289-319.
- 1293 Santos, I.R., Cook, P.L.M., Rogers, L., de Weys, J., Eyre, B.D., 2012. The “salt wedge pump”: Convection-driven  
1294 pore-water exchange as a source of dissolved organic and inorganic carbon and nitrogen to an estuary. *Limnol.*  
1295 *Oceanogr.* 57, 1415-1426.
- 1296 Schijf, J., de Baar, H.J.W., Wijbrans, J.R., Landing, W.M., 1991. Dissolved rare earth elements in the Black Sea.  
1297 *Deep-Sea Res.* 38, S805-S823.
- 1298 Schubert, M., Knöller, K., Stollberg, R., Mallast, U., Ruzsa, G., Melikadze, G., 2017. Evidence for submarine  
1299 groundwater discharge into the Black Sea - investigation of two dissimilar geographical settings. *Water* 9, 468.
- 1300 Schulz, H.-M., Bechtel, A., Sachsenhofer, R.F., 2005. The birth of the Paratethys during the early Oligocene: from  
1301 Tethys to an ancient Black Sea analogue? *Global Planet. Change* 49, 163-176.
- 1302 Scott, C., Lyons, T.W., 2012. Contrasting molybdenum cycling and isotopic properties in euxinic versus non-euxinic  
1303 sediments and sedimentary rocks: Refining the paleoproxies. *Chem. Geol.* 324, 19-27.
- 1304 Severmann, S., Lyons, T.W., Anbar, A., McManus, J., Gordon, G., 2008. Modern iron isotope perspective on the

- 1305 benthic iron shuttle and the redox evolution of ancient oceans. *Geology* 36, 487-490.
- 1306 Severmann, S., McManus, J., Berelson, W.M., Hammond, D.E., 2010. The continental shelf benthic iron flux and its  
1307 isotope composition. *Geochim. Cosmochim. Acta* 74, 3984-4004.
- 1308 Sharma, T., Clayton, R.N., 1965. Measurement of  $^{18}\text{O}/^{16}\text{O}$  ratios of total oxygen of carbonates. *Geochim. Cosmochim.*  
1309 *Acta* 29, 1347-1353.
- 1310 Stacey, J.S., Kramers, J.D., 1975. Approximation of terrestrial lead isotope evolution by a two-stage model. *Earth*  
1311 *Planet. Sci. Lett.* 26, 207-221.
- 1312 Stille, P., Steinmann, M., Riggs, S.R., 1996. Nd isotope evidence for the evolution of the paleocurrents in the Atlantic  
1313 and Tethys Oceans during the past 180 Ma. *Earth Planet. Sci. Lett.* 144, 9-19.
- 1314 Stoyanov, E., 1961. On the stratigraphic division of Oligocene in Varna district. *Annuaire de la Direction Generale*  
1315 *des Recherches Geologiques* 12, 123-140 (in Bulgarian).
- 1316 Stoyanov, E., 1963. Physico-geographical conditions of the Oligocene basin in the Varna district and southeast  
1317 Dobrodja. *Rev. Bulg. Geol. Soc.* 24, 29-38 (in Bulgarian).
- 1318 Sun, S.-S., McDonough, W.F., 1989. Chemical and isotopic systematics of oceanic basalts: implications for mantle  
1319 composition and processes. In: Saunders, A.D., Norry, M.J., (Eds), *Magmatism in the Ocean Basins*. *Geol.*  
1320 *Soc. Spec. Publ.* 42, 313-345.
- 1321 Szymczycha, B., Pempkowiak, J., 2016. State of art and theory of submarine groundwater discharge (SGD). In:  
1322 Szymczycha, B., Pempkowiak, J., (Eds), *The Role of Submarine Groundwater Discharge as Material Source*  
1323 *to the Baltic Sea*. Springer International Publishing, Switzerland, pp. 3-32.
- 1324 Tenchov, Y., (Ed.) 1993. *Glossary of the Formal Lithostratigraphic units in Bulgaria (1882-1982)*. Bulgarian Academy  
1325 of Sciences Publisher, Sofia, 397 p. (in Bulgarian).
- 1326 Tripathi, A., Darby, D., 2018. Evidence for ephemeral middle Eocene to early Oligocene Greenland glacial ice and  
1327 pan-Arctic sea ice. *Nat. Commun.* 9, 1038.
- 1328 Vangelova, V., Vangelov, D., Cvetkov, P., 2005. Genesis of Oligocene manganese ore in Northeast Bulgaria. *Annual*  
1329 *of Sofia University, Geology* 98, 213-230 (in Bulgarian).
- 1330 Varentsov, I.M., 2002. Genesis of the Eastern Paratethys manganese ore giants: impact of events at the  
1331 Eocene/Oligocene boundary. *Ore Geol. Rev.* 20, 65-82.
- 1332 Varentsov, I.M., Rakhmanov, V.P., 1980. Manganese deposits of the USSR (a review). In: Varentsov, I.M., Grasselly,

- 1333 Gy., (Eds), *Geology and Geochemistry of Manganese*. Stuttgart, E. Schweizerbart'sche Verlagsbuchhandlung,  
1334 2, pp. 319-392.
- 1335 Varentsov, I.M., Sokolova, A.L., Gor'kova, N.V., Stolyarov, A.S., Ivleva, E.I., Potkonen, N.I., Gorshkov, A.I., 1997.  
1336 On a geochemical model of the formation of Early Oligocene manganese ores in the Eastern Paratethys: the  
1337 Nikopol' and other deposits of the southern Ukrainian Basin. *Geology of Ore Deposits* 39, 40-57.
- 1338 Vassilev, L., 1967. Mineralogical features of Obrochishte manganese deposit and some implications for its exploration  
1339 and grade evaluation. *Rudodobiv* 3, 9-13 (in Bulgarian).
- 1340 Vassilev, L., Zapryanova, N., Nikiforov, N., 1958. Studies on manganese ores and their host rocks in Varna district.  
1341 *Annuaire de la Direction Generale des Recherches Geologiques* 8, 139-210 (in Bulgarian).
- 1342 Weyer, S., Schwieters, J.B., 2003. High precision Fe isotope measurements with high mass resolution MC-ICPMS.  
1343 *Int. J. Mass Spectrom.* 226, 355-368.
- 1344 Whittaker, E.J.W., Muntus, R., 1970. Ionic radii for use in geochemistry. *Geochim. Cosmochim. Acta* 34, 945-956.
- 1345 Windom, H.L., Moore, W.S., Niencheski, L.F.H., Jahnke, R.A., 2006. Submarine groundwater discharge: A large,  
1346 previously unrecognized source of dissolved iron to the South Atlantic Ocean. *Mar. Chem.* 102, 252-266.
- 1347 Yiğiterhan, O., Murray, J.W., 2008. Trace metal composition of particulate matter of the Danube River and Turkish  
1348 rivers draining into the Black Sea. *Mar. Chem.* 111, 63-76.
- 1349 Yiğiterhan, O., Murray, J.W., Tuğrul, S., 2011. Trace metal composition of suspended particulate matter in the water  
1350 column of the Black Sea. *Mar. Chem.* 126, 207-228.
- 1351 Zachos, J., Pagani, M., Sloan, L., Thomas, E., Billups, K., 2001. Trends, rhythms, and aberrations in global climate  
1352 65 Ma to Present. *Science* 292, 686-693.

1354 **Figure captions**

1355

1356 **Fig. 1.** (A) Simplified geological map of the tectonic framework of Bulgaria (after Ivanov, 1988)

1357 with the location of the studied north-eastern region (B). Each tectonic unit includes several

1358 geomorphology structures. Some of them (not all) are mentioned in the paper: e.g., the Balkan

1359 Zone includes Stara Planina Mountains, Sredna gora Zone includes Sredna gora (Srednogorie) and

1360 Vitoshka Mountains, Sakar-Strandzha Zone includes Strandzha Mountains, and Rhodope Massif

1361 includes Rhodope Mountains and Mesta Basin. (B) Map of the distribution of the Ruslar Formation

1362 in the NE Bulgaria and adjacent Black Sea shelf (based on unpublished data of Juranov and

1363 Valchev from 338 drill holes) with the sample sites: white circles = drill holes, black circles =

1364 outcrops, black star = mine. Legend: I = Ruslar Formation, in general; II = under-marl unit with

1365 the Mn-ore bed at the base; III = marl unit; IV = over-marl unit; V = boundaries of extension of

1366 the lithostratigraphic units (LSU), a – proven, b – extrapolated; VI = edge of the continental shelf;

1367 VII = fault. Sample site numbers: 1 = C-258a Dobruja drill hole (sample OBR-1-3270), 2 = C-

1368 140a Dobruja drill hole (sample OBR-2-1601), 3 = C-170a Dobruja drill hole (sample OBR-3-

1369 1622), 4 = C-3a Makedonka drill hole (sample OBR-4-1413), 5 = C-138a Dobruja drill hole

1370 (samples OBR-5-1261, -1262, -1263, -1264, -1265, -1266, -1267; -1302), 6 = NE of Pripek village

1371 (sample OBR-6-3186), 7 = Kalimanski dol (samples OBR-7-3178, -3205, -4130, -4131), 8 = E of

1372 Pripek village (samples OBR-8-4136, -3193, -A, -B), 9 = Ichme kulak (samples OBR-9-3884, -

1373 3885), 10 = Kondulak cheshme (sample OBR-10-164), 11 = Obrochishte mine (samples OBR-11-

1374 1.2, -1.8, -2.8, -3.8, -4.4, -5.1, -5.7, -6.1). Summary lithostratigraphic core logs representative for

1375 different areas (arrows) are shown at the right-hand side.

1376

1377 **Fig. 2.** Chunk of Mn-ore with concentrically-laminated pisoliths of Mn-carbonates within matrix  
 1378 of Mn-carbonates and clays (sample OBR-11-5.7).

1379

1380 **Fig. 3.** Photomicrographs (optical polarizing microscope; sample OBR-11-1.2) of: (A) pisolith  
 1381 layers (transmitted light,  $\parallel N$ ); (B) the same as at (A) at  $\times N$ , note the carbonate-rich layers (high  
 1382 interference colors) alternating with carbonate-poor layers (light to dark brown); (C) rhodochrosite  
 1383 (rh) layers in pisolith (transmitted light,  $\parallel N$ ); (D) the same as at (C) at  $\times N$ ; (E) veins of pyrite  
 1384 (black; py) in matrix of Mn-carbonate and clays, note the thin rims of rhodochrosite (white; rh)  
 1385 along the pyrite veins (transmitted light,  $\parallel N$ ); (F) the same as at (E) in reflected light at  $\parallel N$ ; (G)  
 1386 pyrite vein (white; py) (close up) with rhodochrosite rhombic crystals (greyish-black; rh) (reflected  
 1387 light,  $\parallel N$ ); (H) pyrite vein (white; py) (close up) with secondary alterations along cracks and  
 1388 rhodochrosite rhombic crystals (greyish-black; rh) (reflected light,  $\parallel N$ ).

1389

1390 **Fig. 4.** X-ray fluorescence maps of the distribution of elements across a pisolith within the ore  
 1391 matrix (sample OBR-11-6.1): (A) microphotograph (thin polished section) of the pisolith, general  
 1392 view; (B) X-ray fluorescence scan in Mn  $K_{\alpha}$ ; (C) X-ray fluorescence scan in Ca  $K_{\alpha}$ ; (D) X-ray  
 1393 fluorescence scan in Al  $K_{\alpha}$ ; (E) X-ray fluorescence scan in Si  $K_{\alpha}$ ; (F) X-ray fluorescence scan in  
 1394 Fe  $K_{\beta}$ ; (G) X-ray fluorescence scan in Rb  $K_{\alpha}$ ; (H) X-ray fluorescence scan in Zr  $K_{\alpha}$ . Brighter colors  
 1395 correspond to higher concentrations.

1396

1397 **Fig. 5.** SEM photomicrographs (SEI; sample OBR-11-6.1) of: (A) laminae of carbonate  
 1398 (composition is consistent with Ca-rhodochrosite:  $Mn_{80}Ca_{11}Mg_7Fe_2$  (mole %)) in pisolith; (B) sub-  
 1399 micron spheres (Si/Mn = 3/1) likely composed of silica and rhodochrosite.

1400

1401 **Fig. 6.** X-ray fluorescence maps of the distribution of elements across a pyrite vein within the ore  
 1402 matrix (sample OBR-11-1.2): (A) microphotograph (thin polished section) of the pyrite (py) vein  
 1403 (black), general view; (B) X-ray fluorescence scan in Fe  $K_{\beta}$ ; (C) X-ray fluorescence scan in S  $K_{\alpha}$ .  
 1404 Brighter colors correspond to higher concentrations.

1405

1406 **Fig. 7.** Correlation between  $S_{\text{tot}}$  and  $C_{\text{org}}$  concentrations in the studied samples.

1407

1408 **Fig. 8.** C1 chondrite-normalized (Sun and McDonough, 1989) REE distribution patterns of  
 1409 samples: (A) OBR-11-1.8 (Mn-ore bed); (B) OBR-11 (Mn-ore bed): bulks, 2N HCl leachates,  
 1410 residues; (C) OBR-11 (Mn-ore bed): 2N HCl pisolith leachates, pisolith residues; (D) OBR-5 (Mn-  
 1411 ore bed): 2N HCl leachates, residues; (E) oxic (50 m water depth), suboxic (100 m water depth)  
 1412 and anoxic (2185 m water depth) seawater from Black Sea (German et al., 1991); (F) OBR-8-A  
 1413 (above Mn-ore bed) and average UCC (McLennan, 1989).

1414

1415 **Fig. 9.** C and O stable isotope correlation diagrams of studied carbonates from Ruslar Formation:  
 1416 (A)  $\delta^{18}\text{O} - \delta^{13}\text{C}$  correlation diagram. Note, the two arrays of the data point distribution: one at  
 1417 constant  $\delta^{18}\text{O}$ , the other with linear  $\delta^{18}\text{O} - \delta^{13}\text{C}$  correlation. Oligocene seawater data from  
 1418 Armstrong-McKay et al. (2016); modern Danube River water data from Povinec et al. (2013) and  
 1419 Rank et al. (2014). (B)  $\delta^{13}\text{C} - \text{MnO}$  correlation diagram. Note, the two trends in data point  
 1420 distribution suggesting two sources of C in Mn carbonates. Squares = samples from the southern  
 1421 part of Ruslar Formation (sites ##6, 7, 8, 9, 10; Fig. 1B); circles (open, blue and green) = samples

1422 from the northern part of Ruslar Formation (sites ##1, 2, 3, 5, 11); blue circles = upper part of Mn-  
1423 ore bed at site #11; green circles = lower part of Mn-ore bed at site #5.

1424

1425 **Fig. 10.** Comparison of Sr isotopic compositions of bulk, leachate and residue samples with  
1426 seawater Sr isotope curve. Note, the residue for sample OBR-5-1264 ( $^{87}\text{Sr}/^{86}\text{Sr}=0.72038$ ) plots  
1427 beyond the scale of the plot. Seawater Sr curve from McArthur and Howarth (2004).

1428

1429 **Fig. 11.** Comparison of Nd isotopic compositions of bulk, leachate and residue samples with  
1430 Atlantic and Tethys seawater. Seawater field after Stille et al. (1996).

1431

1432 **Fig. 12.** Pb isotopic compositions of bulk, leachate and residue samples compared to Srednogorie  
1433 Arc (including Vitosha volcano-magmatic complex) and Stara Planina detritus. Note that there is  
1434 no particular trend between leachates and residues. Overall, Obrochishte Pb isotopes do not show  
1435 any significant mantle input and indicate derivation from crustal sources. Srednogorie Arc data  
1436 from Georgiev et al. (2009), Vitosha and Stara Planina from Kamenov (2008), Continental crust  
1437 and Mantle evolution lines from Stacey and Kramers (1975).

1438

1439 **Fig. 13.** Schematic representation of our hypothesis for the sources of Mn, accumulation of  
1440 dissolved Mn in the Oligocene Western Black Sea water, modes of Mn deposition at the shelf, and  
1441 formation of Obrochishte Mn deposit (Ruslar Formation, Oligocene Series). (A) Enhanced  
1442 chemical weathering during the Eocene weathering phase (EECO, 50-52 Ma) resulted in thick  
1443 laterite crusts rich in Fe- and Mn-oxyhydroxides in the drainage basin of the Western Black Sea.  
1444 World Ocean (including Western Black Sea) was characterized by a high sea-level stand during

1445 this warm epoch. Groundwater table in the drainage basin was high. (B) Late Eocene cooling that  
1446 peaked at the Eocene-Oligocene transition (33-35 Ma) led to glaciations (continental ice sheets  
1447 and sea ice) in both hemispheres. This resulted in low (global) sea-level stand, isolation of the  
1448 small marine basins (e.g., Black Sea) which in turn provoked onset of anoxia conditions. Sea-level  
1449 fall drew down the erosional basis of the rivers that led to increased erosion of the laterite crusts.  
1450 Residually accumulated Fe- and Mn-oxyhydroxides in the laterites were swept away into the  
1451 ocean. In vertically stratified anoxic marine basins (with oxic, suboxic and anoxic water layers)  
1452 they remained in suspended state in the oxic and suboxic water layers, but were dissolved in the  
1453 anoxic deep waters when they sank down. In anoxic-euxinic waters (with free HS<sup>-</sup>) dissolved Fe  
1454 and other chalcophile elements (e.g., Cu, Zn, Pb) were immobilized as sulfides, which settled on  
1455 the seafloor while dissolved Mn was accumulated in seawater. (C) Early Oligocene warming (25-  
1456 32 Ma) caused glacier and sea ice melting, and rise of both sea-level and groundwater table. In the  
1457 anoxic Western Black Sea the suboxic layer migrated upward (synchronously with sea-level rise)  
1458 and impinged on the shelf. Steep gradient of the dissolved Mn<sup>2+</sup> concentration across the suboxic-  
1459 anoxic interface and turbulent mixing caused dissolved Mn flux (molecular diffusion and eddies)  
1460 from the deep Mn storage to the suboxic water layer. Part of dissolved Mn<sup>2+</sup> precipitated as MnO<sub>2</sub>  
1461 and the amount of immobilized Mn<sup>2+</sup> was controlled by the available O<sub>2</sub> in this layer. Sinking  
1462 MnO<sub>2</sub> particles could either fall back in the anoxic water where they re-dissolved (Mn<sup>2+</sup>), or settle  
1463 on the seafloor in the suboxic layer. The last could be reduced in the presence of organic matter in  
1464 the sediment and liberated Mn<sup>2+</sup> may react with CO<sub>2</sub> and precipitate as MnCO<sub>3</sub> (diagenetic  
1465 precipitation). High groundwater table would produce high SGD flux through the seafloor which  
1466 will supply HCO<sub>3</sub><sup>-</sup> and alkalinity to the suboxic water layer. Excess dissolved Mn<sup>2+</sup> in the suboxic  
1467 layer would react with HCO<sub>3</sub><sup>-</sup> in the alkaline environment and precipitate as MnCO<sub>3</sub> in the water

1468 column (authigenic precipitation). Volcanic ash fall contemporary of  $\text{MnCO}_3$  precipitation had  
 1469 supplied additional amount of Mn (through partial dissolution of ash particles) to the basin.  
 1470 Manganese diffusion-turbulent pump from the deep anoxic Mn storage to the suboxic water layer  
 1471 would supply Mn enough for formation of large Mn deposits around the Oligocene Black Sea.

1472

1473 **Fig. 14.**  $\delta^{18}\text{O} - \delta^{13}\text{C}$  and  $\delta^{13}\text{C} - \text{MnO}$  correlation diagrams of Mn-ore samples from Binkiliç (A,  
 1474 B) [data from Öztürk and Frakes (1995)], Chiatura (C, D) [data from Kuleshov and Dombrovskaya  
 1475 (1997)], and Mangyshlak (E, F) [data from Kuleshov (2003, 2017)] deposits.

- 1476 • Mn-carbonate ore at the Obrochishte has dual origin: diagenetic and authigenic
- 1477 • Mn deposition was a result of the climatic events at the Late Eocene-Early Oligocene
- 1478 • Mn ore was deposited in a redox-stratified basin, similar to the modern Black Sea

1479

1480 Editorial Board  
 1481 *Ore Geology Reviews*

1482

1483 Prof. Vesselin Dekov  
 1484 Department of Marine Resources and Energy  
 1485 Tokyo University of Marine Science and Technology  
 1486 4-5-7 Konan, Minato-ku  
 1487 Tokyo 108-8477  
 1488 Japan  
 1489 E-mail: [vdekov0@kaiyodai.ac.jp](mailto:vdekov0@kaiyodai.ac.jp)

1490

1491 November 14, 2019

1492

1493 Dear Sirs,

1494

1495 I, on behalf of my co-authors, declare that there is no conflict of interests in our work submitted to  
 1496 your Journal as manuscript entitled "Origin of the Oligocene manganese deposit at Obrochishte (Bulgaria):  
 1497 Insights from C, O, Fe, Sr, Nd, and Pb isotopes" by V.M. Dekov, J.B. Maynard, G.D. Kamenov, O. Rouxel, S.  
 1498 Lalonde and S. Juranov. The manuscript is an original work, not published elsewhere or under  
 1499 consideration for publication elsewhere.

1500

1501

1502  
1503  
1504  
1505

Sincerely Yours

Vesselin Dekov

1506  
1507**Table 1**

Investigated samples from the Oligocene Mn-ore layer in NE Bulgaria.

Sample ID	Sample type	Sample site	Stratigraphic position	Position, m above base	Mineralogy <sup>a</sup>								
					Rhodochrosite	Kutnahorite	Mn-calcite	Dolomite	Apatite	Quartz	Plagioclase	Illite-smectite	Kaolinite
OBR-1-3270 <sup>b</sup>	drill core	C-258a Dobruja	lower part of Ruslar Fmn	below Mn-rich layer	-	2	49	-	-	18	-	31	-
OBR-2-1601	drill core	C-140a Dobruja	lower part of Ruslar Fmn	Mn-rich layer	32	16	-	31	-	14	7	-	-
OBR-3-1622	drill core	C-170a Dobruja	Ruslar Fmn	-	-	-	-	-	-	-	-	-	-
OBR-4-1413	drill core	Makedonka	lower part of Ruslar Fmn	4.4 above Mn-rich layer;	-	-	-	-	-	8	14	77	-
OBR-5-1261	drill core	C-138a Dobruja	lower part of Ruslar Fmn	13.8 uppermost Mn-rich layer;	-	1	-	-	-	17	28	52	3
OBR-5-1262	drill core	C-138a Dobruja	lower part of Ruslar Fmn	12.4 Mn-rich layer;	32	32	36	-	-	-	-	-	-
OBR-5-1263	drill core	C-138a Dobruja	lower part of Ruslar Fmn	11.3 Mn-rich layer;	-	7	-	-	-	18	-	75	-
OBR-5-1264	drill core	C-138a Dobruja	lower part of Ruslar Fmn	9.3 Mn-rich layer;	15	46	-	-	-	25	14	-	-
OBR-5-1265	drill core	C-138a Dobruja	lower part of Ruslar Fmn	6.3 Mn-rich layer;	22	56	-	-	-	22	-	-	-
OBR-5-1266	drill core	C-138a Dobruja	lower part of Ruslar Fmn	0.9 base Mn-rich layer;	13	24	-	-	-	41	22	-	-
OBR-5-1267	drill core	C-138a Dobruja	lower part of Ruslar Fmn	0.1 Mn-rich layer	-	26	-	-	-	74	-	-	-
OBR-5-1302	drill core	C-138a Dobruja	lower part of Ruslar Fmn	NE of	-	-	-	-	-	-	-	-	-
OBR-6-3186	outcrop	Pripek village	lower part of Ruslar Fmn	-	-	-	-	-	-	-	-	-	-
OBR-7-3178	outcrop	Kalimanski dol	lower part of Ruslar Fmn	-	-	23	-	-	-	60	-	17	-
OBR-7-3205	outcrop	Kalimanski dol	lower part of Ruslar Fmn	-	-	-	-	-	-	-	-	-	-

OBR-7-4130	outcrop	Kalimans ki dol	lower part of Ruslar Fmn	- below Mn- rich layer below	1	-	16	-	-	34	31	17	1
OBR-7-4131	outcrop	Kalimans ki dol	lower part of Ruslar Fmn	rich layer below	-	-	-	-	-	42	31	22	5
OBR-8-3193	outcrop	E of Pripek village	lower part of Ruslar Fmn	rich layer	-	-	-	-	-	36	-	64	-
OBR-8-4136	outcrop	Pripek village	Avren Fmn	-	-	-	35	-	-	60	-	5	-
OBR-8-A	outcrop	E of Pripek village	lower part of Ruslar Fmn	rich layer	-	-	73	-	-	24	3	-	-
OBR-8-B	outcrop	E of Pripek village	lower part of Ruslar Fmn	rich layer	-	-	-	-	-	-	-	-	-
OBR-9-3884	outcrop	Ichme kulak	lower part of Ruslar Fmn	rich layer above	-	-	27	-	-	14	28	31	-
OBR-9-3885	outcrop	Ichme kulak	lower part of Ruslar Fmn	rich layer	-	-	-	-	-	-	-	-	-
OBR-10-164	outcrop	Kondulak cheshme	Ruslar Fmn	7.4 Mn- rich layer;	-	-	-	-	-	-	-	-	-
OBR-11-1.2 <sup>c</sup>	mine	Obrochish te	Ruslar Fmn	1.2 Mn- rich layer;	29	39	-	32	-	-	-	-	-
OBR-11-1.8	mine	Obrochish te	Ruslar Fmn	1.8 Mn- rich layer;	73	24	-	-	-	1	-	2	-
OBR-11-2.8	mine	Obrochish te	Ruslar Fmn	2.8 Mn- rich layer;	95	-	-	-	-	-	-	5	-
OBR-11-3.8	mine	Obrochish te	Ruslar Fmn	3.8 Mn- rich layer;	95	-	-	-	-	5	-	-	-
OBR-11-4.4	mine	Obrochish te	Ruslar Fmn	4.4 Mn- rich layer;	97	-	-	-	-	2	-	1	-
OBR-11-5.1	mine	Obrochish te	Ruslar Fmn	5.1 Mn- rich layer;	100	-	-	-	-	-	-	-	-
OBR-11-5.1P <sup>d</sup>	mine	Obrochish te	Ruslar Fmn	5.1 Mn- rich layer;	100	-	-	-	-	-	-	-	-
OBR-11-5.7	mine	Obrochish te	Ruslar Fmn	5.7 Mn- rich layer;	-	-	-	-	-	-	-	-	-
OBR-11-6.1	mine	Obrochish te	Ruslar Fmn	6.1 Mn- rich layer;	61	11	-	-	-	-	-	28	-
OBR-11-6.1M <sup>e</sup>	mine	Obrochish te	Ruslar Fmn	6.1 Mn- rich layer;	49	-	-	-	-	2	-	49	-
OBR-11-6.1M <sup>e</sup>	mine	Obrochish te	Ruslar Fmn	Mn- rich layer;	90	-	-	-	9	-	-	-	-

11- te rich  
6.1P layer;  
6.1

1508  
1509  
1510  
1511  
1512  
1513

<sup>a</sup> %, X-ray diffraction with Rietveld refinement quantification.

<sup>b</sup> The last four digits of the drill core sample IDs denote the depth (m) below surface.

<sup>c</sup> The last two digits of the mine sample IDs denote the distance (m) from the lower boundary of the Mn-ore layer.

<sup>d</sup> Pisolith.

<sup>e</sup> Matrix.

1514 **Table 2**

1515 EDX data for sample OBR-11-4.4.

	Matrix	Pisolith
SiO <sub>2</sub> , wt. %	19.2	6.40
Al <sub>2</sub> O <sub>3</sub>	3.57	0.19
CaO	2.80	4.09
MgO	5.44	2.24
Fe <sub>2</sub> O <sub>3</sub>	1.80	0.79
MnO	35.6	52.9
CO <sub>2</sub> <sup>a</sup>	31.5	33.7
Total	100.0	100.4

1516 <sup>a</sup> Measured C<sub>tot</sub> (C<sub>inorg</sub>+C<sub>org</sub>) recalculated as CO<sub>2</sub> considering that 88% of C<sub>tot</sub> is as C<sub>inorg</sub> in  
1517 carbonates (bulk sample analyses; Table 3).  
1518

1519 **Table 3**

1520 Chemical composition (XRF) of bulk samples and separated pisoliths.

Sample ID <sup>a</sup>	Si O <sub>2</sub> wt. %	Al <sub>2</sub> O <sub>3</sub>	Ca O	Mg O	Fe <sub>2</sub> O <sub>3</sub>	Mn O	K <sub>2</sub> O	Na <sub>2</sub> O	Ti O <sub>2</sub>	P <sub>2</sub> O <sub>5</sub>	L OI	H <sub>2</sub> O <sup>-</sup>	H <sub>2</sub> O <sup>+</sup>	C <sub>to</sub> t <sup>b</sup>	C <sub>or</sub> g <sup>b</sup>	C <sub>ino</sub> r <sup>b</sup>	S <sub>tot</sub> <sup>b</sup> ppm	Total wt. %	Mo ppm
<i>Detection limits</i>	0.4	0.5	2	0.1	2	2	1	0.2	1	0.1	0.2	0.2	0.2	2	2	2	20		3
<b>OBR-1-3270</b>	<b>30.1</b>	<b>13.0</b>	<b>16.8</b>	<b>2.9</b>	<b>8.1</b>	<b>0.0</b>	<b>1.8</b>	<b>0.2</b>	<b>0.6</b>	<b>b.d.</b>	<b>26.4</b>	<b>3.5</b>	<b>22.8</b>	<b>4.3</b>	<b>0.5</b>	<b>3.8</b>	<b>479</b>	<b>100</b>	<b>b.d.</b>
OBR-2-1601	24.0	12.4	14.1	1.1	1.3	18.9	1.5	0.6	0.1	0.2	25.6	1.1	24.5	5.8	0.2	5.6	430	99.	b.d.
OBR-3-1622	53.9	8.8	1.6	1.1	3.2	8.8	2.4	1.3	0.1	0.2	16.4	2.4	14.1	3.6	0.1	3.5	685	98.	b.d.
<b>OBR-5-1261</b>	<b>55.8</b>	<b>15.8</b>	<b>0.4</b>	<b>1.8</b>	<b>8.0</b>	<b>0.0</b>	<b>2.4</b>	<b>1.6</b>	<b>0.7</b>	<b>0.1</b>	<b>12.3</b>	<b>2.9</b>	<b>9.3</b>	<b>1.1</b>	<b>1.1</b>	<b>0.0</b>	<b>422</b>	<b>99.</b>	<b>3.3</b>
OBR-5-1262	54.9	14.5	0.4	1.7	8.6		2.4	1.6	0.8	0.1	13.0	3.1	9.8	1.2	1.3		573	98.	81.
OBR-5-1263	20.7	12.7	2.7	2.5	1.5	21.6	1.2	1.1	0.2	0.5	33.8	1.2	32.6	8.1	0.4	7.6	132	99.	11.
OBR-5-1264	51.5	16.4	0.4	1.8	8.1	0.2	2.6	1.1	0.9	0.1	15.7	3.8	11.8	0.8	0.7	0.1	388	99.	b.d.
OBR-5-1265	47.4	15.5	0.4	1.7	8.0	0.2	2.4	1.0	0.9	0.1	21.3	0.3	20.9	6.3	0.2	6.1	375	99.	b.d.
OBR-5-1266	23.0	12.6	13.3	3.2	4.6	15.6	1.3	0.8	0.2	0.3	24.1	1.1	22.9	6.1	0.3	5.7	256	99.	b.d.
OBR-5-1267	48.7	11.0	15.5	4.1	4.5	5.1	2.2	1.5	0.5	0.2	4.9	0.4	4.5	3.0	0.3	2.7	341	98.	b.d.
OBR-5-1302	67.1	4.0	3.6	1.7	2.6	4.8	1.4	0.7	0.0	0.0	12.9	2.0	10.1	2.2	0.2	1.9	218	100	27.
OBR-6-3186	40.7	12.7	10.8	2.1	3.7	7.1	2.1	0.6	0.5	0.2	18.2	2.0	16.1	2.2	0.1	2.1		99.	17.
OBR-7-3178	34.9	14.1	2.9	1.5	2.9	15.2	0.5	0.2	0.3	0.3	24.5	5.5	18.7	0.5	0.1	0.4	416	99.	b.d.
OBR-7-3205	40.6	13.7	8.6	2.0	6.2	1.5	2.4	b.d.	0.5	0.1	23.4	4.9	18.1	2.8	0.3	2.4	503	99.	19.

OBR-7-4130	41.	13.	7.2	2.2	3.2	8.0	2.4	0.6	0.5	0.2	20.	3.8	16.	1.5	0.1	1.3	101	99.	4.3
OBR-7-4131	<b>60.</b>	<b>15.</b>	<b>3.2</b>	<b>0.5</b>	<b>3.9</b>	<b>0.2</b>	<b>2.2</b>	<b>0.8</b>	<b>0.6</b>	<b>0.1</b>	<b>11.</b>	<b>2.5</b>	<b>9.1</b>	<b>1.4</b>	<b>0.5</b>	<b>0.9</b>	<b>120</b>	<b>99.</b>	<b>4.6</b>
OBR-8-3193	<b>53.</b>	<b>18.</b>	<b>0.2</b>	<b>2.4</b>	<b>4.3</b>		<b>0.7</b>	<i>b.d.</i>	<b>0.1</b>	<i>b.d.</i>	<b>19.</b>	<b>2.0</b>	<b>17.</b>	<b>0.1</b>	<b>0.1</b>	<i>b.d.</i>		<b>99.</b>	<i>b.d.</i>
OBR-8-4136	39.	13.	9.6	1.9	3.8	8.1	1.8	0.4	0.5	0.2	20.	3.4	16.	1.8	0.1	1.7		99.	3.2
OBR-8-A	<b>21.</b>	<b>4.9</b>	<b>41.</b>	<b>0.4</b>	<b>2.1</b>	<b>0.4</b>	<b>0.3</b>	<b>0.2</b>	<b>0.5</b>	<b>0.1</b>	<b>27.</b>	<b>0.4</b>	<b>26.</b>	<b>6.3</b>	<b>0.1</b>	<b>6.2</b>		<b>99.</b>	<i>b.d.</i>
OBR-8-B	63.	10.	0.8	0.1	1.6	9.7	1.3	0.9	0.1	0.2	8.2	1.8	6.4	0.1	0.1	<i>b.d.</i>	267	97.	11.
OBR-9-3884	26.	11.	15.	1.5	2.8	7.9	1.5	0.3	0.4	0.2	30.	2.8	27.	5.4	0.6	4.8	224	98.	5.7
OBR-10-164	20.	14.	6.5	1.4	5.1	17.	1.9	<i>b.d.</i>	0.3	1.2	31.	7.4	23.	2.3	0.1	2.1		99.	<i>b.d.</i>
OBR-11-1.2	6.9	1.5	22.	1.5	2.9	29.	0.1	0.2	0.0	0.1	34.			9.7	0.2	9.4		99.	3.9
OBR-11-1.2P <sup>d</sup>	-	-	-	-	-	-	-	-	-	-	-	-	-	-	0.1	-	681	-	-
OBR-11-1.8	8.0	4.0	11.	4.2	2.2	36.	0.5	0.6	0.1	0.2	33.			7.7	0.2	7.4		100	11.
OBR-11-1.8P	-	-	-	-	-	-	-	-	-	-	-	-	-	-	0.2	-	877	-	-
OBR-11-2.8	3.8	3.8	3.9	6.7	1.7	45.	0.6	0.8	0.1	0.2	32.			7.5	0.2	7.3		99.	8.0
OBR-11-3.8	23.	7.5	3.0	11.	1.6	17.	0.9	1.5	0.3	0.2	32.			6.1	0.3	5.8		99.	12.
OBR-11-3.8P	-	-	-	-	-	-	-	-	-	-	-	-	-	-	0.2	-	819	-	-
OBR-11-4.4	2.1	4.1	2.8	7.5	1.5	43.	0.4	1.0	0.1	0.4	37.			7.7	0.3	7.3		100	<i>b.d.</i>
OBR-11-4.4P	-	-	-	-	-	-	-	-	-	-	-	-	-	-	0.1	-	124	-	-
OBR-11-5.1	15.	5.5	2.9	8.1	1.3	32.	0.7	1.2	0.2	0.1	32.			6.9	0.3	6.6	211	100	<i>b.d.</i>
OBR-11-5.1P	-	-	-	-	-	-	-	-	-	-	-	-	-	-	0.1	-	150	-	-
OBR-11-5.7	16.	4.7	1.6	9.5	0.4	24.	0.3	1.2	0.2	0.0	40.			2.3	-	-		100	<i>b.d.</i>
OBR-11-6.1	-	-	-	-	-	-	-	-	-	-	-	-	-	-	0.4	-	102	-	-
OBR-11-6.1P <sup>e</sup>	18.	4.6	1.9	9.1	0.7	21.	0.4	1.4	0.2	0.3	40.			3.8	-	-		99.	<i>b.d.</i>
OBR-11-6.1P	-	-	-	-	-	-	-	-	-	-	-	-	-	-	0.2	-	200	99.	<i>b.d.</i>
OBR-11-6.1P	-	4	8	2	9	5	1	7	1	2	-	-	-	-	3	-	00	5	1.

<sup>a</sup> In bold italic, samples from the host strata; in regular, samples from the Mn-ore layer.

<sup>b</sup> Elemental analyser data.

<sup>c</sup> Below detection limit.

<sup>d</sup> Pisolith.

<sup>e</sup> Matrix.

1521  
1522  
1523  
1524  
1525  
1526

1527  
1528

**Table 4**

Chemical composition (ICP-MS) of the investigated samples.

Sample ID <sup>a</sup>	OBR-11-1.2								OBR-11-1.8								OBR-11-2.8							
	bu	leachat	residu	% in the	pisolith	pisolith	% in the	bul	leachat	residu	% in the	pisolith	pisolith	% in the	bu	leachat	residu	% in the						
Element	lk	e	e	leachate	e	leachate	leachate	k	e	ue	leachate	e	h	in	lk	e	ue	leachate						
Al, wt.%		0.77	1.38	35.8	0.60	0.75	44.2		1.20	2.05	36.9	0.94	1.27	42.4		1.26	1.38	47.7						
Ca		8.32	1.91	81.3	19.5	1.93	91.0		8.04	1.14	87.6	9.52	1.27	88.2		3.11	0.29	91.5						
Mg		0.43	0.26	61.8	0.40	0.09	81.2		1.23	0.61	66.7	0.72	0.27	73.1		1.88	0.34	84.5						
Fe		1.09	0.93	54.0	0.97	0.36	73.2		1.12	0.91	55.0	0.69	0.51	57.7		0.76	0.57	56.9						
Mn		21.6	4.95	81.4	16.0	1.13	93.4		17.9	2.34	88.4	22.6	1.95	92.1		25.5	1.86	93.2						
Na		0.20	0.12	61.8	0.13	0.09	59.4		0.42	0.15	73.7	0.25	0.12	67.2		0.43	0.13	76.3						
K		0.03	0.14	17.4	0.02	0.05	30.0		0.09	0.30	22.6	0.05	0.12	29.8		0.07	0.21	24.7						
P		0.07	0.02	78.3	0.04	0.004	90.5		0.09	0.02	85.0	0.08	0.01	90.9		0.08	0.01	91.0						
Li, ppm	13.	5.73	8.70	39.7	3.07	2.13	59.1	88.	40.8	55.2	42.5	20.6	19.8	51.0	34.	20.7	14.4	58.9						

	6						3						0					
	1.7						3.6						2.6					
Sc	9	0.23	1.04	17.9	0.11	0.24	30.8	8	1.10	2.15	33.8	0.37	0.78	32.4	8	0.80	1.28	38.5
	69							11							89			
Ti	3	105	437	19.4	81.3	164	33.1	25	176	768	18.6	132	359	26.8	4	201	513	28.1
	70.							20							49.			
V	7	22.1	56	28.4	13.0	1.76	88.1	0	88.3	95.3	48.1	42.6	13.9	75.4	8	42.2	9.31	81.9
	13.							26.							18.			
Cr	3	4.33	10.9	28.4	3.02	3.31	47.7	8	9.46	17.0	35.7	5.62	6.44	46.6	4	9.06	10.6	46.0
	13.							36.							26.			
Co	3	7.94	3.54	69.2	4.73	1.77	72.8	1	26.6	7.98	76.9	20.5	4.78	81.1	8	20.1	4.81	80.7
	29.							11							60.			
Ni	1	20.9	11.2	65.2	15.7	6.37	71.1	8	84.2	37.5	69.2	63.0	21.3	74.8	8	46.6	16.6	73.7
	12.							23.							13.			
Cu	6	8.20	8.04	50.5	7.11	2.88	71.2	1	15.3	12.2	55.6	13.0	7.41	63.7	3	10.2	7.63	57.2
								30.							16.			
Zn		10.0	8.27	54.8	10.2	4.34	70.2	8	28.8	13.0	68.9	19.0	7.76	71.0	7	22.7	9.36	70.9
	2.4							4.9							3.7			
Ga	9	0.62	2.16	22.4	0.47	0.79	37.2	5	1.38	3.66	27.4	0.84	1.75	32.4	4	1.46	2.42	37.6
	13.							27.							20.			
Rb	4	2.12	10.4	16.9	0.92	2.99	23.5	1	4.64	20.1	18.7	2.72	8.38	24.5	4	3.93	14.5	21.4
	19							21							10			
Sr	6	147	42.4	77.6	296	34.3	89.6	3	174	32.3	84.3	194	32.0	85.9	2	86.8	15.3	85.0
	12.							15.							14.			
Y	6	8.97	2.66	77.1	5.34	0.49	91.7	2	11.3	2.85	79.8	8.72	1.57	84.7	4	10.8	1.68	86.5
	11.							26.							20.			
Zr	4	1.06	10.4	9.3	0.84	3.77	18.2	4	2.85	20.8	12.1	1.43	9.14	13.5	7	2.22	15.3	12.6
	1.3							2.6							1.9			
Nb	4	0.06	1.27	4.7	0.04	0.37	10.0	4	0.07	2.64	2.5	0.05	1.00	4.7	7	0.04	1.90	2.3
	0.8							1.7							1.2			
Cs	6	0.13	0.68	15.7	0.06	0.19	23.8	0	0.22	1.34	14.0	0.13	0.56	19.3	5	0.20	0.92	17.6
	22							23							17			
Ba	2	146	53.7	73.1	183	23.1	88.8	7	156	54.9	74.0	177	37.0	82.7	2	111	33.9	76.7
	10.							15.							11.			
La	5	7.42	2.92	71.8	3.30	0.77	81.0	3	11.3	3.92	74.3	7.14	1.86	79.3	5	8.08	2.31	77.8
	14.							20.							15.			
Ce	2	11.1	4.77	69.9	4.67	1.18	79.9	5	15.3	6.47	70.3	10.1	2.33	81.3	5	11.6	3.59	76.4
	2.0							3.0							2.5			
Pr	8	1.26	0.55	69.7	0.56	0.16	77.4	8	2.05	0.82	71.6	1.33	0.38	77.7	0	1.54	0.48	76.3
	8.4							12.							10.			
Nd	5	5.14	2.09	71.1	2.42	0.63	79.3	3	8.48	3.16	72.9	5.42	1.45	78.9	1	6.47	1.81	78.2
	1.8							2.6							2.2			
Sm	7	1.04	0.38	73.0	0.48	0.11	81.0	2	1.69	0.56	75.0	1.13	0.26	81.1	1	1.30	0.33	79.9
	0.4							0.6							0.5			
Eu	8	0.26	0.09	74.7	0.15	0.02	86.0	3	0.40	0.12	77.4	0.29	0.06	82.3	3	0.32	0.07	82.1
	1.9							2.7							2.3			
Gd	8	1.19	0.37	76.2	0.61	0.11	85.3	3	1.83	0.51	78.3	1.20	0.25	82.6	1	1.44	0.27	84.1
	0.3							0.4							0.3			
Tb	1	0.19	0.06	75.7	0.10	0.02	86.3	2	0.28	0.08	78.5	0.20	0.04	82.9	6	0.23	0.05	83.0
	1.8							2.4							2.1			
Dy	9	1.14	0.38	75.0	0.64	0.11	85.9	1	1.57	0.46	77.5	1.18	0.26	82.0	4	1.36	0.26	83.9
	0.4							0.5							0.4			
Ho	1	0.25	0.08	75.6	0.14	0.02	86.5	0	0.33	0.10	76.7	0.24	0.05	81.8	5	0.30	0.06	83.3
	1.2							1.4							1.3			
Er	1	0.75	0.26	74.0	0.42	0.07	85.4	3	0.92	0.30	75.4	0.71	0.18	80.2	3	0.85	0.20	81.0
	0.1							0.2							0.2			
Tm	8	0.11	0.04	73.2	0.06	0.01	84.3	1	0.13	0.05	73.7	0.10	0.03	78.6	0	0.13	0.03	80.4
	1.0							1.2							1.2			
Yb	7	0.61	0.24	71.6	0.34	0.07	83.9	8	0.73	0.29	71.6	0.61	0.18	77.5	2	0.72	0.21	77.3
	0.1							0.1							0.1			
Lu	7	0.09	0.04	70.0	0.05	0.01	86.1	9	0.10	0.04	69.8	0.09	0.02	78.0	9	0.11	0.03	76.9
	44.							63.							50.			
ΣREE	8	30.5	12.3		14.0	3.29		7	45.1	16.9		29.7	7.36		6	34.5	9.69	
(Ce/Ce*)	0.7							0.6							0.6			
<sup>b</sup>	0	0.81	0.86		0.77	0.77		9	0.72	0.84		0.75	0.64		7	0.76	0.80	
(Eu/Eu*)	0.7							0.7							0.7			
<sup>c</sup>	6	0.73	0.71		0.85	0.68		1	0.69	0.65		0.75	0.72		1	0.70	0.69	
La <sub>CN</sub> /Lu <sub>CN</sub>	6.6							8.6							6.5			
<sup>CN</sup>	3	8.84	8.13		6.79	9.87		6	11.9	9.52		8.72	8.05		9	7.89	7.48	
	0.2							0.6							0.4			
Hf	2	0.04	0.28	12.0	0.03	0.10	20.2	0	0.07	0.55	11.4	0.05	0.24	16.5	4	0.05	0.40	10.8
	0.0							0.1							0.1			
Ta	7	0.00	0.08	2.0	0.001	0.02	6.4	7	0.001	0.16	0.4	0.001	0.04	2.5	0	0.001	0.09	0.6
	2.3							6.1							3.3			
Pb	7	2.30	0.69	76.9	9.42	0.29	97.0	4	5.95	0.40	93.7	5.30	0.29	94.8	3	5.29	0.30	94.6
	0.9							2.5							1.9			
Th	5	0.58	0.52	52.4	0.20	0.17	54.5	5	1.54	0.98	60.9	0.79	0.42	65.1	6	1.09	0.66	62.3
	3.2							3.7							1.9			
U	5	2.58	0.84	75.5	2.31	0.30	88.4	4	3.13	0.84	78.9	1.66	0.37	81.9	3	1.51	0.43	77.7

1530  
1531  
1532  
1533  
1534  
1535  
1536  
1537  
1538<sup>b</sup> Ce/Ce\* = 2Ce<sub>CN</sub> / (La<sub>CN</sub> + Pr<sub>CN</sub>)<sup>c</sup> Eu/Eu\* = 2Eu<sub>CN</sub> / (Sm<sub>CN</sub> + Gd<sub>CN</sub>)

Table 4 (continued)

Sample ID	OBR-11-3.8						OBR-11-4.4								
	Element	bulk	leachate	residue	% in the leachate	pisolith leachate	pisolith residue	% in the leachate	bulk	leachate	residue	% in the leachate	pisolith leachate	pisolith residue	% in the leachate
Al, wt.%		1.48	1.61		47.9	1.45	1.58	47.9		1.18	1.25	48.5	0.85	0.80	51.5
Ca		2.80	0.32		89.9	3.32	0.22	93.8		2.40	0.12	95.1	2.81	0.18	93.9
Mg		2.31	0.50		82.2	2.36	0.42	84.9		1.40	0.26	84.3	0.88	0.23	79.5
Fe		0.82	0.68		54.4	0.82	0.67	54.8		0.53	0.51	50.7	0.33	0.33	50.4
Mn		20.7	1.89		91.6	23.1	1.20	95.1		28.8	1.28	95.8	32.8	1.45	95.8
Na		0.57	0.16		78.2	0.58	0.14	80.7		0.43	0.12	77.7	0.24	0.10	70.1
K		0.10	0.30		25.3	0.09	0.29	22.7		0.06	0.17	26.1	0.03	0.04	39.6
P		0.09	0.01		88.5	0.09	0.01	91.1		0.06	0.01	89.9	0.09	0.005	94.6
Li, ppm	40.9	23.9	18.1		56.9	23.3	19.0	55.2	22.3	13.8	9.28	59.7	7.10	2.50	74.0
Sc	3.58	1.06	1.76		37.6	0.94	1.97	32.2	2.12	0.51	0.99	34.1	0.10	0.11	48.0
Ti	1143	226	656		25.7	228	705	24.5	741	188	397	32.1	125	147	46.1
V	214	133	35.1		79.1	118	31.5	79.0	118	152	34.3	81.5	75.2	2.11	97.3
Cr	26.9	11.7	13.3		47.0	11.3	14.7	43.4	15.0	8.11	9.72	45.5	2.91	2.52	53.5
Co	41.3	27.5	9.15		75.1	25.7	10.4	71.1	33.3	21.1	9.26	69.5	8.45	8.13	51.0
Ni	118	82.9	32.2		72.0	85.3	35.5	70.6	70.2	46.2	21.2	68.6	24.4	27.4	47.1
Cu	27.2	13.9	15.0		48.1	13.4	15.8	45.8	18.3	11.0	10.9	50.1	4.97	6.66	42.7
Zn	30.9	26.9	12.3		68.5	27.2	12.3	68.8	9.48	18.6	8.77	67.9	10.4	5.07	67.3
Ga	4.90	1.47	3.27		31.0	1.50	3.50	30.0	2.98	1.13	2.10	35.1	0.67	0.78	46.3
Rb	29.5	5.00	21.2		19.1	4.28	23.1	15.7	17.3	3.09	12.4	19.9	1.17	2.95	28.4
Sr	112	87.2	18.9		82.2	92.1	16.3	85.0	87.4	74.8	11.5	86.7	67.9	9.48	87.8
Y	20.9	14.6	2.99		83.0	15.7	2.79	85.0	12.7	9.65	1.03	90.3	10.5	0.57	94.8
Zr	33.4	2.62	20.7		11.2	2.15	23.2	8.5	15.0	1.88	11.2	14.3	1.81	4.31	29.5
Nb	2.78	0.05	2.52		2.0	0.03	2.76	0.9	1.47	0.04	1.42	2.9	0.03	0.33	9.1
Cs	1.85	0.23	1.39		14.5	0.18	1.48	10.8	1.11	0.17	0.79	17.6	0.07	0.19	26.9
Ba	201	117	47.9		71.0	120	46.8	71.9	143	89.3	26.0	77.4	78.9	9.01	89.7
La	16.0	10.8	3.66		74.6	10.9	3.51	75.6	9.41	6.77	1.77	79.3	6.80	0.82	89.3
Ce	21.7	14.6	5.51		72.6	15.6	5.80	73.0	11.0	8.71	2.98	74.5	8.92	1.19	88.2
Pr	3.31	2.02	0.77		72.3	2.12	0.73	74.4	1.99	1.19	0.38	76.1	1.00	0.15	87.3
Nd	13.4	8.55	2.97		74.2	8.83	2.76	76.2	8.21	5.02	1.38	78.5	4.13	0.57	87.9
Sm	2.80	1.72	0.53		76.4	1.83	0.48	79.2	1.83	1.03	0.21	82.8	0.85	0.10	89.2
Eu	0.68	0.42	0.10		80.3	0.44	0.10	81.8	0.44	0.26	0.05	84.6	0.21	0.02	90.9
Gd	3.08	1.97	0.46		81.0	2.07	0.43	82.6	1.93	1.21	0.20	85.7	1.06	0.10	91.7
Tb	0.47	0.31	0.07		80.9	0.33	0.07	82.1	0.31	0.19	0.03	85.2	0.18	0.02	91.0
Dy	2.82	1.87	0.45		80.6	2.00	0.44	81.9	1.88	1.17	0.21	85.0	1.24	0.11	91.5
Ho	0.61	0.40	0.10		80.8	0.43	0.10	81.5	0.40	0.26	0.05	84.7	0.28	0.03	91.2
Er	1.79	1.17	0.31		78.8	1.26	0.30	80.6	1.16	0.75	0.14	84.0	0.84	0.09	90.6
Tm	0.27	0.18	0.05		77.7	0.19	0.05	78.5	0.18	0.10	0.02	81.0	0.14	0.01	90.6
Yb	1.65	1.02	0.33		75.5	1.13	0.33	77.5	1.07	0.64	0.15	80.7	0.80	0.08	90.7
Lu	0.25	0.15	0.05		75.4	0.17	0.05	77.2	0.17	0.09	0.03	78.9	0.12	0.01	90.4
ΣREE	68.8	45.2	15.4		47.3	15.2	47.3	40.0	40.0	27.4	7.60	26.6	26.6	3.30	
Ce/Ce*	0.69	0.72	0.76		0.75	0.84	0.60	0.69	0.85	0.74	0.78	0.74	0.78		
Eu/Eu*	0.71	0.69	0.62		0.68	0.63	0.72	0.70	0.68	0.66	0.62	0.66	0.62		
La <sub>CN</sub> /Lu <sub>CN</sub>	6.96	7.61	7.91		6.93	7.57	6.02	7.70	7.53	6.00	6.77	6.00	6.77		
Hf	0.77	0.06	0.54		9.8	0.05	0.63	7.4	0.30	0.04	0.31	12.5	0.04	0.12	24.4
Ta	0.19	0.001	0.13		0.9	0.001	0.15	0.8	0.06	0.001	0.07	0.8	0.001	0.01	4.9
Pb	7.45	5.69	0.35		94.3	11.3	0.72	94.0	1.96	3.21	0.47	87.2	2.65	0.33	88.9
Th	2.71	1.40	1.03		57.6	1.44	1.09	57.0	1.48	0.86	0.48	64.5	0.28	0.16	64.2
U	4.08	3.25	0.78		80.6	2.95	0.69	81.0	3.88	3.44	0.49	87.5	1.78	0.19	90.3

1539  
1540  
1541  
1542  
1543  
1544  
1545  
1546  
1547  
1548  
1549

Table 4 (continued)

Sample ID	OBR-11-5.1						OBR-11-5.7			OBR-11-6.1						
	Element	bul k	leachate	residu e	% in the leachate	pisolith leachate	pisolith residue	% in the leachate	bul k	leachate	residu e	% in the leachate	bul k	pisolith bul k	pisolith leachate	pisolith residue
Al, wt.%		1.14	1.29		47.0	1.13	1.04	52.1		2.08	1.43	59.3		1.26	1.05	54.4
Ca		2.08	0.43		82.9	2.35	0.19	92.7		0.93	0.14	86.8		4.46	0.52	89.5
Mg		1.47	0.50		74.7	1.11	0.26	81.1		2.85	1.19	70.6		1.92	0.49	79.7
Fe		0.77	0.93		45.4	0.51	0.61	45.6		0.62	0.81	43.3		0.49	0.64	43.6
Mn		27.8	3.80		88.0	30.4	1.94	94.0		17.3	0.99	94.6		23.8	2.68	89.9
Na		0.42	0.16		72.1	0.38	0.13	75.3		0.82	0.16	83.6		0.47	0.14	76.9

K		0.06	0.20	24.6	0.05	0.09	33.6		0.10	0.23	29.7		0.06	0.11	35.4	
P		0.05	0.01	87.0	0.05	0.01	89.2		0.06	0.01	89.2		1.08	0.12	89.8	
Li, ppm	22.0	13.9	11.8	54.2	8.19	5.94	57.9	28.2	19.8	12.8	60.6	7	23.2	18.4	7.37	71.4
Sc	2.1							2.8				3.1				
	4	0.58	1.23	32.2	0.28	0.49	35.9	3	0.53	2.00	21.0	3	1.62	0.58	0.56	50.6
Ti	112							112				105				
Ti	799	171	480	26.2	162	245	39.8	0	231	790	22.6	2	635	189	323	36.9
V	111	104	16.6	86.2	86.0	6.98	92.5	227	232	26.8	89.7	553	329	306	51.1	85.7
Cr	16.0							17.6				30.9				
	31.0							22.6				65.9				
Co	7	19.1	11.8	61.8	12.9	7.42	63.4	1	17.9	3.86	82.3	5	44.5	32.2	10.3	75.7
Ni	129	79.4	68.7	53.6	53.6	47.1	53.2	107	98.6	24.7	80.0	151	127	79.5	48.8	61.9
Cu	20.6							15.3				36.1				
	5.1	7.82	15.8	33.1	6.68	8.82	43.1	3	8.60	9.82	46.7	1	27.7	11.2	19.7	36.3
Zn	7	16.4	10.0	62.0	12.8	7.82	62.0	4	21.8	12.7	63.3	7	12.7	23.3	7.49	75.7
Ga	3.0							4.7				4.9				
	5	1.07	2.38	31.0	0.82	1.36	37.7	9	2.82	2.47	53.4	7	2.52	1.75	1.49	54.1
Rb	17.6							20.2				23.7				
	77.3							84.2				7				
Sr	3	66.7	20.4	76.6	63.1	11.4	84.7	3	81.4	13.6	85.7	113	399	326	44.6	88.0
Y	14.1							13.4				22.2				
	18.1	11.0	3.15	77.8	9.87	1.05	90.4	4	10.2	2.75	78.8	2	64.9	54.9	6.73	89.1
Zr	6	1.70	14.3	10.6	1.91	7.58	20.1	1	2.21	20.5	9.8	7	14.4	4.17	8.64	32.5
Nb	1.6							2.9				2.7				
	4	0.03	1.75	1.8	0.03	0.81	3.8	3	0.04	3.26	1.2	8	1.13	0.11	1.30	7.8
Cs	1.1							0.9				1.5				
Ba	1	0.16	0.84	15.8	0.09	0.45	16.5	2	0.12	0.75	14.2	6	0.76	0.18	0.52	25.7
	143	85.9	42.3	67.0	77.2	16.9	82.0	191	95.2	84.3	53.0	159	261	192	37.7	83.6
La	9.2							11.5				18.1				
	11.4	6.46	3.32	66.1	5.33	1.70	75.8	5	8.78	2.94	74.9	1	52.5	48.3	6.62	88.0
Ce	6	8.80	4.26	67.4	7.25	2.81	72.1	5	14.2	5.80	71.0	3	62.0	58.2	8.73	87.0
	2.0							2.8				3.4				
Pr	7	1.24	0.70	63.9	0.94	0.36	72.3	1	1.86	0.78	70.5	2	7.17	6.23	0.96	86.6
Nd	8.6							11.3				13.9				
	3	5.22	2.68	66.1	3.95	1.37	74.2	2	7.33	3.13	70.0	9	28.9	25.8	3.89	86.9
Sm	1.9							2.4				2.8				
	6	1.11	0.49	69.5	0.82	0.25	76.8	3	1.48	0.67	68.7	8	5.69	5.03	0.72	87.5
Eu	0.4							0.5				0.6				
	9	0.27	0.11	71.9	0.21	0.04	85.2	5	0.32	0.12	73.1	8	1.41	1.19	0.16	87.9
Gd	2.0							2.4				3.2				
	8	1.33	0.47	74.0	1.00	0.21	82.7	6	1.49	0.55	73.1	6	7.28	6.28	0.84	88.1
Tb	0.3							0.3				0.4				
	5	0.22	0.07	75.8	0.18	0.03	84.9	8	0.24	0.09	73.4	9	1.12	0.97	0.13	88.5
Dy	2.1							2.1				2.9				
	3	1.39	0.45	75.3	1.20	0.20	85.5	7	1.37	0.51	72.9	3	6.98	6.13	0.83	88.0
Ho	0.4							0.4				0.6				
	6	0.31	0.10	76.0	0.28	0.04	86.7	6	0.29	0.10	74.0	2	1.54	1.37	0.18	88.3
Er	1.4							1.3				1.8				
	0	0.95	0.32	74.7	0.89	0.14	86.7	4	0.85	0.31	73.5	1	4.48	4.02	0.55	88.0
Tm	0.2							0.2				0.2				
	1	0.14	0.05	74.3	0.14	0.02	86.5	1	0.13	0.05	73.4	6	0.62	0.58	0.08	88.1
Yb	1.3							1.2				1.5				
	0	0.83	0.33	71.8	0.83	0.14	86.0	4	0.77	0.29	72.9	6	3.83	3.31	0.48	87.4
Lu	0.2							0.2				0.2				
	0	0.12	0.05	71.1	0.12	0.02	86.1	0	0.12	0.04	73.2	3	0.54	0.47	0.07	86.9
ΣREE	42.1							55.5				75.5				
	0.6	28.4	13.4		23.1	7.32		0.7	39.2	15.4		0.7	184	168	24.2	
Ce/Ce*	2	0.71	0.65		0.73	0.84		7	0.82	0.92		4	0.68	0.71	0.75	
Eu/Eu*	0.7							0.6				0.6				
	4	0.68	0.67		0.70	0.47		8	0.65	0.58		8	0.67	0.65	0.64	
La <sub>CN</sub> /Lu <sub>CN</sub>	4.9							6.3				8.2				
	4	5.74	7.27		4.59	9.05		3	8.02	7.33		5	10.4	10.9	9.89	
Hf	0.4							0.6				0.6				
	1	0.04	0.39	8.9	0.04	0.20	16.2	2	0.05	0.62	7.8	8	0.30	0.09	0.25	26.5
Ta	0.1							0.1				0.3				
	0	0.001	0.08	1.3	0.001	0.05	2.1	9	0.001	0.20	0.6	1	0.06	0.005	0.09	4.8
Pb	2.7							10.7				9.3				
	5	2.85	0.30	90.6	3.14	0.45	87.4	7	12.0	0.39	96.8	1	6.06	5.22	1.66	75.9
Th	1.5							4.6				2.4				
	1	0.88	0.74	54.2	0.47	0.52	47.4	6	3.83	1.00	79.3	4	1.43	0.85	0.46	64.6
U	3.9							2.8				10.1				
	2	3.24	1.12	74.3	2.17	0.37	85.5	5	2.96	0.42	87.7	9	10.5	9.88	1.31	88.3

1551  
1552  
1553  
1554  
1555  
1556  
1557  
1558  
1559  
1560

Table 4 (continued)

Sample ID	OBR-5-1263	OBR-5-1264	OBR-5-1265	OBR-5-1266	OBR-5-1267	OBR-5-1302	OBR-8-A
Element	leachate residue %	leachate residue %	leachate residue %	leachate residue %	leachate residue %	leachate residue %	leachate residue %
wt. %	0.92	0.97	0.8	0.9	0.9	0.8	0.7
Ca	8.78	0.20	5	9	4	2	3
Mg	0.83	0.22	8	3	1	0	4
Fe	1.37	1.48	5	6	9	6	9
Mn	25.8	0.28	5	0	4	7	3
Na	0.48	0.45	2	2	3	8	9
K	0.07	0.12	6	7	5	8	3
P	0.33	0.03	2	9	7	1	2
Li, ppm	17.0	8.08	1	0	0	7	7
Sc	0.54	3.62	9	3	5	2	1
Ti	106	102	25	2.2	103	8	7
V	51.4	10.5	2	6.5	2	9	7
Cr	5.32	7.36	2	6.7	6	7	9
Co	14.5	10.7	7	7	6	3	7
Ni	87.8	26.9	9	5	7	4	3
Cu	45.6	21.8	4	1	1	4	1
Zn	34.4	46.7	5	3	7	5	1
Ga	1.00	1.31	9	6.2	8	1	9
Rb	3.44	7.50	9	2	3	4	7
Sr	360	62.1	6	5	234	3	2
Y	14.6	15.4	4	8	9	2	2
Zr	2.00	3.21	9	2.9	4	4	9
Nb	0.05	0.04	0	0.3	5	3	3
Cs	0.14	0.36	8	2	9	6	7
Ba	632	61.4	7	8	3	6	3
La	12.4	15.7	7	4	2	1	9
Ce	17.6	35.5	5	3	8	0	5
Pr	2.14	4.41	0	8	0	3	7
Nd	8.98	18.2	9	7	7	8	4
Sm	1.81	3.92	5	7	8	1	7
Eu	0.51	0.84	2	3	6	1	9
Gd	2.06	3.60	9	2	6	7	1

Tb	0.31	0.0	79.	0.0	87.	0.2	0.0	86.	0.3	0.0	83.	0.3	0.1	79.	0.4	0.0	89.	0.0	0.0	60.	
		8	7	0.55	8	9	6	4	2	7	1	9	0	9	3	5	8	6	4	2	
		0.4	81.	0.4	86.	1.4	0.2	85.	1.8	0.3	82.	2.1	0.5	78.	2.4	0.2	89.	0.3	0.2	57.	
Dy	1.87	3	2	3.00	9	0	5	4	8	1	9	4	9	9	6	8	8	2	3	9	
		0.0	81.	0.1	83.	0.3	0.0	85.	0.3	0.0	82.	0.4	0.1	79.	0.5	0.0	90.	0.0	0.0	58.	
Ho	0.39	9	5	0.54	1	1	0	5	2	8	8	3	4	2	0	1	5	4	7	7	
		0.2	80.	0.3	79.	0.8	0.1	84.	1.0	0.2	81.	1.1	0.3	76.	1.4	0.1	89.	0.1	0.1	53.	
Er	1.14	8	3	1.46	7	7	5	5	7	8	5	3	9	6	9	7	8	3	7	8	
		0.0	79.	0.0	74.	0.1	0.0	83.	0.1	0.0	79.	0.1	0.0	74.	0.2	0.0	88.	0.0	0.0	49.	
Tm	0.16	4	7	0.20	7	9	2	2	8	5	4	2	6	6	2	1	3	9	2	0	
		0.2	77.	0.4	71.	0.7	0.1	83.	0.8	0.2	76.	0.9	0.3	72.	1.2	0.1	87.	0.1	0.1	46.	
Yb	0.93	7	5	1.18	7	4	0	4	3	3	5	9	1	5	0	0	7	5	4	1	
		0.0	75.	0.0	69.	0.1	0.0	79.	0.1	0.0	77.	0.1	0.0	70.	0.1	0.0	86.	0.0	0.0	44.	
Lu	0.13	4	7	0.17	7	2	0	3	9	2	4	1	3	6	5	7	3	4	2	7	
		17.		12.		43.	9.2		48.	15.		59.	20.		58.	13.		9.1	8.7		
ΣREE	50.4	9		89.2	5		1	7		5	9		4	6		6	4		2	8	
		0.8		1.5		0.8	0.9		0.8	0.9		0.8	0.9		0.8	0.9		0.6	0.9		
Ce/Ce*	0.77	6		1.03	0		2	0		5	2		3	1		8	5		1	1	
		0.6		0.8		0.6	1.1		0.6	0.8		0.6	1.0		0.6	1.0		0.5	1.0		
Eu/Eu*	0.81	0		0.67	7		7	9		6	4		5	2		5	6		9	6	
La <sub>CN</sub> /Lu <sub>CN</sub>	10.	8		9.98	9		0	2		7	9		3	7		1	2		1	7	
		0.5		3.0		0.0	0.3		12.	0.0	0.6		0.0	0.8		0.0	0.6		0.0	0.4	
Hf	0.05	1	9.1	0.13	2	4.2	5	4	9	7	6	9.8	8	5	8.4	4	2	6.3	2	0	4.7
		0.1		0.8		0.0	0.1		0.0	0.1		0.0	0.3		0.0	0.1		0.0	0.1		
Ta	0.001	7	0.7	0.001	5	0.1	01	1	0.9	01	8	0.4	01	1	0.3	02	6	1.1	01	4	0.4
		1.4	86.	8.3	69.	4.9	5.3	48.	6.5	4.4	59.	6.3	7.7	45.	3.9	4.4	47.	4.7	3.7	55.	
Pb	9.75	9	7	19.0	0	5	8	5	2	0	8	2	7	2	2	1	1	0	0	5	7
		0.8	54.	1.9	74.	0.9	0.4	68.	1.3	0.7	63.	2.0	1.0	65.	1.6	0.7	68.	0.1	1.2	10.	
Th	1.03	7	2	5.67	5	5	0	2	0	6	9	2	1	6	4	4	9	5	4	6	
		0.5	79.	1.4	41.	1.0	0.3	75.	1.7	0.5	76.	2.5	0.8	75.	1.6	0.4	78.	0.8	0.4	68.	
U	1.98	0	7	1.00	2	2	6	4	7	0	2	7	7	2	9	8	5	7	7	0	6

1561

1562

1563

1564

Table 5

Isotope composition of the investigated samples.

Sample ID <sup>a</sup>	Sample type	$\delta^{13}\text{C}_{\text{PDB}}$ (‰)	$\delta^{18}\text{O}_{\text{PDB}}$ (‰)	$\delta^{56/54}\text{Fe}_{\text{IRMM14}}$ (‰)	$^{87}\text{Sr}/^{86}\text{Sr}$	$^{143}\text{Nd}/^{144}\text{Nd}$	$\epsilon\text{Nd}$	$^{206}\text{Pb}/^{204}\text{Pb}$	$^{207}\text{Pb}/^{204}\text{Pb}$	$^{208}\text{Pb}/^{204}\text{Pb}$
<b>OBR-1-3270</b>	<b>bulk</b>	<b>2.04</b>	<b>-1.50</b>	-	-	-	-	-	-	-
OBR-2-1601	bulk	0.12	-0.53	-	-	-	-	-	-	-
OBR-3-1622	bulk	-2.76	-1.50	-	-	-	-	-	-	-
<b>OBR-5-1261</b>	<b>bulk</b>	-	-	-	-	-	-	-	-	-
OBR-5-1262	bulk	-	-	0.24	-	-	-	-	-	-
OBR-5-1263	bulk	-0.13	-1.13	-0.25	-	-	-	-	-	-
OBR-5-1263	leachate	-	-	-	0.70791	0.512296	-6.7	18.553	15.632	38.415
OBR-5-1264	bulk	-	-	0.16	-	-	-	-	-	-
OBR-5-1264	leachate	-	-	-	0.70837	0.512289	-6.8	18.337	15.596	38.318
OBR-5-1264	residue	-	-	-	0.72038	0.512193	-8.7	18.668	15.614	38.680
OBR-5-1265	bulk	-9.02	-1.57	-0.19	-	-	-	-	-	-
OBR-5-1265	leachate	-	-	-	0.70788	0.512277	-7.0	18.868	15.660	38.669
OBR-5-1266	bulk	-8.42	-1.02	-0.06	-	-	-	-	-	-
OBR-5-1266	leachate	-	-	-	0.70794	0.512291	-6.8	19.253	15.706	38.896
OBR-5-1267	bulk	-5.81	-3.23	0.04	-	-	-	-	-	-
OBR-5-1267	leachate	-	-	-	0.70795	0.512285	-6.9	19.339	15.709	38.940
OBR-5-1267	bulk	-9.01	0.02	-0.33	-	-	-	-	-	-

1302										
OBR-5-1302	leachate	-	-	-	0.70796	0.512260	-7.4	18.823	15.654	38.659
OBR-5-1302	residue	-	-	-	0.71336	0.512018	-	18.697	15.648	38.762
OBR-6-3186	bulk	-1.86	-6.13	-	-	-	-	-	-	-
OBR-7-3205	bulk	-1.28	-3.69	-	-	-	-	-	-	-
OBR-7-4130	bulk	-0.24	-7.31	-	-	-	-	-	-	-
<b>OBR-7-4131</b>	<b>bulk</b>	<b>0.45</b>	<b>-4.62</b>	-	-	-	-	-	-	-
<b>OBR-8-3193</b>	<b>bulk</b>	<b>-0.96</b>	<b>-3.19</b>	-	-	-	-	-	-	-
OBR-8-4136	bulk	-2.39	-6.08	-	-	-	-	-	-	-
<b>OBR-8-A</b>	<b>bulk</b>	<b>-4.26</b>	<b>-9.19</b>	-	-	-	-	-	-	-
<b>OBR-8-A</b>	<b>leachate</b>	-	-	-	-	<b>0.512281</b>	<b>-7.0</b>	<b>18.262</b>	<b>15.597</b>	<b>38.039</b>
OBR-8-B	bulk	-10.5	-12.2	-	-	-	-	-	-	-
OBR-9-3884	bulk	-1.79	-2.32	-	-	-	-	-	-	-
OBR-10-164	bulk	-0.60	-2.17	-	-	-	-	-	-	-
OBR-11-1.2	bulk	-0.60	-2.17	-0.12	0.70826	0.512297	-6.7	-	-	-
OBR-11-1.2	leachate	-	-	-	0.70791	0.512319	-6.2	-	-	-
OBR-11-1.2	residue	-	-	-	0.70967	0.512265	-7.3	18.534	15.622	38.405
OBR-11-1.2p	pisolith separate, bulk	3.60	-2.77	-0.35	-	-	-	-	-	-
OBR-11-1.2p	pisolith separate, leachate	-	-	-	0.70788	0.512324	-6.1	18.420	15.605	38.258
OBR-11-1.8	bulk	2.10	-2.31	0.16	0.70861	0.512233	-7.9	18.862	15.649	38.956
OBR-11-1.8	leachate	-	-	-	0.70789	0.512297	-6.7	18.794	15.654	38.703
OBR-11-1.8p	pisolith separate, bulk	-1.54	-2.12	0.13	-	-	-	-	-	-
OBR-11-1.8p	pisolith separate, leachate	-	-	-	0.70787	0.512288	-6.8	18.721	15.641	38.609
OBR-11-2.8	bulk	-0.80	-0.81	-0.15	0.70901	0.512279	-7.0	18.833	15.646	38.756
OBR-11-2.8	leachate	-	-	-	0.70812	0.512329	-6.0	18.785	15.653	38.690
OBR-11-3.8	bulk	0.82	-1.07	0.00	0.70937	0.512279	-7.0	-	-	-
OBR-11-3.8	leachate	-	-	-	0.70798	0.512306	-6.5	-	-	-
OBR-11-3.8p	pisolith separate, bulk	1.20	-1.01	-0.02	-	-	-	-	-	-
OBR-11-3.8p	pisolith separate, leachate	-	-	-	0.70798	0.512304	-6.5	18.459	15.614	38.329
OBR-11-4.4	bulk	-1.02	-1.05	-0.07	0.70902	0.512271	-7.2	18.922	15.662	38.776
OBR-11-4.4	leachate	-	-	-	0.70793	0.512282	-6.9	18.885	15.668	38.723
OBR-11-4.4p	pisolith separate, bulk	-0.66	-1.18	-0.42	-	-	-	-	-	-

OBR-11-4.4p	pisolith separate, leachate bulk	-	-	-	0.70793	0.512317	-6.3	18.889	15.658	38.669
OBR-11-5.1	bulk	-4.91	-2.09	-0.16	0.70917	0.512293	-6.7	18.938	15.662	38.750
OBR-11-5.1	leachate	-	-	-	0.70796	0.512327	-6.1	18.915	15.672	38.728
OBR-11-5.1p	pisolith separate, bulk	-7.43	-2.03	-0.44	-	-	-	-	-	-
OBR-11-5.1p	pisolith separate, leachate bulk	-	-	-	0.70793	0.512314	-6.3	18.846	15.655	38.651
OBR-11-6.1	bulk	-20.3	-3.34	0.08	0.70921	0.512224	-8.1	18.974	15.671	38.788
OBR-11-6.1	leachate	-	-	-	0.70796	0.512282	-6.9	19.017	15.687	38.755
OBR-11-6.1p	pisolith separate, bulk	-24.8	-2.09	-0.24	0.70808	0.512263	-7.3	19.050	15.679	38.777
OBR-11-6.1p	pisolith separate, residue	-	-	-	-	0.512205	-8.4	19.153	15.685	38.873

1565 <sup>a</sup> In bold italic, samples from the host strata; in regular, samples from the Mn-ore layer.

1566

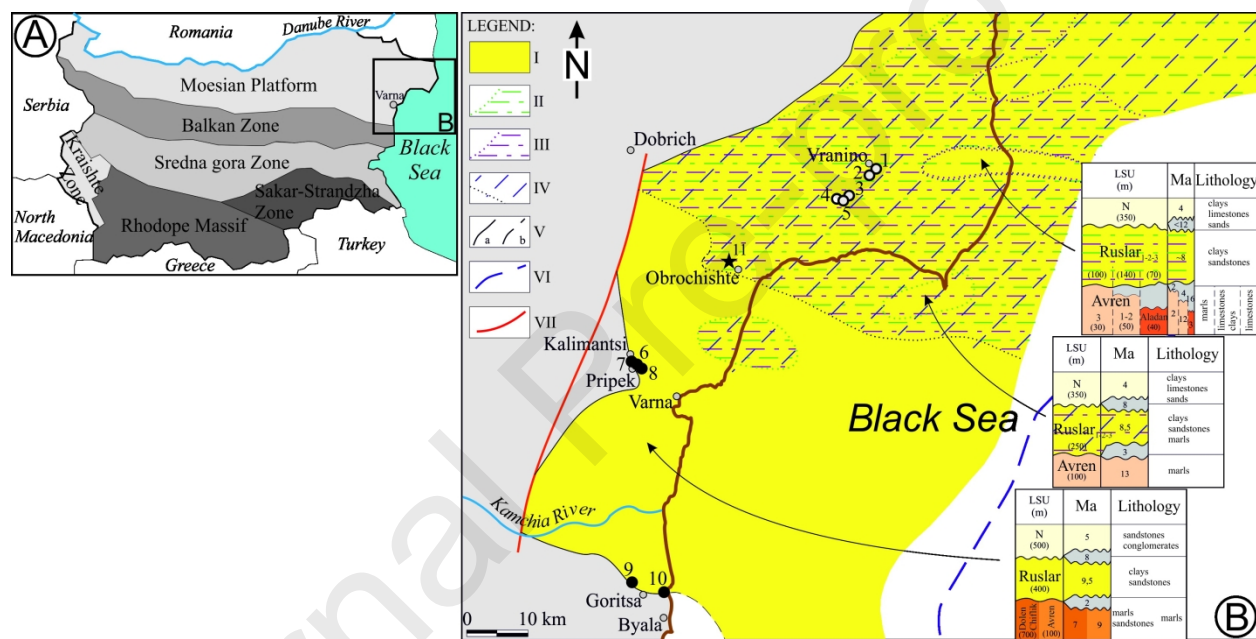
1567 **Table 6**

1568 Geochemistry of Oligocene Mn-deposits around the Black Sea.

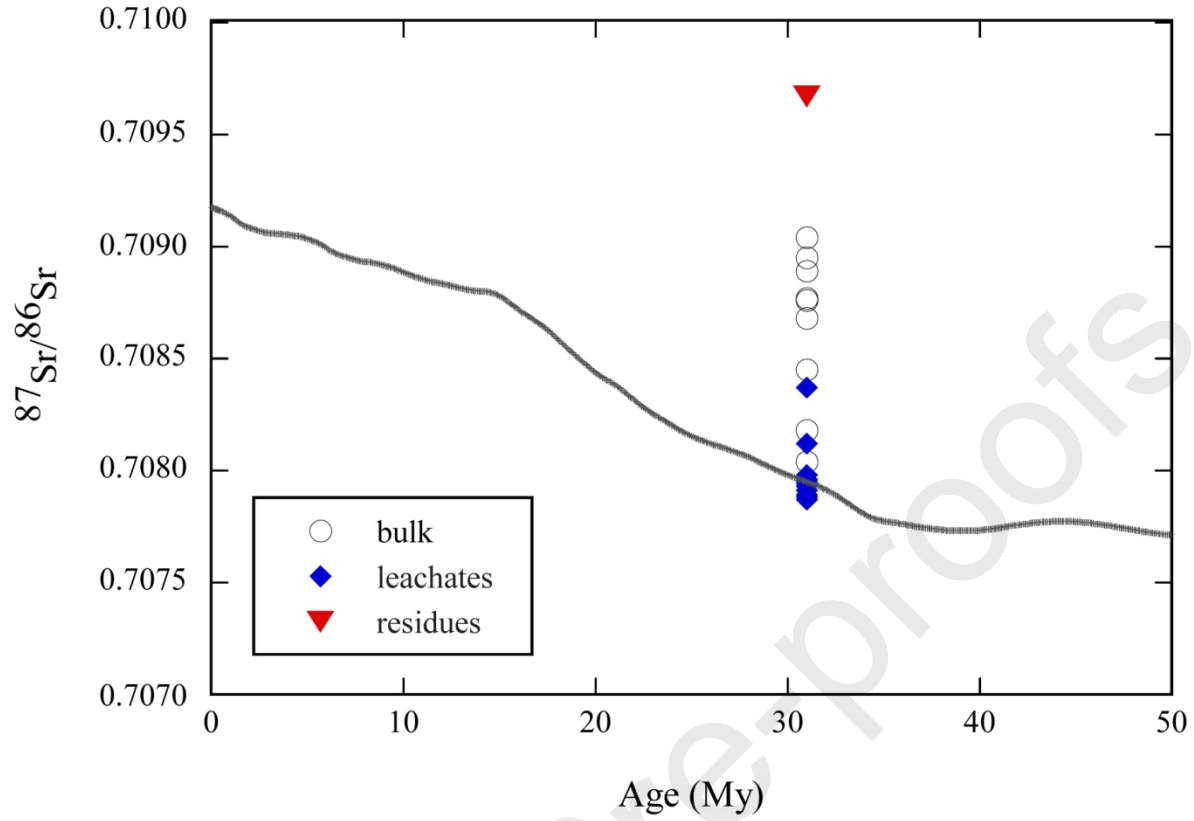
deposit facies	Binkiliç		Chiatura-Kvirila		Labá (Labinsk)	Mangyshlak	
age (Ma)	oxide	carbonate	oxide	carbonate	carbonate	oxide	carbonate
country	Turkey	Turkey	Georgia	Georgia	Russia	Kazakhstan	Kazakhstan
host rock	limestone	limestone	sandstone	sandstone	sand	calcareous sandstone	calcareous sandstone
predominant mineral	ore cryptomelane	rhodochrosite	manganite	rhodochrosite	rhodochrosite	pyrolusite	rhodochrosite
# of analyses	19	11	11	30	24	15	24
MnO (wt.%)	53.5	35.3	48.4	30.6	32.9	39.8	29.2
Fe <sub>2</sub> O <sub>3</sub> tot (wt.%)	2.92	5.92	1.63	3.33	3.88	3.48	2.61
SiO <sub>2</sub> (wt.%)	7.47	8.26	14.7	18.6	-	-	35.5
Al <sub>2</sub> O <sub>3</sub> (wt.%)	2.47	2.27	3.52	3.59	-	-	5.72
CaO (wt.%)	15.1	18.4	5.25	9.56	9.85	-	11.6
MgO (wt.%)	0.94	1.05	1.86	3.07	1.39	-	1.22
K <sub>2</sub> O (wt.%)	0.33	0.49	0.50	0.55	-	-	1.70
Na <sub>2</sub> O (wt.%)	0.43	0.27	0.49	0.55	-	-	1.91
P <sub>2</sub> O <sub>5</sub> (wt.%)	0.74	0.32	0.22	1.14	0.04	0.09	0.48
TiO <sub>2</sub> (wt.%)	0.56	0.38	0.17	0.24	-	-	0.17
LOI (wt.%)	13.4	25.3	16.6	26.8	39.6	-	13.8
Ba (ppm)	4249	5505	9578	785	-	-	-
Co (ppm)	85	72	21	49	13	68	8
Cr (ppm)	15	7	-	-	19	20	21
Cu (ppm)	93	64	24	69	22	60	18
Ni (ppm)	195	203	527	401	151	175	36
Pb (ppm)	46	43	26	22	-	-	-
Sr (ppm)	2232	2719	-	-	-	-	-
V (ppm)	44	91	-	-	37	86	-
Y (ppm)	14	17	-	-	-	-	-
Zn (ppm)	60	57	102	142	53	-	-
Zr (ppm)	53	35	-	-	-	-	-
Ce/Ce*	0.77	0.74	-	-	-	-	-

Eu/Eu*	2.78	1.62	-	-	-	-
Ce/Ce* (at Al=0)	0.80	0.81	-	-	-	-
Eu/Eu* (at Al=0)	3.33	1.78	-	-	-	-
C <sub>carb</sub> (wt.%)	-	-	8.03	18.5	-	5.79
C <sub>org</sub> (wt.%)	-	-	-	-	-	0.29
$\delta^{13}\text{C}_{\text{cct}}^{\text{a}}$ (‰ PDB)	-	-5.10	-7.10	-12.5	-	-5.98
$\delta^{13}\text{C}_{\text{rhod}}^{\text{b}}$ (‰ PDB)	-	-6.61	-10.1	-10.5	-	-10.3
$\delta^{18}\text{O}_{\text{cct}}$ (‰ PDB)	-	-8.05	-7.11	-4.32	-	-2.51
$\delta^{18}\text{O}_{\text{rhod}}$ (‰ PDB)	-	-6.39	-5.32	-4.40	-	-0.99
References	Öztürk and Frakes, 1995; Gültekin, 1998; Gültekin and Balcı, 2018	Varentsov and Rakhmanov, 1980; Dombrovskaya, 1997	Kalinenko et al., 1965	Kuleshov, 2003; 2017		

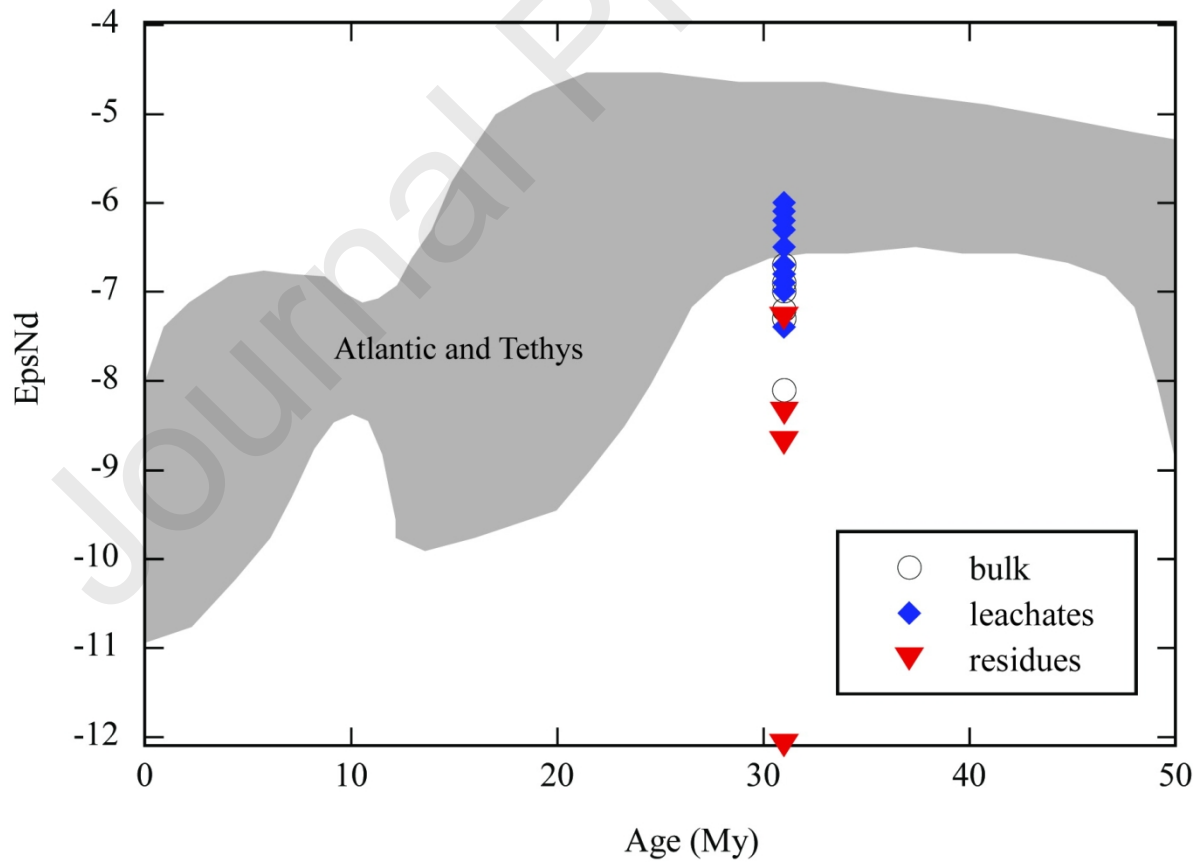
1569 <sup>a</sup>  $\delta^{13}\text{C}_{\text{cct}} = \delta^{13}\text{C}_{\text{calcite}}$  (similarly,  $\delta^{18}\text{O}_{\text{cct}} = \delta^{18}\text{O}_{\text{calcite}}$ )  
 1570 <sup>b</sup>  $\delta^{13}\text{C}_{\text{rhod}} = \delta^{13}\text{C}_{\text{rhodochrosite}}$  (similarly,  $\delta^{18}\text{O}_{\text{rhod}} = \delta^{18}\text{O}_{\text{rhodochrosite}}$ )  
 1571



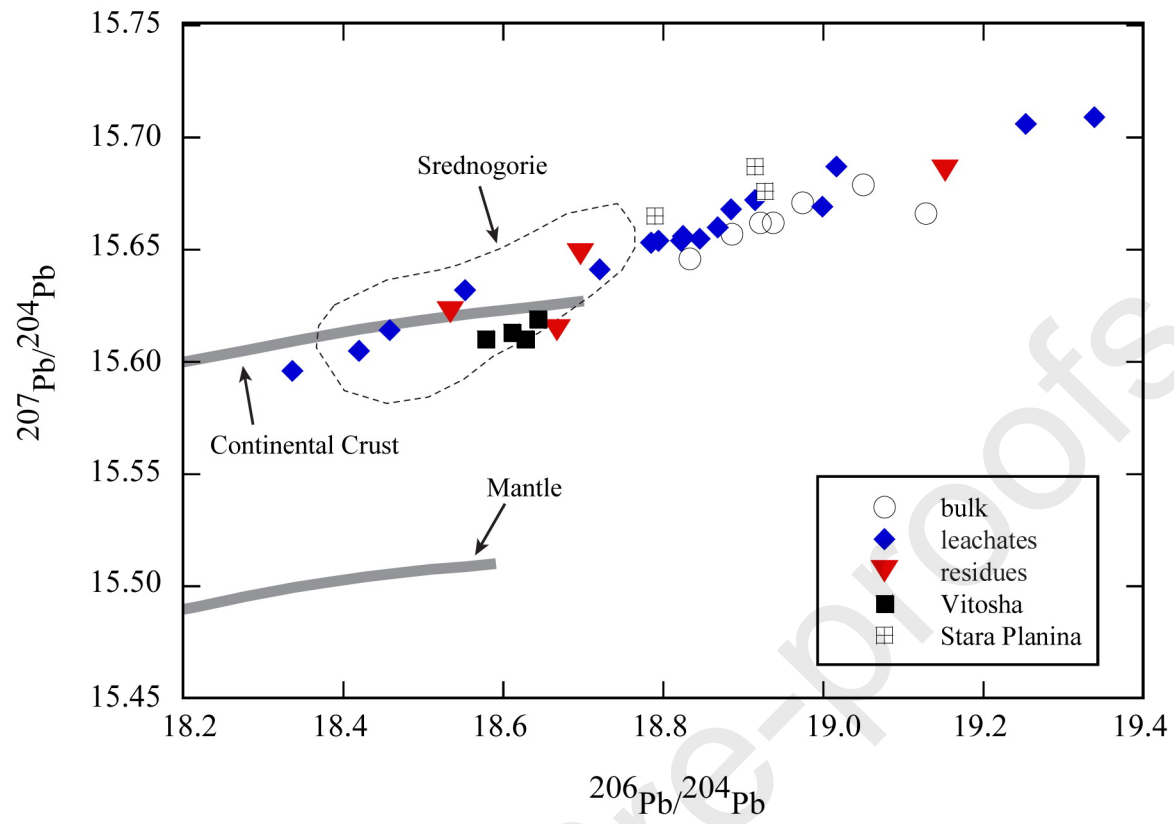
1572



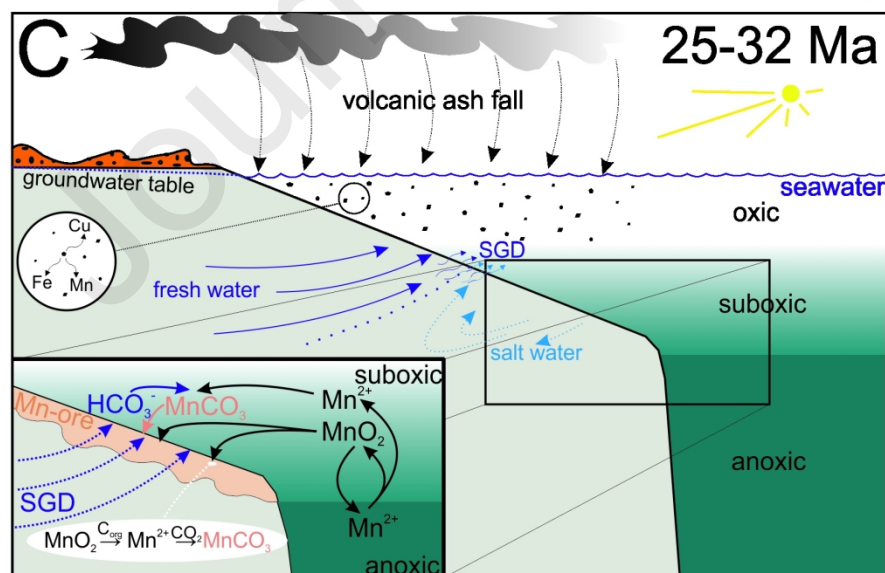
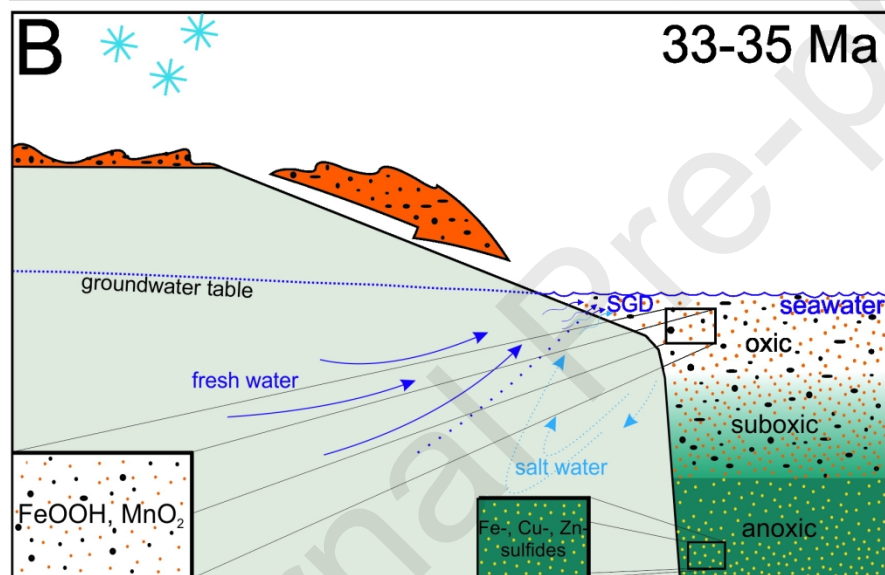
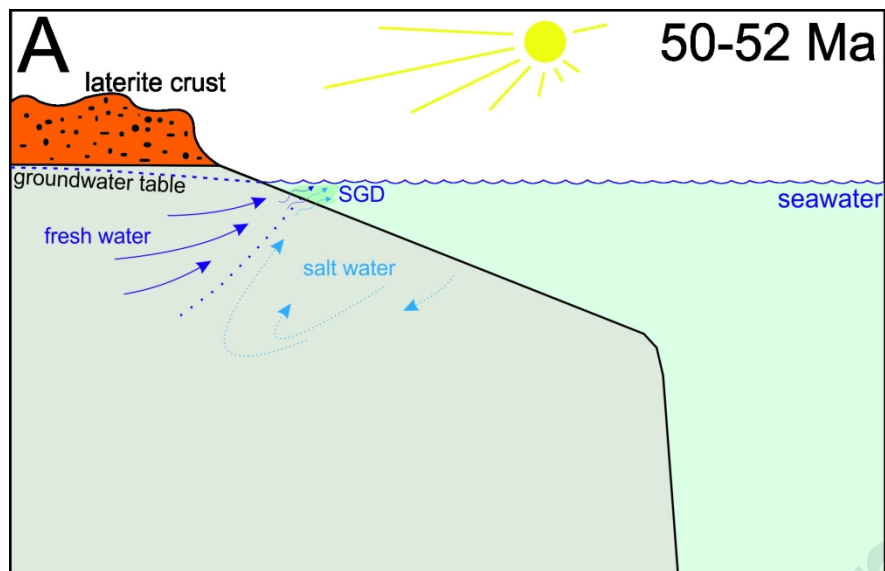
1573

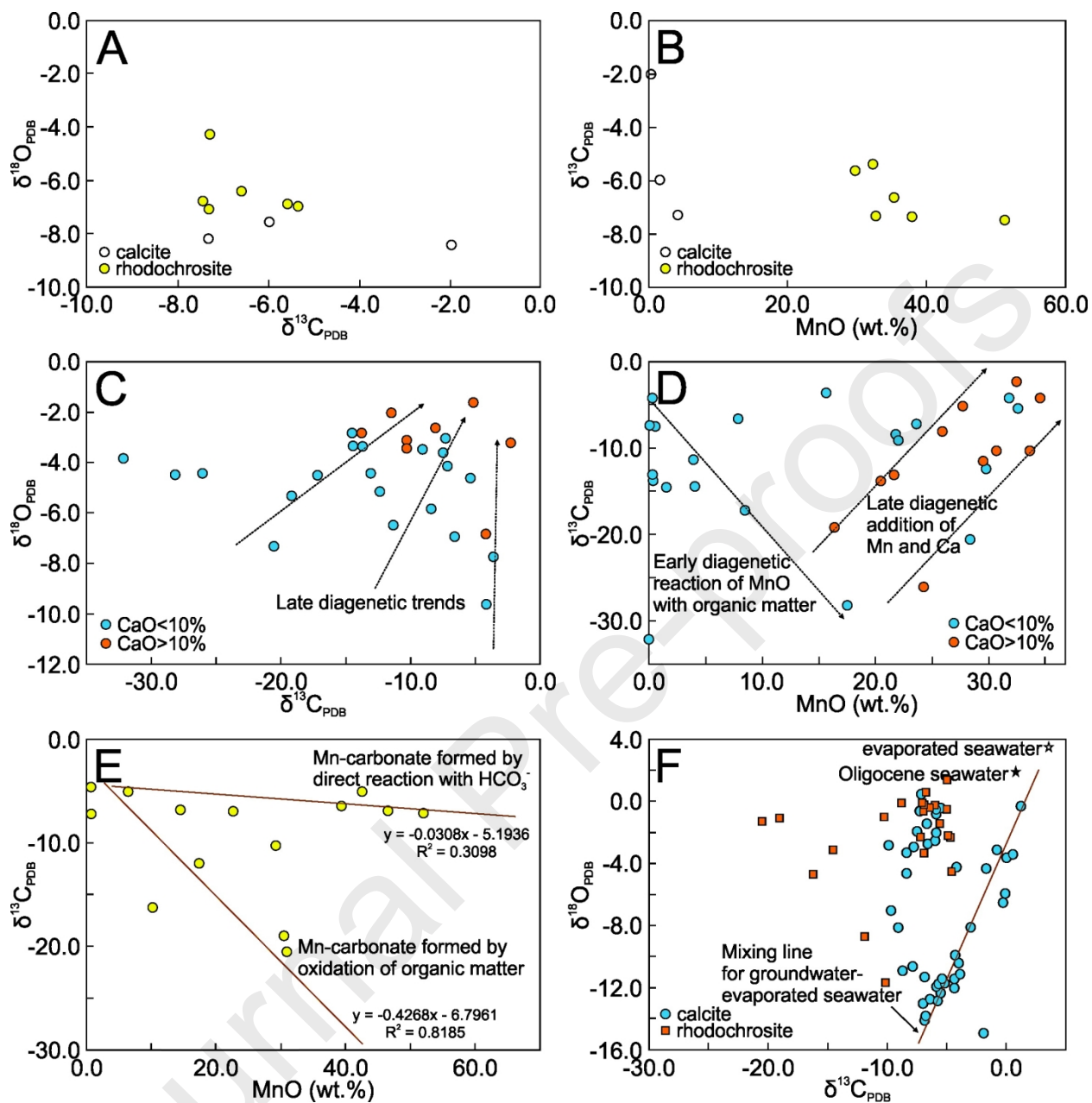


1574



1575





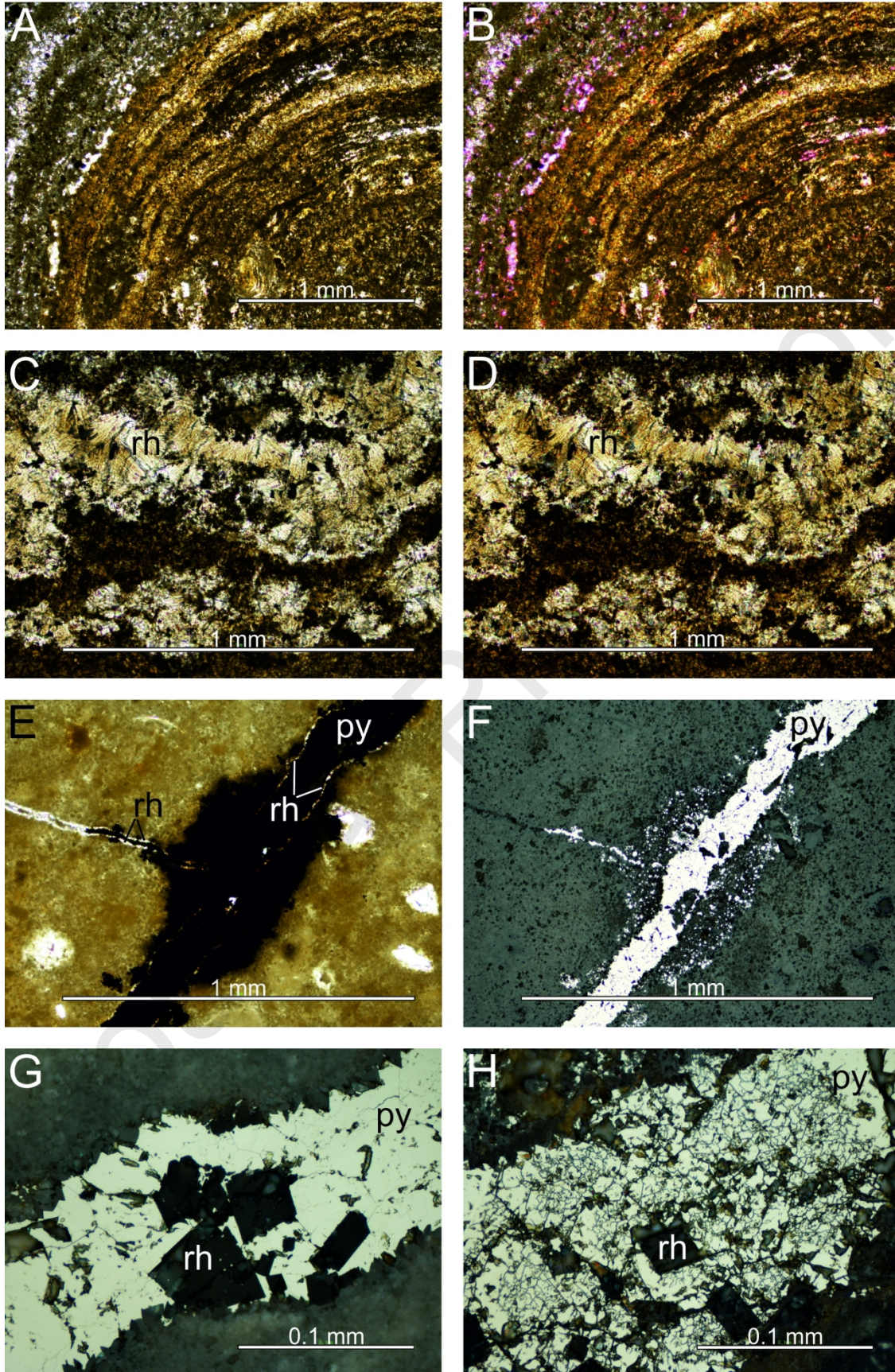
1577

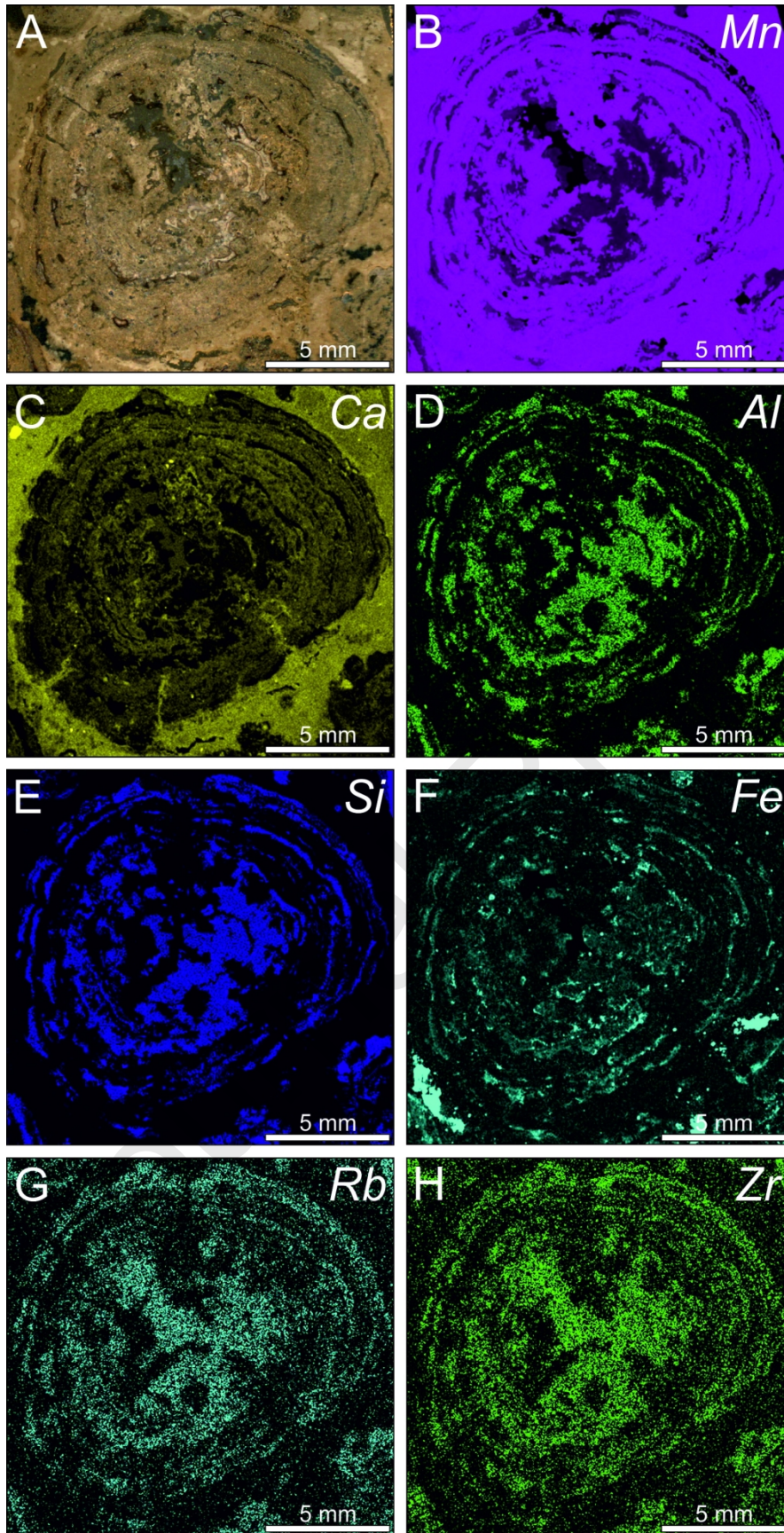


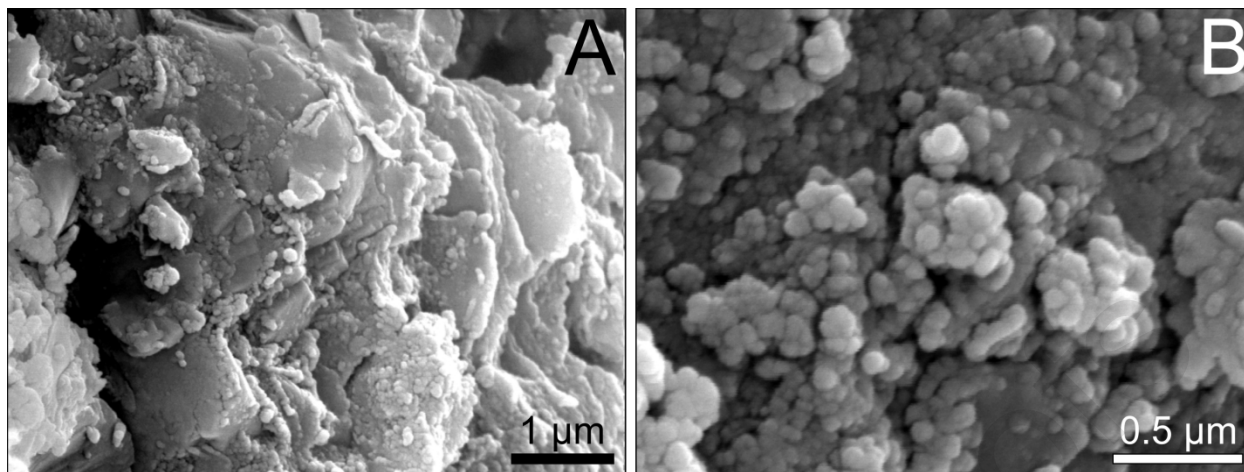
1 cm

1578

Journal Pre-proofs

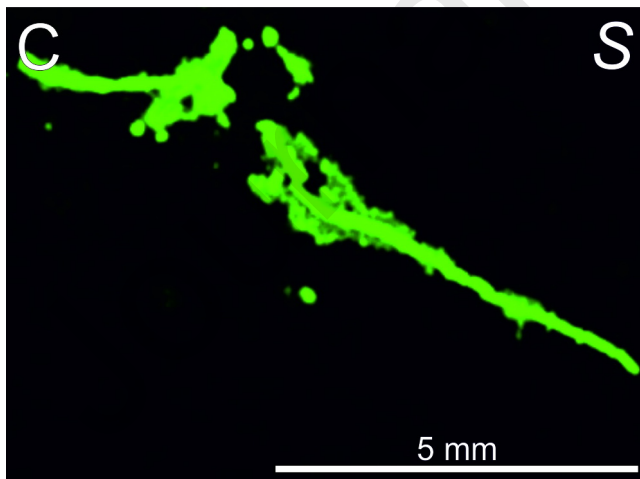
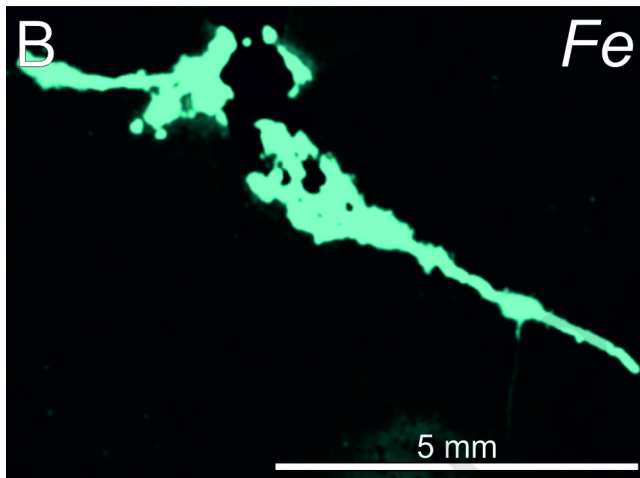
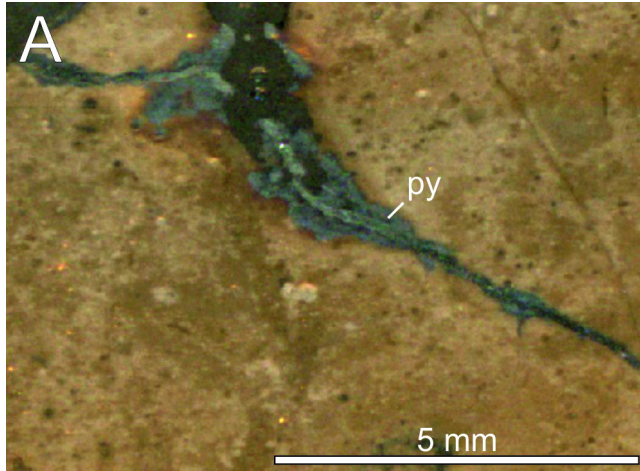




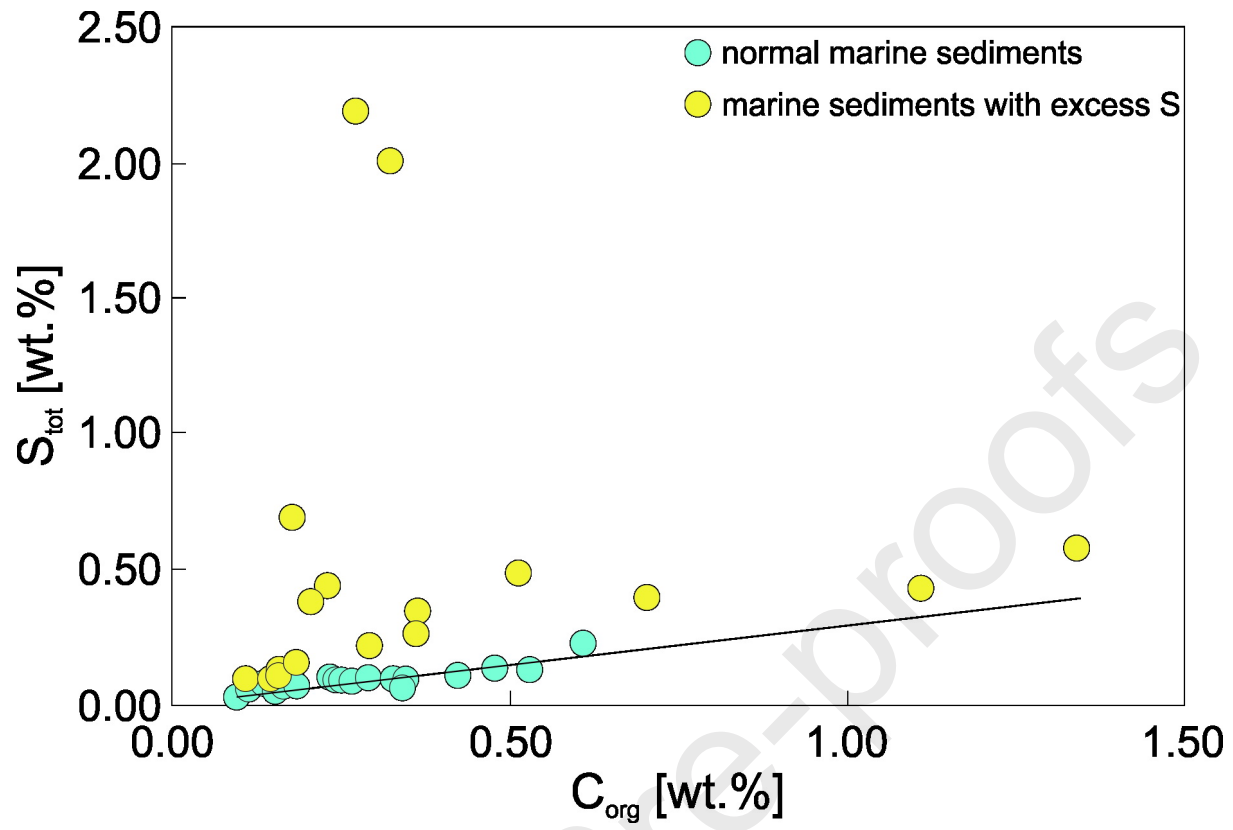


1581

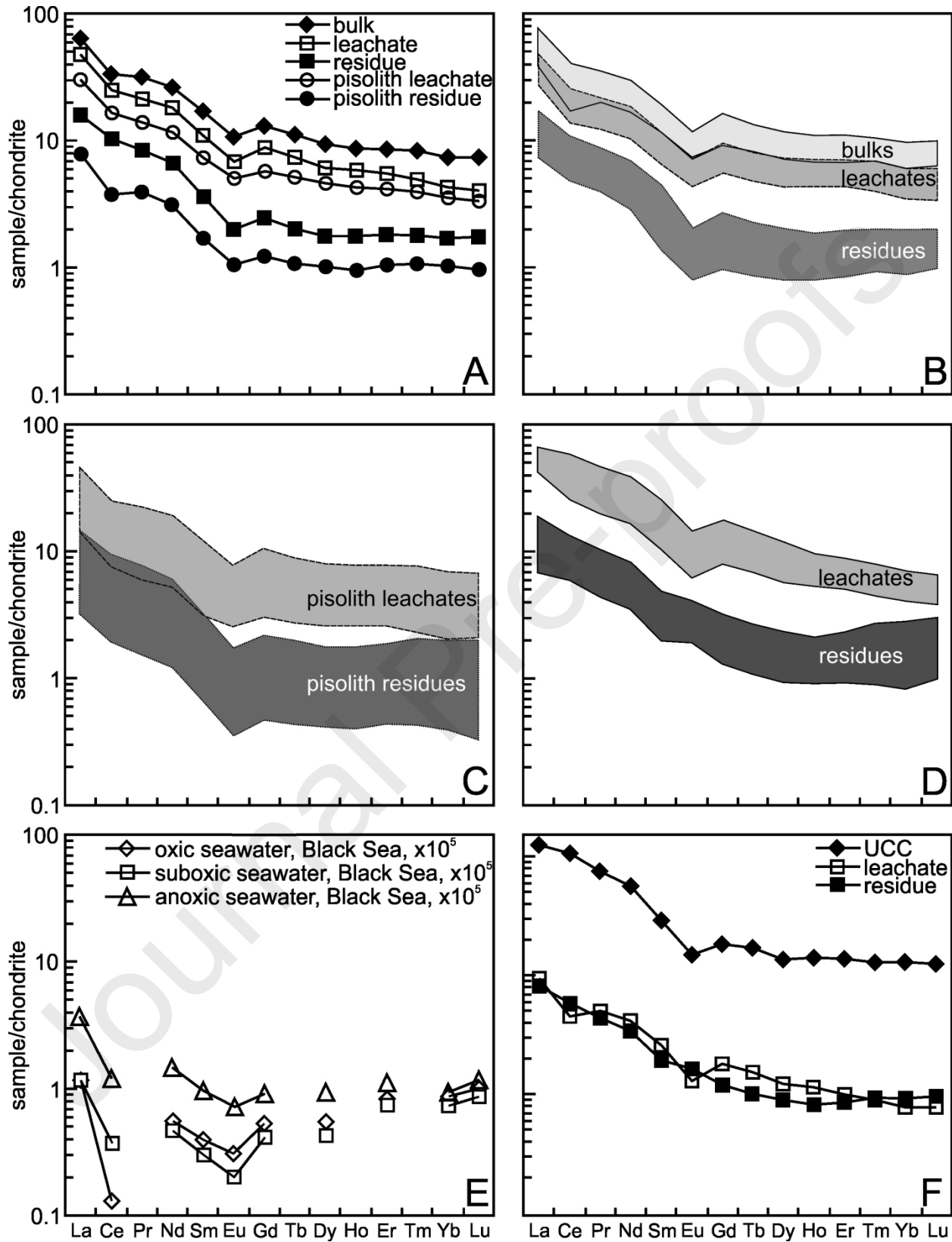
Journal Pre-proof



1582



1583



1584

